GEOSTATISTICAL INTEGRATION OF CORE AND WELL LOG DATA FOR HIGH-RESOLUTION RESERVOIR MODELING

A THESIS IN

Environmental and Urban Geosciences

Presented to the Faculty of the University
of Missouri-Kansas City in partial fulfillment of
the requirements for the degree

MASTER OF SCIENCE

By

KATRINA M BURCH

B.S., University of Missouri - Kansas City, 2009

Kansas City, Missouri

2012

GEOSTATISTICAL INTEGRATION OF CORE AND WELL LOG DATA

FOR HIGH-RESOLUTION RESERVOIR MODELING

Katrina M Burch, Candidate for the Master of Science Degree

University of Missouri – Kansas City, 2012

ABSTRACT

Analyzing data derived from well logging and core plugs to understand the heterogeneity of porosity in geologic formations is paramount in petrological studies. The well-log data and core-plug data are integrated in order to generate an accurate model describing the porosity distribution; however these data exist at different scales and resolution. This difference necessitates scaling of one or both sets of the data to aid in integration.

The present study established a geostatistical scaling (GS) model combining mean, variance, skewness, kurtosis and standard deviation with a misfit algorithm and sequential Gaussian simulation to integrate porosity data in conjunction with correlating the depth of core-plug data within the well-log data through a scaling process. The GS model examined well-log porosity data from a Permian-age formation in the Hugoton Embayment in Kansas

and well log data from a Cretaceous-age formation in the GyeongSang Basin in The Republic of Korea. Synthetic core-plug porosity data was generated from well-log data with random number generation.

The GS model requires basic histograms and variogram models for scaling the computerized tomography (CT) plug data to well log scale as well as integrating the data in a sequential Gaussian simulation. Variance-based statistics were calculated within specific intervals, based on the CT plug size, then a best fit for depth correlation determined. A new correlation algorithm, named the multiplicative inverse misfit correlation method (MIMC), was formulated for accurate depth correlation. This associated depth then constrained the well log porosity data at reservoir- or field-scale to interpolate higher-resolution porosity distributions.

Results for all the wells showed the MIMC method accurately identified the depth from which the CT plug data originated. The porosity from the CT plug data was applied in a sequential Gaussian co-simulation, after kriging the well log data. This culminated in a greater refinement in determining the higher porosities distributions than the interpolation of solely the well log data. These results validate the proposed high-resolution model for integrating data and correlating depths in reservoir characterization.

Approval Page

The faculty listed below, appointed by the Dean of the College of Arts and Sciences have examined a thesis titled "Geostatistical Integration of Core and Well Log Data for High-Resolution Reservoir Modeling," presented by Katrina M Burch, candidate for the Master of Science degree, and certify that in their opinion it is worthy of acceptance.

Supervisory Committee

Jejung Lee, Ph.D. Committee Chair
Department of Geosciences

Tina Niemi, Ph. D.
Department of Geosciences

K. Dave Newell, Ph. D.
Department of Geosciences

CONTENTS

ABSTRACT iii

LIST OF ILLUSTRATIONS viii

LIST OF TABLES x

LIST OF EQUATIONS xi

LIST OF SYMBOLS xiii

ACKNOWLEDGEMENTS xv

Chapter

1. INTRODUCTION 1

    1.1 Background 1

    1.2 Objectives 3

2. GEOSTATISTICAL FRAMEWORK 6

    2.1 Well-Log Data 6

    2.2 CT and Core-Plug Data 8

    2.3 Porosity 9

    2.4 Geostatistical Characterization of a Reservoir 11

    2.5 Porosity Modeling 12

3. FORMULATION OF THE GEOSTATISTICAL SCALING MODEL 16

    3.1 Defining the Histogram and Semi-Variogram 17

    3.2 Generating Basic Statistics 17

    3.3 Scaling Process 22

    3.4 Scaling with Sequential Gaussian Simulation 23

4. APPLICATIONS OF THE MODEL: CASE STUDIES 24

    4.1 Case Study Overview 24

4.2 Case Study: Jinju Sub-basin, Republic of Korea 24
4.3 Results for Jinju Sub-basin, Republic of Korea 28
4.4 Case Study: Panoma Gas Field, Kansas 35
4.5 Results for Panoma Gas Field, Kansas 43
4.6 SGS Results for Panoma Gas Field, Kansas 48
5. DISCUSSION OF RESULTS 54
5.1 Misfit and Likelihood 54
5.2 MIMC Discussion 55
5.3 SGS Scaling Discussion 65
5.4 Further Work 69
6. CONCLUSION 71
APPENDIX 74
REFERENCES 106
VITA 111

ILLUSTRATIONS

Figure		Page
1.1	Geostatistical modeling flow	4
2.1	The relationship between the well core and plugs	8
3.1	Flowchart for the geostatistical scaling model	16
4.1	Jinju Formation in outcrop at Bitori-do Island, Korea	26
4.2	Photo of core showing the darker-grey mudstone and lighter-grey sandstone	27
4.3	Histogram showing distribution of Jinju well-log data	29
4.4	Histogram showing distribution of Jinju CT data	29
4.5	Variogram at 1 meter well-log scale of Jinju well	30
4.6	Variogram at 0.01 meter CT scale of Jinju well	30
4.7	Graph showing non-scaled likelihood results, Jinju well	32
4.8	Upscaled results showing likelihood to depth, Jinju well	32
4.9	Entropy for Jinju for each likelihood function per data window	33
4.10	Jinju data showing correct correlation depth after using MIMC	34
4.11	Site map of wells in the Panoma Gas Field, Grant County, Kansas	36
4.12	Cross section of Hugoton and Panoma Field	37
4.13	Distribution of the Panoma Field well-log data	40
4.14	Distribution of the Panoma Field CT data	40
4.15	Variogram for the Panoma Field well-log data	41
4.16	Variogram for the Panoma Field CT data	41
4.17	3D point dataset of well-log porosity from Panoma Gas Field	42
4.18	Variogram for well-log scale of Well 20369	44
4.19	Variogram for CT scale of Well 20369	44

4.20 Likelihood for Well 20363 46
4.21 MIMC for Well 20363 46
4.22 Likelihood for Well 20370 47
4.23 MIMC for Well 20370 47
4.24 Interpolation of Panoma Gas Field to 1x1 cell size using SK 48
4.25 Interpolation of Panoma Gas Field to 1x1x1 size using SGS 49
4.26 Upscaled Panoma Gas Field to 5x5x5 cell size from SGS 50
4.27 Upscaling of SK Panoma Gas Field to 5x5x5 cell size 51
4.28 Downscaling of SGS Panoma Gas Field to 1x1x1 cell size after SGcS 52
4.29 Downscaling of SK Panoma Gas Field to 1x1x1 cell size after SGcS 53
4.30 SGS results for Panoma Gas Field to 1x1x1 cell size with no co-simulation 53
5.1 Cross plot showing correlation of porosity values 60
5.2 Cross plot showing correlation of skewness values 61
5.3 The greatest values within the uncertainty range can be seen with the graph 64
5.4 SGS simulation on log porosity values to 1x1x1 67
5.5 After SGcS and downscaled back to 1x1x1 size 68

TABLES

Tables Page

5.1 Showing how the mean skews the final results 57

5.2 Correlation coefficients for the statistical parameters 58

5.3 Comparing statistical parameters for well-log and CT for each well 59

5.4 Error variances for each well at the correlated depth 59

5.5 The progression from primary statistics to Misfit results
with unknown correlation depth 62

5.6 Continuing the progression from Misfit to best-fit with unknown CT depth 63

5.7 Setting the variance to the selected depths5
when the best-fit depth is unknown 64

5.8 MIMC results of selected depths to determine
the best-fit depth when it is unknown 65

EQUATIONS

1	Porosity	$\Phi = \frac{Pore\ Volume}{Bulk\ Volume} = \frac{\rho_{ma} - \rho_b}{\rho_{ma} - \rho_f}$	9
2	Simple kriging	$Z_{SK}(u) = m + \sum_{\alpha=1}^{n(u)} \lambda_\alpha^{SK}(u)[Z(u_\alpha) - m]$	13
3	Omni-directional Variogram	$\gamma(h) = \frac{1}{2N(h)} \sum_{\alpha=1}^{N(h)} [z(u_\alpha) - z(u_\alpha + h)]^2$	17
4	Mean	$\bar{x} = \frac{1}{N}\sum_{i=1}^{N} x_i$	18
5	Variance	$\sigma^2 = \frac{1}{N-1}\sum_{i=1}^{N}(x_i - \bar{x})^2$	18
6	Skewness	$Skew = \frac{1}{N}\sum_{i=1}^{N}\left[\frac{x_i - \bar{x}}{\sigma}\right]^3$	18
7	Kurtosis	$Kurt = \left[\frac{1}{N}\sum_{i=1}^{N}\left[\frac{x_i - \bar{x}}{\sigma}\right]^4\right] - 3$	18
8	Standard deviation	$\sigma = \frac{1}{N-1}\sum_{i=1}^{N}(x_i - \bar{x})$	18
9	Parameter upscaling	$P_V = P_v \cdot \frac{1 - \bar{\Gamma_v}}{1 - \bar{\Gamma_V}}$	19
10	Misfit function	$M(x) = \sqrt{\frac{(T(x) - T)^2}{\sigma^2}}$	19
11	Group average deviation, misfit	$\bar{\Delta}(x) = \frac{1}{N}\sum_{i=1}^{N}(Mx_i - \bar{M}x)$	20

12	Misfit correlation constant	$C_m\,(x) = \frac{1}{\bar{\Delta}\ (\mathrm{x})}$	20
13	Multiplicative inverse misfit correlation method, MIMC	$C_m\,(x) = \frac{N}{\sum_{i=1}^{N}(Mx_i - \bar{M}x)}$	20
14	Likelihood function	$L_i(x) = e^{-M(x)^2}$	20
15	Group average deviation, likelihood	$\overline{\Delta(x)} = \frac{1}{4}\sum_{i=1}^{4}(L_i(x) - \bar{L}(x))$	21
16	Likelihood correlation constant	$C_l\,(x) = -\ ln\ (\bar{\Delta}(x))$	21
17	Entropy function	$H = -K\sum_{i}^{I} p_i\ \ln p_{i\,,}$	22
18	Averaging of data, upscaling	$\bar{A} = \frac{1}{4}\{X_m(i,j) + X_m(i,j+1) + X_m(i+1,j) + X_m(i+1,j+1)\}$	22
19	Random number function	= RAND ( ) * (X_2 - X_1) + X_1	27
20	Electron density	$\rho_b\ = \frac{\rho_e}{A/_{2Z}}$	38
21	Observed gamma ray	$\gamma_{obs}\ = \frac{k}{\rho_e}$	38
22	Bulk density to observed gamma ray	$\rho_b\ = \frac{k}{\gamma_{obs}}$	38

LIST OF SYMBOLS

Φ	Porosity
ρ_{ma}	Grain density of the matrix
ρ_b	Bulk density of the formation
ρ_f	Fluid density
z(u)	Random variable, such as porosity
N(h)	Number of pairs of data separated by h
h	The lag distance
x	Value under investigation
N	Number of values under investigation
x	Mean or average for that set of values
σ^2	Variance
σ	Standard deviation
P_V	Statistical parameter of the larger volume measurement
P_v	Statistical parameter of the smaller volume measurement
Γ_V	Normalized point scale sill of larger volume of investigation
Γ_v	Normalized point scale sill of smaller volume of investigation
T(x)	Observed well log statistic at depth x
T	Reference plug statistic
M(x)	Misfit at depth x
$\overline{\Delta}$	Group average deviation
C_m (x)	Correlation constant at depth x from misfit parameters
$L_i(x)$	Likelihood at depth x
C_l (x)	Correlation constant at depth x from likelihood parameters
p_i	Normalized parameter at depth i
K	Entropy constant
H_i	Entropy at depth i
X_m	The data value at m-th cell
i	The x coordinate of m-th cell
j	The y coordinate of m-th cell
A	The mean value of four X_m
u, u_α	Location vectors for estimation point
α	Index for neighboring data points
$Z(u_\alpha), Z_{sk}(u)$	Datum point
$n(u)$	Number of conditioning data points
$\lambda_\alpha^{SK}(u)$	Kriging weight

ρ_e	Electron density
A	Molecular weight
Z	Number of electrons per molecule
γ_{obs}	Observed gamma ray measurement
k	Density constant relating gamma ray to bulk density

ACKNOWLEDGEMENTS

I would like to recognize the people who helped make this thesis a reality.

I am grateful to my son, Spencer, for his patience with mommy when she had to work and could not play. You are my guiding force behind this. I am appreciative and beholden to my mother, Janice, who stepped in with Spencer or gave me the daily support I needed. You are the paragon of what a mother should be. My brother, Eric, my sister, Candace, and my dad, Vince, have given me their unequivocal support throughout, for which my expression of thanks probably does not suffice. Each and all of you have been supportive of me, even when this project took me away from home for long periods.

This thesis would not have been possible without Dr. Jejung Lee, without whom I would not have worked on this project and been able to accomplish so much in the two short years we've been working on this. You have been there to guide me and push when needed and I sincerely thank you. I hope I have not been too much trouble. I am thankful to Dr. Jhin at KIGAM for sponsoring this project, providing the Korean data and giving me a place to study for two months. I also am grateful and recognize the staff and students at KIGAM who helped make my stay there better, you know who you are. ☺

For the good advice, support, and friendship from Dr. Tina Niemi, who also had the confidence in me to complete this project, I am extremely appreciative. I would like to acknowledge and express gratitude to Dr. Dave Newell for answering my questions at the beginning, his wonderful comments, and for being on my committee. I would also like to send a BIG thank you to the following staff at KGS who tolerated my endless questions, Dr. Doveton and Martin Dubois. I realize my questions about the data seemed never-ending and your assistance was never forgotten.

Last but certainly not least, I would like to send a thank you to all the friends I have made along the way, at UMKC, and to my fellow EAPSI peeps. If not for you, I would have been all work and no play.

CHAPTER 1

INTRODUCTION

Geologic reservoirs serve as fundamental archetypes for gas and oil exploration, methane extraction and carbon sequestration. Among many physical parameters, porosity and permeability are the major factors determining the capacity of gas/oil production and carbon storage. Well logging and core experiments are the methods for examining lithology and rock characteristics in order to analyze the porosity and permeability relations in carbonate reservoir formations. The data resolution and spatial coverage combined with the quantity of measured parameters occur at separate scales to impart subsurface lithology and structural information.

1.1 Background

Evaluating geologic reservoirs requires continual effort due to the heterogeneity of the rock and the lack of modern day proxies for carbonate formation (Lucia, 1999). Heterogeneity creates challenges modeling and predicting flow, therefore knowledge about heterogeneity is essential for evaluating fluid flow behavior. The geophysical measurements exploring the characteristics of a petroleum reservoir include well-log data at the medium-scale and small-scale computerized tomography (CT) scans or core-plug data. The measurements taken directly from well logs and CT scans are used as proxies for determining the porosity at that location (Rider, 1986). Investigating and determining the capabilities of

carbonates and sandstone as reservoirs and the amount of petroleum contained in them can be accomplished by using geophysical techniques and geostatistics.

Porosity heterogeneity within the reservoir occurs at various scales from large vugs to interparticle, making multi-scale geological-heterogeneity integration complex. Intricate porosity distributions dominate in carbonate formations due to dissolution and diagenesis creating secondary porosity (Choquette & Pray, 1970). The high porosity in carbonates allows for reservoir capabilities, resulting in carbonates producing nearly half of the world's petroleum (Prothero & Schwab, 2004).

During the coring process, sections of the core may not be fully recovered, so the exact depths of any scans or plugs taken from the core are difficult to establish. The accuracy of the depth correlations depends on the skills of the logging geologist and the amount of useable retrieved core, and even then there may be more than a 2-foot (0.61 meters) correlation-match uncertainty. The typical method for correlating strata at different depths involves matching the lithology from the extracted core to the well-log data.

Well-log data and core-plug measurements exemplify types of hard data, as they derive from accurate measurements generated by tools directly on the geologic formation (Hirsche, Boerner, Kalkomey, & Gastaldi, 1998). Yet core measurements and well logs evaluate at different scales that the researcher must explicate in reservoir modeling. These measured data evince different volume scales that necessitate deliberation before beginning modeling.

Well logging evaluates at a medium resolution or scale (several centimeters) with medium coverage (several meters). Meanwhile, laboratory measurements on the core investigate at a maximum resolution (micrometer to millimeter) but with minimum coverage

(centimeters). This variance in scale leads to concerns during the depth correlation when determining how to relate the higher resolution measurements of the computerized tomographic (CT) scan or core-plug data to the lower resolution well-log measurements. These differences in the volume resolution of measurements generate the necessity of scaling the data.

The resolution of well-log measurements determines the spatial accuracy of the data at that scale and the uncertainty in correlations. Additionally, core-plug data exhibits greater variations in measurements than well-log due to an increase in the resolution of the data (Oz, Deutsch, & Frykman, 2002; Tilke, Allen, & Gyllensten, 2006). Data integration then becomes incompatible across the available data-resolution range.

Various geostatistical methods combine and correlate data to facilitate the generation of reservoir models which detail the reservoir's characteristics and make production estimates for the reservoir. Variograms and kriging represent the most common geostatistical methods for integrating spatially varying parameters. However, variograms cannot discern natural variations in the reservoirs due to the limitations of interpolation smoothing and an increase in uncertainty owing to inadequate data distributions (Leary & Al-Kindy, 2002; Liu, Harding, Abriel, & Strebelle, 2004).

1.2 Objectives

The present study seeks to illustrate the capability of geostatistics in examining several parameters in porosity data, correlating the maximum -resolution data to the medium-resolution data, and then constraining the data to construct a high-resolution geostatistical model. This study also investigates the efficacy of a geostatistical modeling approach to the

integration of geophysical data from well-logs and core experiments under different geologic settings of reservoir.

The objective is the development of a multi-dimensional high-resolution modeling framework for the reconstruction of stratigraphically-ordered rock formation in reservoirs using geostatistical techniques involving a misfit/likelihood method and sequential Gaussian simulation (SGS). The model actuates with basic statistics arising from well-log and CT plug porosity data and then implements a scaling process to compare and identify the best depth correlation. Figure 1.1 illustrates the proposed modeling flow of a geostatistical framework to integrate core and well-log data from a reservoir beginning with the multiplicative inverse misfit correlation method after scaling the core data.

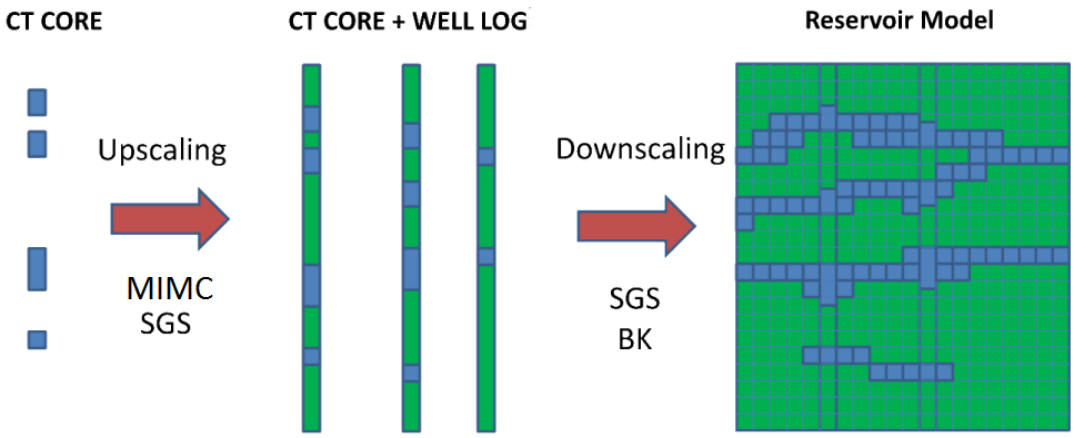

Figure 1.1, Geostatistical modeling flow

Step-1. Porosity/permeability measurements from computerized tomographic (CT) images of cores from a single bore hole will update well-log data using the MIMC method.

Step-2. The updated well-log data and the CT core data are upscaled to a one-dimensional cell structure using arithmetic upscaling formulation.

Step-3. The CT core data are used in a sequential Gaussian co-simulation to integrate the data and upscaled to a coarser, multidimensional-scale resolution.

Step-4. Multiple lines of a one-dimensional porosity/permeability model are interpolated/extrapolated using simple kriging and SGS.

Step-5 (optional, if have seismic data). When a two-dimensional inversed model of porosity or permeability from seismic survey is available, depending on the resolution of seismic model, the model from Step 3 will be either upscaled or downscaled by using SGS or block kriging.

CHAPTER 2

GEOSTATISTICAL FRAMEWORK

2.1 Well-Log Data

Well-log data originate from a constant recording obtained in a borehole and documents diverse geological parameters (Rider, 1986). The measurements derive from three techniques: mechanical, spontaneous or natural, and induced. The well-log tests quantify the properties of rock matrix and the fluids or gases in the pores surrounding the well in an attempt to locate formations containing hydrocarbons (Bigelow, 1992; Luthi, 2001). Porosity, texture, internal structure, and permeability are rock characteristics defined by the well-log tests.

On a larger scale, lithology, bed thickness, compaction, and reserve estimates may also be ascertained through well-log tests (Bigelow, 1992). A collection of well-log data encompassing a geographical area provides material to define reservoir geometry, correlate beds, and map structures (Asquith & Gibson, 1982). Reservoir properties then can be described through combining well-log and core-plug data.

There are two methods for well-log testing, open hole or logging-while-drilling (LWD) (Luthi, 2001). Open-hole logs take place once drilling is complete and in the uncased portion of the well (Asquith & Gibson, 1982; Luthi, 2001). The instruments, attached to a cable or wire-line, are subsequently lowered into the depths of the well to acquire the data (Serra, 1984). The down-hole logger records the data as the wire-line is pulled back up from

the bottom while transmitting the information to the surface (Rider, 1986). LWD logs are performed during the drilling of the well, to lessen fluid invasion and borehole damage effects, with the instruments placed in the bottom-hole assembly of the drill (Luthi, 2001). This allows for real-time data acquisition. A specific curve, collection of curves, a logging tool or the logging process can all be expressed as a "log" (Asquith & Gibson, 1982).

The logging tools obtain the measurements while moving and the sensors have dimension, which while factored into the design means the measurements are not perfect (Rider, 1986). Rock characteristics such as permeability, porosity, water saturation, and resistivity will also affect the measurements (Asquith & Gibson, 1982). The fluid and mud administered during drilling generally enters the bedrock surrounding the borehole and consequently influence the log measurements.

Natural phenomena simply need an appropriate sensor to obtain the measurements; called mechanical and spontaneous measurements (Rider, 1986; Serra, 1984). Natural or spontaneous measurements involve self or spontaneous potential (SP) and gamma-ray, while mechanical measurements include temperature and borehole diameter (Rider, 1986). Calipers measure the well diameter; thermometers record the formation temperatures at different depths, which is required when defining porosity and permeability in the formation. Spontaneous potential reads the spontaneous electrical currents and gamma-ray calculates the natural radioactivity in the formation.

Induced measurements need an emitter or transmitter, which creates a specific reaction in the formation, plus a detector (Serra, 1984). Induced measurements include resistivity, neutron porosity logs, and sonic or acoustic measurements. Resistivity measures how well electricity flows through the formation since locations containing hydrocarbons act

as resistors. Sonic measurements test the travel velocity of sound waves through the rock; neutron ray and density tests measure the gamma-ray or neutron density that through processing determines the amount of pore space or porosity.

2.2 CT and Core-Plug Data

Core plugs consist of small corings or plugs removed from the larger core procured during the well drilling, illustrated in Figure 2.1. Microscopic methods and rock physics examine these plugs to gain insight into porosity and the matrix framework. Without these analyses which evaluate beyond the surface of the core, the formation's porosity would lack a detailed rendering and lead to inaccuracies when characterizing the reservoir.

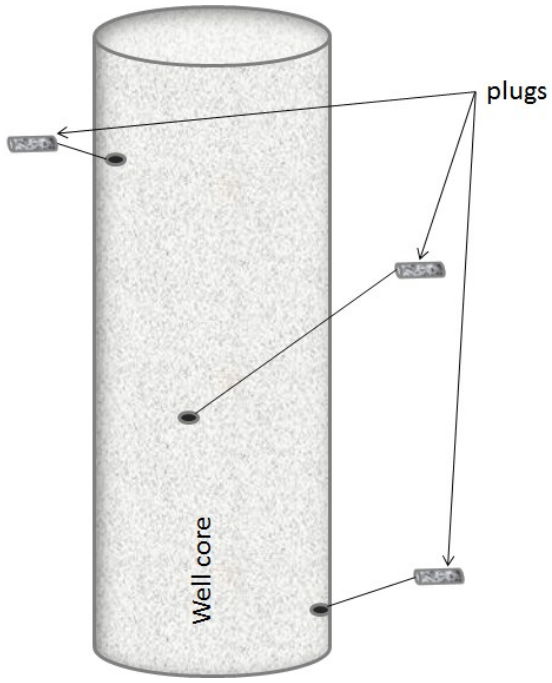

Figure 2.1, The relationship between the well core and plugs

Scanning electron microscopy (SEM) and x-ray computerized tomography (CT) directly render porosity from an extracted core and allow for whole core inspection at the macroscale. The CT scanners measure the average attenuation of an X-ray beam as it passes through a sample. The resolution of the tomography is 0.165 milimeters, which is the size of the voxel, the three-dimensional volume cubes that represent the average attenuation of material within the voxel (Price, Curtis, & Wood, 2008). This higher detailed analysis, capable from the CT images, reveals the pore sizes and shapes while also allowing for investigating fractures without causing damage to the core.

Additionally, the identification of pore fluids and pore connectivity becomes perceptible under the comprehensive exploration available from a CT investigation. The porosities resulting from CT images or core plugs present higher variability than porosity derived from well logs. However, since these measurements are highly precise due to the type of investigation, these porosities reveal an accurate view of the porosity at that location or depth.

2.3 Porosity

Porosity of a formation is important in order to evaluate fluid content, potentiality of fluids to flow and probable recovery rates within a reservoir (Prasad, 2003). Porosity is the ratio of pore volume to bulk volume thus determining the volumetric concentration of pore space using the equation

$$\Phi = \frac{Pore\ Volume}{Bulk\ Volume} = \frac{\rho_{ma} - \rho_b}{\rho_{ma} - \rho_f} \quad (1)$$

where Φ is the porosity, ρ_{ma} is the density of the grain matrix, ρ_f is the density of the fluid and ρ_b is the bulk density of the formation (Serra, 1984).

There are two different definitions of porosity: effective porosity and total porosity. Total porosity involves porosity that can never be accessed as a result of the pores not being connected. Effective porosity means the pores are connected with flow channels and thus fluids can be attained. The pores produced during the original sedimentation and lithification of the reservoir are called primary porosity. The pores generated later during multifarious geologic process following deposition, such as fracture or dissolution, are accordingly called secondary porosity.

Well logs can help compute porosity using either the gamma-ray log or by the preferred method with the neutron density logs. The gamma-ray logs use an algorithm to formulate the bulk density of the formation. Once the matrix density and fluid density is known, the porosity can be calculated using Equation (1). When using the neutron density logs, the neutron porosity (NDPI) and density porosity (DPHI) logs are averaged to directly estimate the porosity.

Akin, Ross & Kovscek (2008) suggest that porosity distribution is neither random nor homogeneous thus consequently its structure impacts the petrophysical character of rock. Porosity heterogeneity in a reservoir is complex with pore throat scales stretching over orders of magnitude (Choquette & Pray, 1970; Price et al., 2008). Exploration of the porosity distribution varies depending on the ultimate objective of the reservoir characterization and the relationships of the tested parameters. Porosity distribution statistics develop from statistical scaling relationships between high-resolution data and low-resolution data, which then improves the porosity heterogeneity understanding for modeling reservoirs (Price et al., 2008; Tilke et al., 2006). The major problem when developing these relationships consists of

correlating the high-resolution sections, CT data, to the low-resolution information, well log data (Price et al., 2008).

2.4 Geostatistical Characterization of a Reservoir

Various geostatistical techniques are developed to combine and correlate data, and to facilitate the generation of numerical models that detail the reservoir's characteristics. Identifying statistical relationships between measurements helps predict the porosity distribution (Price et al., 2008). Geostatistical analysis examines the spatial relationships between measured properties of rocks which is a useful precursor to reservoir modeling.

One or more variables distributed through space and having multiple values is a feature of natural phenomena and obliges geostatistics to describe these variables as regionalized. In geology, nearly all the variables can be considered as regionalized and thus analyzed to a greater degree using geostatistics. Matheron (1970) indicated that the application of random functions to the observations and estimations of natural phenomena defines geostatistics.

According to Journel & Huijbregts (1978) "geostatistical theory is based on the observation that the variabilities of all regionalized random variables have a particular structure" (p. 10). Geostatistical estimation assumes that the variable z at location x is the value or function $z(x)$ and leads to representing the variability of the function where x varies (Journel & Huijbregts, 1978; Minasny, Vrugt, & McBratney, 2011). Geostatistical solution requires interpreting every value of $z(x)$ as a realization of a random variable $Z(x)$.

A random variable takes a series of values as possible outcomes, each according to a certain probability distribution with a particular frequency of occurrence (Journel & Huijbregts, 1978; Remy, Boucher, & Wu, 2009). The set of random variables realized at

every point *x* defines a random function. The random variable and function lie at the root of any conceptual models developed in geostatistics (Remy et al., 2009). The geostatistical model is designed to represent reality but in an uncomplicated process to facilitate describing or predicting a particular variable. The complexity of the model relates more to the number of parameters involved in the model instead of the amount of observations (Pawitan, 2001).

2.5 Porosity Modeling

Porosity is often modeled alongside permeability and acoustic impedance when characterizing a reservoir's properties, particularly when modeling fluid flow (Alfaaouri, Riahi, Alizadeh, & Resaei, 2009; Deutsch, 2002; Leary & Al-Kindy, 2002; Liu et al., 2004; Prasad, 2003). Often times, porosity is modeled first due to the large amounts of available data, and is then compared to permeability data (Deutsch, 2002). Seismic data also is frequently combined to provide the overall structure of a reservoir although the scale difference between seismic and well-log data impedes the integration when modeling porosity (Al-Khalifah & Makkawi, 2000). When seismic data and porosity are incorporated together, the resulting porosity model has been very successful in delineating the distribution within geologic structures (Al Qassab et al., 2000; Tran, Wen, & Behrens, 1999; Xu et al., 1992).

Porosity modeling can be more accurate and successful after combining core plugs, well logs and seismic data (Fournier, 1995; Yao et al., 1999). Price et al. (2008) proposed the use of statistical parameters derived from porosity imaging of high resolution data to constrain correlation with well log data, an important step before a realistic model can be developed. Stochastic or geostatistical approaches, kriging and SGS, are the most common

procedures for porosity modeling, although artificial neural network techniques are currently being explored (Akin et al., 2008; Deutsch, 2002; Journel & Deutsch, 1993).

Kriging has a long history with geostatistics and prevails as a key tool in data integration (Isaaks & Srivastava, 1989; Journel & Deutsch, 1993; Remy et al., 2009). Simple kriging (SK) assumes the known mean is constant and a constant trending variable, and is defined by:

$$Z_{SK}(u) = m + \sum_{\alpha=1}^{n(u)} \lambda_{\alpha}^{SK}(u)[Z(u_{\alpha}) - m], \quad (2)$$

where u and u_{α} are the location vectors for estimation point and one of the neighboring data points indexed by α, $\lambda_{\alpha}^{SK}(u)$ is the kriging weight assigned to datum $Z(u_{\alpha})$ for estimation at the location *u, m* is the expected mean of $Z_{sk}(u)$ and $Z(u_{\alpha})$, and $n(u)$ is the number of conditioning data points used for the estimation of $Z_{sk}(u)$ centered at *u* (Journel & Huijbregts, 1978). However, this estimate is changed based on the established conditions. As the simulation process moves forward, each previous node's value is used in the kriging of the current node. This process is repeated until all nodes are visited. Simple kriging is adapted to gain a baseline estimate (Remy et al., 2009).

Block kriging (BK) approximates the random variable over a local area rather than a point and the covariance estimations are point-to-block rather than point-to-point (Isaaks & Srivastava, 1989). An advantage to block kriging is it gives one kriging solution yet provides a block average estimation. Since BK provides this block averaging it has a higher computational demand which is slightly negated as multiple kriging estimates are not needed (Isaaks & Srivastava, 1989; Tran et al., 1999). The BK estimation discretizes the variables on

a regularly spaced grid that based on the amount of points in the grid governs the spatial accuracy.

Sequential Gaussian Simulation (SGS) is similar to kriging, differing due to the application of conditioning to the estimates based on global statistics (Asghari, Soltni, & Amnie, 2009; Webster & Oliver, 2007; Tran et al., 1999). However, when using the Gaussian simulation, it must be noted that the random function aggrandizes the covariance model's entropy (Journel & Deutsch, 1993; Remy et al., 2009). Once global statistics are obtained and normalized within a Gaussian space, the known data is used to model a variogram which is the basis for the simulation. After the variograms are set up, a grid is defined on which to simulate data in a method similar to block kriging (Asghari et al., 2009; Remy et al., 2009).

However, unlike kriging, which minimizes variance of the parameter estimation, the SGS method maximizes variance of the estimation. To maximize this variance, a random path must be defined to visit each node within the block of data (Asghari et al., 2009; Tran et al., 1999). As the SGS process continues, the value of the prior node is calculated in the estimation of the current node and this repeats until all nodes are evaluated. During the SGS process some nodes may be overestimated and a process of back-transformation is needed. This process adjusts the out-of-line estimations to fit more suitably with the distribution of the data. This process is repeated until the entire model fits the normalization (Asghari et al., 2009; Delbari, Afrasiab, & Loiskandl, 2009). Every iteration or realization in the simulation represents a different model that can be reviewed and tested. The point of normalization is the simulation that best represents the actual area of examination.

Sequential Gaussian co-simulation (SGcS) utilizes the cokriging process to incorporate information contained in neighborhood secondary data which relates to the

primary variable when simulating the Gaussian variable (Babak & Deutsch, 2009; Deutsch, 2002). The primary variable is conditioned to the secondary variable with full cokriging which models co-regionalization to reproduce the variables within a correlation structure (Deutsch, 2002; Remy et al., 2009). The Markov Model 1(MM1) works around needing the multiple variograms required in the linear model of co-regionalization by only requiring the correlation coefficient between the primary and secondary variables (Babak & Deutsch, 2009; Remy et al., 2009).

CHAPTER 3

FORMULATION OF THE GEOSTATISTICAL SCALING MODEL

The geostatistical scaling model (Figure 3.1) combines several geostatistical stages in order to achieve correlation depths and integrate the porosity data from well-log and CT data. Basic histograms and semi-variogram models are needed to both upscale the CT plug data to well-log scale, and integrate the data with SGS. Variance-based statistics are calculated within the specified interval based on the CT plug length, then a best fit-for-depth correlation determined with the multiplicative inverse misfit correlation (MIMC) method. This depth then constrains the well-log porosity data at the reservoir or field scale, and thus interpolate all depths to the higher-resolution porosity distributions.

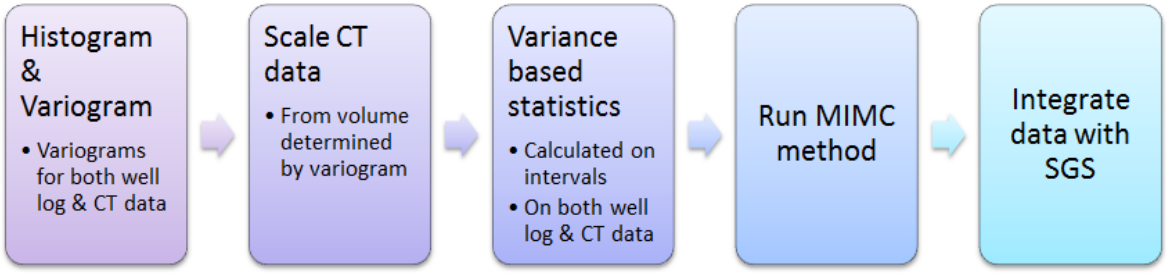

Figure 3.1, Flowchart for the geostatistical scaling model

3.1 Defining the Histogram and Semi-Variogram

Histograms are required for well-log porosity data and the CT plug data to obtain the set mean which SGS required for processing and estimation. A histogram graphically shows the distribution and frequency of the data and when combined with the percent frequency reveals how closely the data has a Gaussian distribution. The histograms are designed using twenty bins, which show the best representation of the distribution.

The algorithms used in scaling the CT data are based on the semi-variogram. An omni-directional semi-variogram, hereafter referred to simply as variogram, was calculated for the CT plug data as well as for the well-log data by:

$$\gamma(h) = \frac{1}{2N(h)} \sum_{\alpha=1}^{N(h)} [z(u_\alpha) - z(u_\alpha + h)]^2 , \qquad (3)$$

where z(u) is the porosity and N(h) is the number of pairs of data separated by h, the lag distance (Deutsch, 2002). The number of lags, for both the CT data and well-log data, are kept to a comparable value while the lag spacing and tolerance remained at lower numbers due to the close spatial proximity of the data.

3.2 Generating Basic Statistics

Statistics for mean, variance, skewness, kurtosis, and standard deviation are generated on porosity data for the entire CT core length, as well as on a moving window within the well-log data on intervals to correspond with the CT core length. The statistics were upscaled on the smaller measurement volume then algorithms compared the core data to well-log data using misfit, likelihood, and entropy.

Mean or the arithmetic average of the dataset defines the center of the distribution and responds easily to erratic values. Variance and standard deviation express the variability and spread of the data values; both conveying moments (shape) of the distribution. Skewness, or the coefficient of skewness, examines the symmetry of the distribution. A positive skewness indicates the median is less than the mean and shows a long tail of high values to the right. A negative skewness, alternatively, indicates the median is greater than the mean with the long tail of small values to the left. Kurtosis examines the flatness or roughness of the data distribution; a negative number showing flat distribution and a positive showing peaks or a more extreme variation in the data.

The following equations were applied to define the statistics for numbers x_i , . . . x_N:

$$\text{Mean}: \quad \bar{x} = \frac{1}{N}\sum_{i=1}^{N} x_i \tag{4}$$

$$\text{Variance}: \quad \sigma^2 = \frac{1}{N-1}\sum_{i=1}^{N} (x_i - \bar{x})^2 \tag{5}$$

$$\text{Skewness}: \quad Skew = \frac{1}{N}\sum_{i=1}^{N} \left[\frac{x_i - \bar{x}}{\sigma}\right]^3 \tag{6}$$

$$\text{Kurtosis}: \quad Kurt = \left[\frac{1}{N}\sum_{i=1}^{N} \left[\frac{x_i - \bar{x}}{\sigma}\right]^4\right] - 3 \tag{7}$$

$$\text{Standard Deviation}: \quad \sigma = \frac{1}{N-1}\sum_{i=1}^{N} (x_i - \bar{x}) \tag{8}$$

where N is the total number of data, x_i is the value at the first position, $\bar{x}$ is the mean of the set of values and σ is the standard deviation of the set.

Upscaling was performed on each statistic calculated from the core-plug to correspond with the volume scale of the well-log measurements using the equation:

$$P_V = P_v \cdot \frac{1 - \bar{\Gamma}_v}{1 - \bar{\Gamma}_V} \tag{9}$$

where P_V is the statistical parameter for the larger volume of investigation, P_v is the statistical parameter for the smaller volume of investigation, Γ_v is the normalized point-scale sill in v and Γ_V is the normalized point-scale sill in V. Equation (9) is based on the correction applied to upscale the sill on the variogram by reason that variance forms the basis of the statistical parameters, utilized in the MIMC method, which correlates with the variance traced to the co-variance equation (Journel & Huijbregts, 1978; Frykman & Deutsch,1999; Tilke, Allen, & Gyllensten, 2006).

A non-dimensional measure of misfit function is applied to compare the statistics from the core-plug and the well-log by:

$$M(x) = \sqrt{\frac{(T(x) - T)^2}{\sigma^2}}, \tag{10}$$

where $M(x)$ is the misfit at the depth x, $T(x)$ is the observed well-log statistic at that depth, T is the reference plug statistic and σ^2 is the variance between the well-log statistic, at the depth where the core was sampled, and the corresponding plug upscaled statistic. The lower the misfit measure the more similar the data are to each other.

Using the misfit parameters for variance, skewness, kurtosis and standard deviation, the group average absolute deviation, $\bar{\Delta}$, a measure of dispersion or variability is calculated at each depth:

$$\overline{\Delta}\,(\mathrm{x}) = \frac{1}{N}\sum_{i=1}^{N}(M_i x - \bar{M}x)\,, \tag{11}$$

where $M_i(x)$ is the misfit parameter, *i*, at the depth *x* and $\bar{M}x$ is the central tendency or mean at depth *x*. This group misfit deviation value then is transformed as:

$$C_m\,(x) = \frac{1}{\overline{\Delta}\;(\mathrm{x})}\,, \tag{12}$$

where $C_m\,(x)$ is the correlation "constant" at the depth *x*, the larger the value of C_m the better the fit or correlation to the data. The introduction of this deviational parameter of misfit serves to search the position of an 'equally-likely' event of occurrence which is the minimal misfit with equal probability. Therefore, where the depth produces the greatest value of *C* the CT or smaller volume data likely derives from this location. This multiplicative inverse misfit correlation (MIMC) approach is presented as:

$$C_m\,(x) = \frac{N}{\sum_{i=1}^{N}(Mx_i - \bar{M}x)}\,. \tag{13}$$

Assuming a Gaussian uncertainty, the likelihood function, which reveals the depths that have a better fit to the core statistics, is calculated by:

$$L_i(x) = e^{-M(x)^2}. \tag{14}$$

where $L_i(x)$ is the likelihood parameter, *i*, at depth *x*, and *M*(*x*) is the misfit at the depth *x*. As the likelihood increases the more completely the model fits to the data. Misfit and likelihood are calculated for each parameter. Pawitan (2001) explains that the likelihood function uses unknown quantities to express information about the data. The likelihood function is especially suited for dealing with uncertain data or parameters as the information contained in a parameter leads to an unbiased evaluation of the data. Likelihood compares the models

to determine how well the information is portrayed in the data and then quantifies the amount of variation.

Using the likelihood parameters for variance, skewness, kurtosis, and standard deviation the group average deviation, $\overline{\Delta}$, was calculated at each depth:

$$\overline{\Delta(x)} = \frac{1}{N}\sum_{i=1}^{N}(L_i(x) - \bar{L}(x)) \quad (15)$$

where $L_i(x)$ is the likelihood parameter, *i*, at the depth *x*. This group likelihood deviation value was transformed using equation:

$$C_l(x) = -\ln(\overline{\Delta}(x)) \quad (16)$$

where $C_l(x)$ is the logarithmic deviational likelihood at the depth *x*. The deviational parameter of likelihood similarly searches for the position of an 'equally-likely' occurrence event. Again, the larger the value of *C,* the better the fit or correlation to the data.

The likelihood function frequently educes extremely small values from the parameters, $< 1 \times 10^{-6}$, which necessitates a transformation to result in true correlation extremes and ease the identification of the best depth correlation. To account for these values, set the average deviation value to 1; this results in true correlation extremes and eases the identification of the best depth correlation. The parameters at the best depth fit do not contain the particularly small values and thus are unaffected by the correction.

Entropy reveals areas of data that have high amounts of uncertainty with little information about the data; this is interpreted to mean that it performs similarly to natural systems. Entropy was determined using the equation:

$$H = -K \sum_{i}^{I} p_i \ln p_i , \tag{17}$$

where p_i is the normalized parameter at depth i and K is a constant. Entropy was implemented to determine which parameters would reveal the most information in the data.

3.3 Scaling Process

The scaling process has two components: upscaling, which reduces the dimension of data into a lower resolution, and downscaling, which adds more dimensions and increases the overall resolution. Upscaling, generally achieved by averaging cell values, reduces the amount of data to process allowing for multiple model derivations while preserving formation details. Concurrently, downscaling creates a more accurate and vibrant model that permits greater simulations. While upscaling is a stress-free procedure, downscaling is far more problematic.

The main purpose of upscaling is to reduce the amount of data that needs to be worked with for modeling processes. This allows for less computationally-intense models, easier transport of the data, and the ability for retaining many large-scale features found within the high-resolution image. The simplest method of upscaling consists of the averaging of data points:

$$\bar{A} = \frac{1}{4}\{X_m(i,j) + X_m(i,j+1) + X_m(i+1,j) + X_m(i+1,j+1)\} \tag{18}$$

where X_m is the data value at m-th cell, $\bar{A}$ is the mean value of four X_m, i is the x coordinate of m-th cell, j is the y coordinate of m-th cell (Harris & Foufoula-Georgiou, 2001). The above formula will average the data evenly while preserving the two-dimensional scale of the

collected data. Nonetheless, upscaling aggrandizes the amount of uncertainty in estimation due to the nature of averaging.

Downscaling increases the amount of data while assigning values to locations that normally are lacking data. Simulation algorithms, such as kriging and SGS, are capable of large volume estimations of unknown values. This converts a coarse-scale data, or low-resolution scale, to fine-scale data. The SGS method generates multiple realizations of the downscaling results at the same time honoring the spatial variance of the data.

3.4 Scaling with Sequential Gaussian Simulation

The formation data structure and variations across the reservoir appear in variograms producing a spatial statistical representation. An omni-directional variogram or variogram map portrays the anisotropy in the formation. The data is then fit to the experimental variogram using a model such as Gaussian, exponential or spherical distributions and determining the nugget effect, sill and appropriate range. This defines the model variogram which kriging applies in downscaling.

A three-dimensional Cartesian block is created for each dataset to allow for the SGS and kriging algorithms. The well-log dataset is interpolated to reservoir scale using simple kriging, SK, and then a co-simulation performed with the CT dataset. The model variogram created from the CT plug data functions in the sequential Gaussian co-simulation with the reservoir scale well-log porosity to constrain the data. Then the algorithms are processed through a double-stepping process, to upscale and then downscale the data, in an attempt to better preserve the details in the reservoir.

CHAPTER 4

APPLICATIONS OF THE MODEL: CASE STUDIES

4.1 Case Study Overview

Two formations originating from dissimilar depositional environments were chosen to study, in order to test the applicability of the geostatistical scaling model to multiple settings. The first formation, located in the southeastern region of Korea, is understood to a lesser degree with investigations into petrophysical opportunities currently ongoing. The second formation in Kansas, currently under production for oil and gas, has been intensely studied.

4.2 Case Study: Jinju Sub-basin, Republic of Korea

The Korean peninsula tectonically links the Japanese Arc to eastern China. During the Mesozoic, the land rested directly at the hindmost section of a subduction-zone-created magmatic arc. The Mesozoic orogenic events produced the mountain regions and basins, dominating Korea, which lie in a predominately northeast-southwest orientation.

The Gyeongsang Basin, the largest basin, forms the southeastern part of the peninsula as a result of crustal extension associated with volcanic activity (Paik & Lee, 1995). Through the Cretaceous, the Gyeongsang Basin filled with approximately 9 km of succedent layers consisting of non-marine sediments and volcanic deposits that have been separated into three major stratigraphic units, in ascending order: the Sindong, Hayang and Yucheon groups

(Chough & Sohn, 2010). The sedimentation occurred in an interior continental region during a semi-arid paleo-climatic environment.

The Jinju sub-basin, located in the southwest area of the Gyeongsang Basin, is composed of low dipping strata and contains approximately seven formations within the Sindong Group. The Sindong Group, dating from middle-early Cretaceous, consists of terrigenous sandstone, conglomerate, shale and mudstone deposited in lacustrine and alluvial environments, some two to three thousand meters thick (Chough & Sohn, 2010). Faults, which cut through most of the Gyeongsang Basin, are rare in the Jinju basin leaving the area untouched by major deformation.

The Jinju Formation ranges from 750 meters to 1,200 meters thick and is composed of mudstone and intercalcalated sandstone, as seen in Figure 4.1. Petrological studies of the formation reveal the sediments derived from erosion of pre-Cambrian gneiss and schist, and Jurassic granite (Chough & Sohn, 2010). The mudstone that generally comprises the formation formed from marginal lake to deeper lake deposition and sandstone accumulated from meandering braided stream channel deposits. A layer of mudstone displays soft-sediment deformation characteristic of nearby seismic activity.

Figure 4.1, Jinju Formation in outcrop at Bitori-do Island, Korea

An exploratory core was drilled near the town of Jinju, located in the southwest region within the Gyeongsang Basin, and penetrated through only one geologic unit within the Sindong Group, the Jinju Formation. As Figure 4.2 depicts, the 60 meter long core exhibited distinct multiple layering of light-gray sandstone and a darker-gray mudstone, characteristic of the formation where seen in outcrops. Porosity was determined by averaging the values calculated with the long-spaced density (LDS) and the high-resolution density (HRD) tools as ascertained by Kim, Suh, & Kim (2001).

Figure 4.2, Photo of core showing the darker-gray mudstone and lighter-gray sandstone

The well-log instruments recorded measurements every 0.02 meters for depths from 6.51 meters to 64 meters then a linear averaging was performed to bring the measurements to every tenth of a meter. For CT data, the readings from 12.01 meters to 12.51 meters were selected followed by random number generation every 0.02 meters in order to have data every hundredth of a meter, or every centimeter, using the random number function:

$$= \text{RAND}(\,) * (X_2 - X_1) + X_1\,, \tag{19}$$

where X_2 represented the larger number and X_1 represented the smallest number in the range of interest.

Statistics for mean, variance, skewness, kurtosis and standard deviation were generated on the porosity data for the entire CT core length, 0.5 meters, as well as on a moving window within the well-log data on intervals corresponding with the core length. Histograms and variograms for the Jinju data were created as well to in order to run the statistics and upscale the CT data for the MIMC method. However, SGS was not performed on the Jinju data on account that data from a single well cannot render field distribution of porosity.

4.3 Results for Jinju Sub-basin, Republic of Korea

Following the creation of the histograms (Figures 4.3 and 4.4) for the well-log data and CT plug data the variograms were designed (Figures 4.5 and 4.6). The experimental variograms, for both the well-log and CT data, were assigned twenty lags. The well-log variogram lags were spaced at a distance of 4 meters and a tolerance of two meters. The CT variogram lags were spaced at a distance of 0.03 meters with a 0.015 meter tolerance.

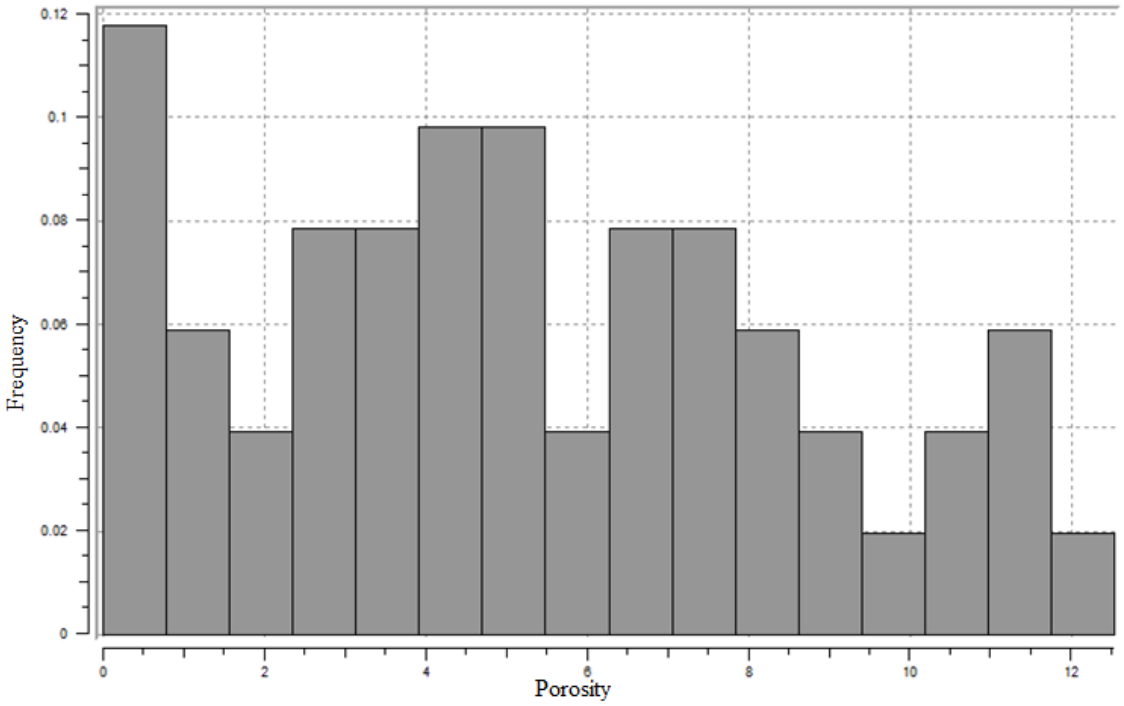

Figures 4.3, Histogram showing distribution of Jinju well-log data

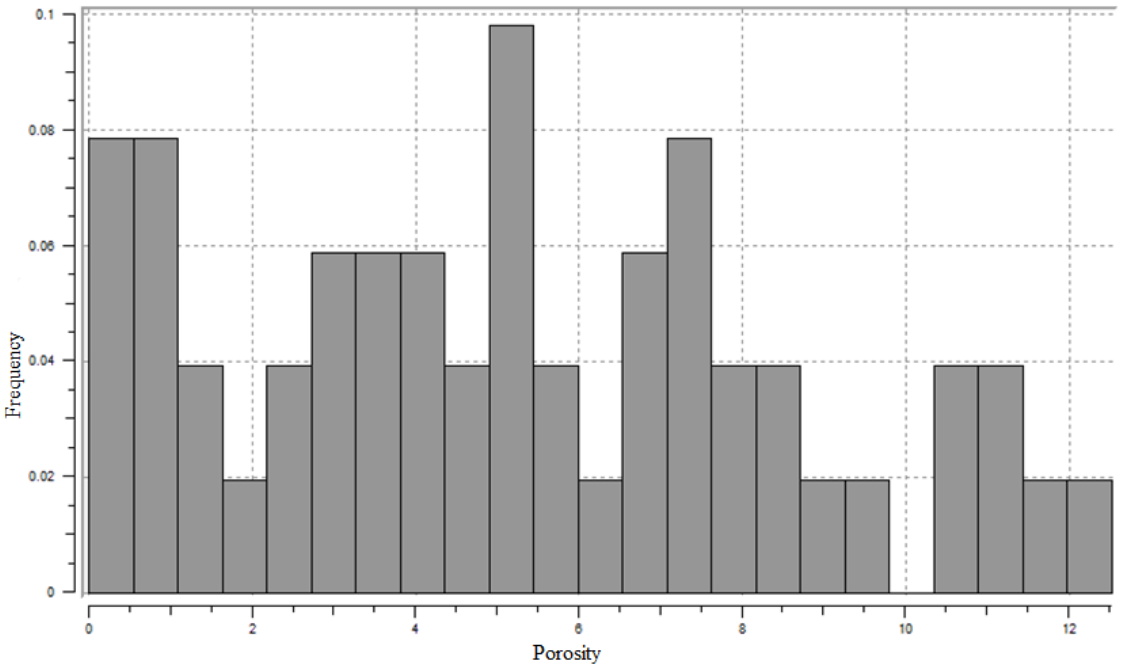

Figures 4.4, Histogram showing distribution of Jinju CT data

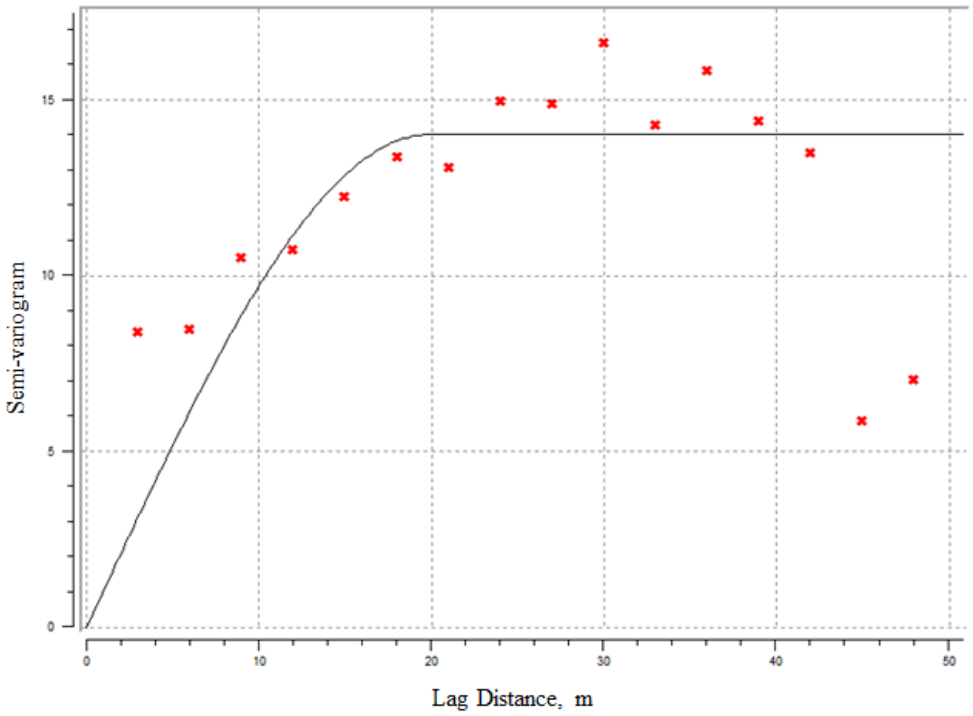

Figure 4.5, Variogram at 1 meter well-log scale of Jinju well

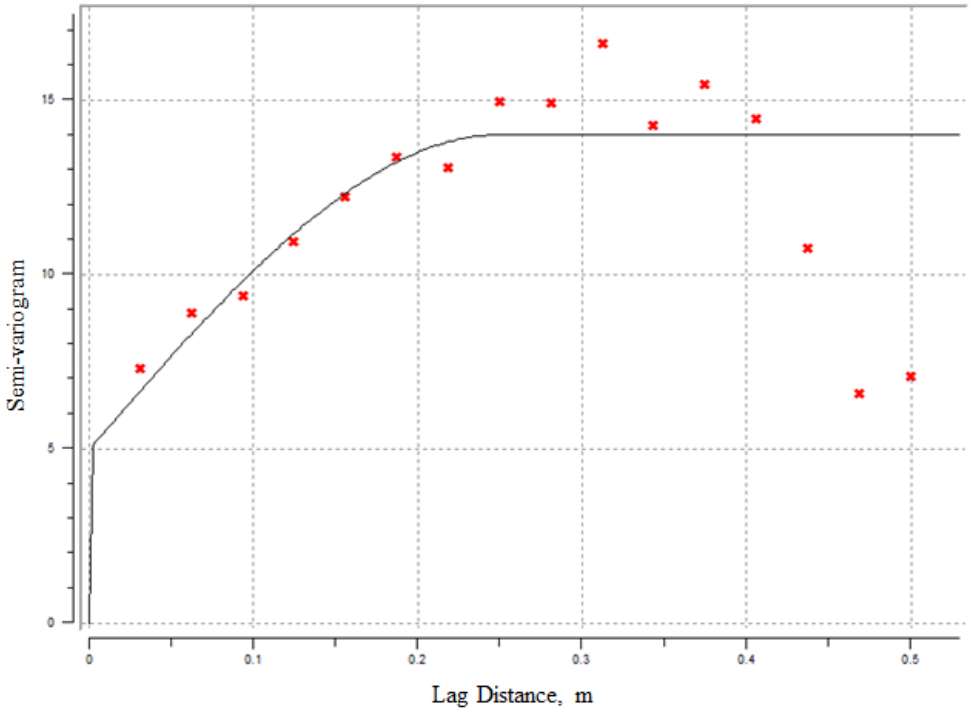

Figure 4.6, Variogram at 0.01 meter CT scale of Jinju well

The sill, for each subsequent model variogram, was noted for both data sets in order to assign the volumes when upscaling the plug data. The basic statistics were calculated with a moving window for the well-log data and the CT data over the length of the core plug, 0.5 meters. The CT data was then upscaled using the parameter scaling equation (Equation 9).

The misfit and likelihood algorithms compared the well-log and CT porosity values on both upscaled parameters and non-scaled parameters at every depth for the Jinju well. The upscaled parameters demonstrated a better likelihood result than the non-scaled parameters especially at the 12 meter depth (Figures 4.7 and 4.8). However, the low likelihood values derived from the likelihood function could not clearly establish a correlation for the CT values within the well-log values.

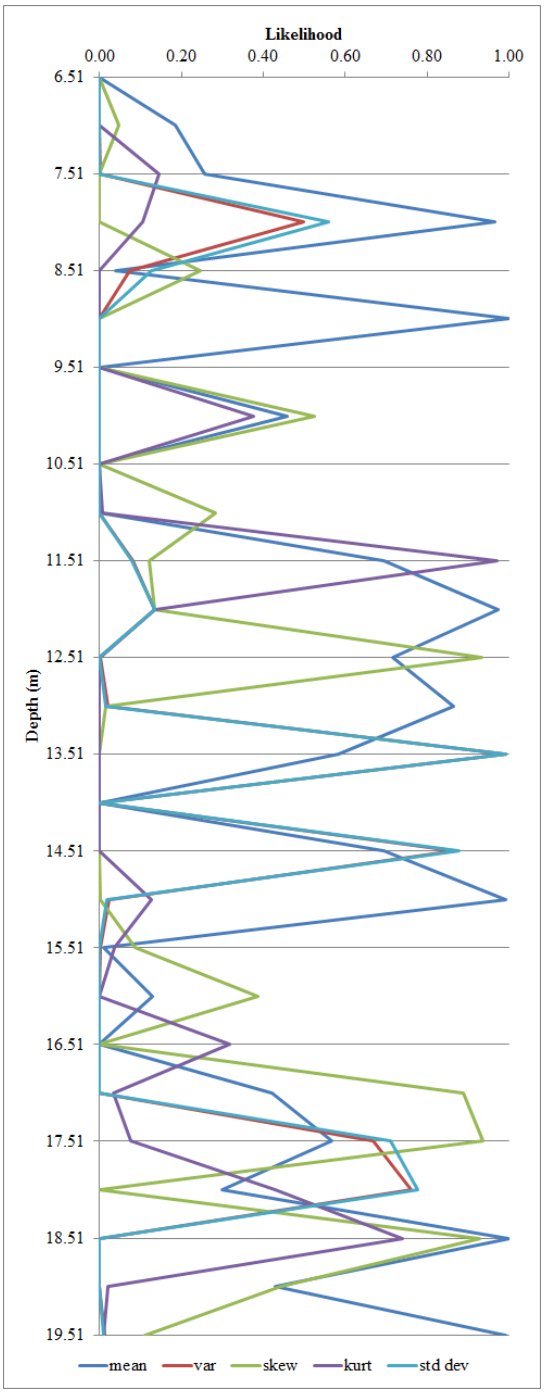

Figure 4.7 Graph showing non-scaled likelihood results, Jinju well

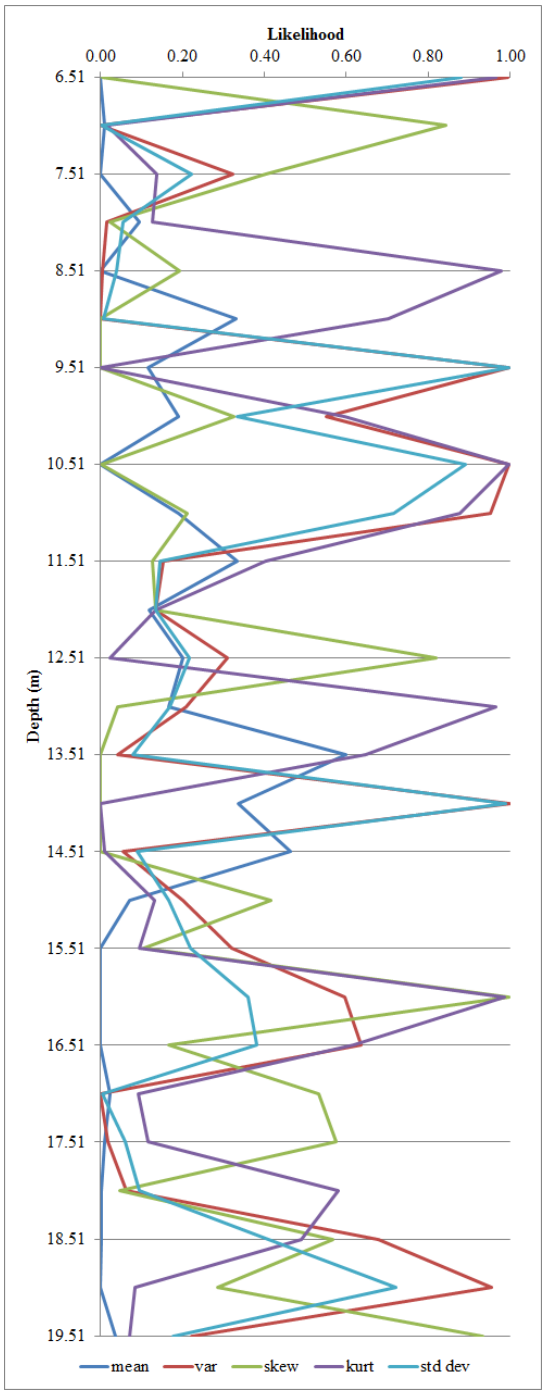

Figure 4.8 Upscaled results showing likelihood to depth, Jinju well

The entropy results, Figure 4.9, showed no parameter was significantly lacking information which suggests that every parameter could be incorporated into the MIMC method. Lower entropy values reflect differentiation capabilities and the values documented in the Jinju data are all very small and comparable to each other (Price et al., 2008). When the MIMC method was executed twice, one with the mean and one without the mean, the results did not change.

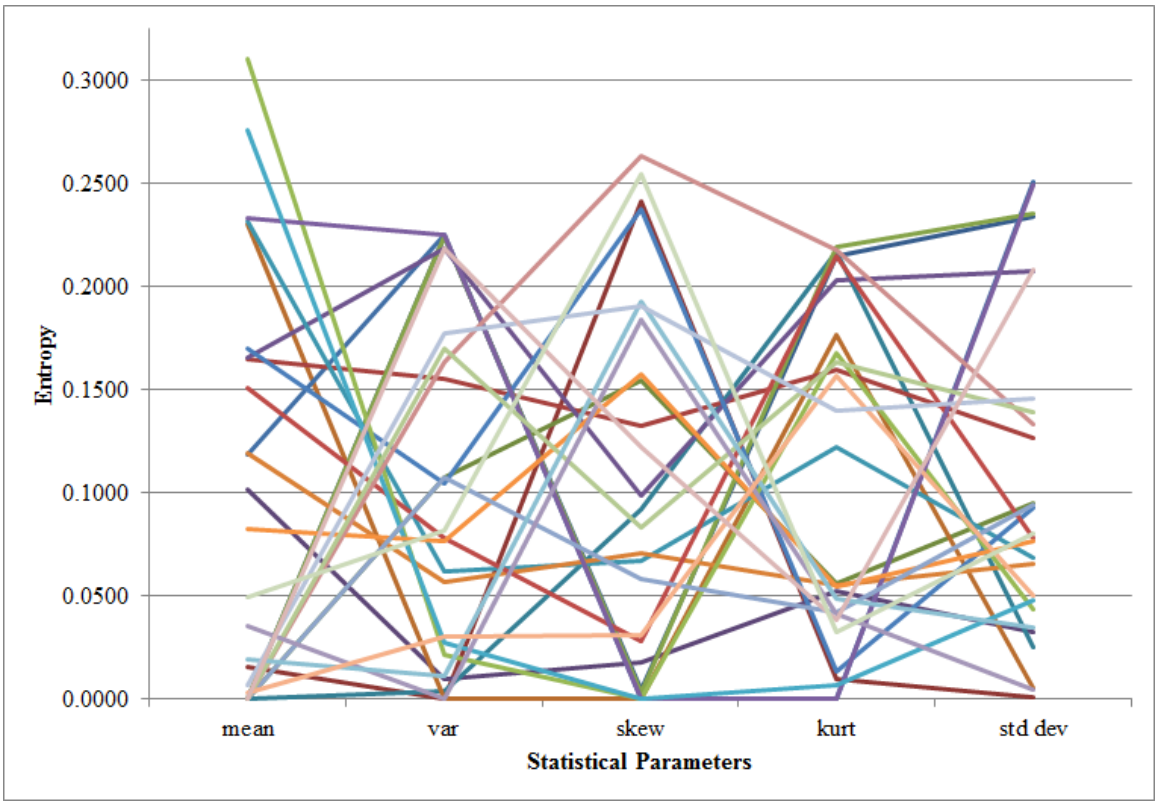

Figure 4.9 Entropy for Jinju for each likelihood function per data window

The statistical parameters derived from misfit (Equation 10) were transformed by implementing the MIMC method (Equation 13) and subsequently the results improved. The depth of twelve meters, from which the CT porosity originated, became unmistakably evident as seen in Figure 4.10.

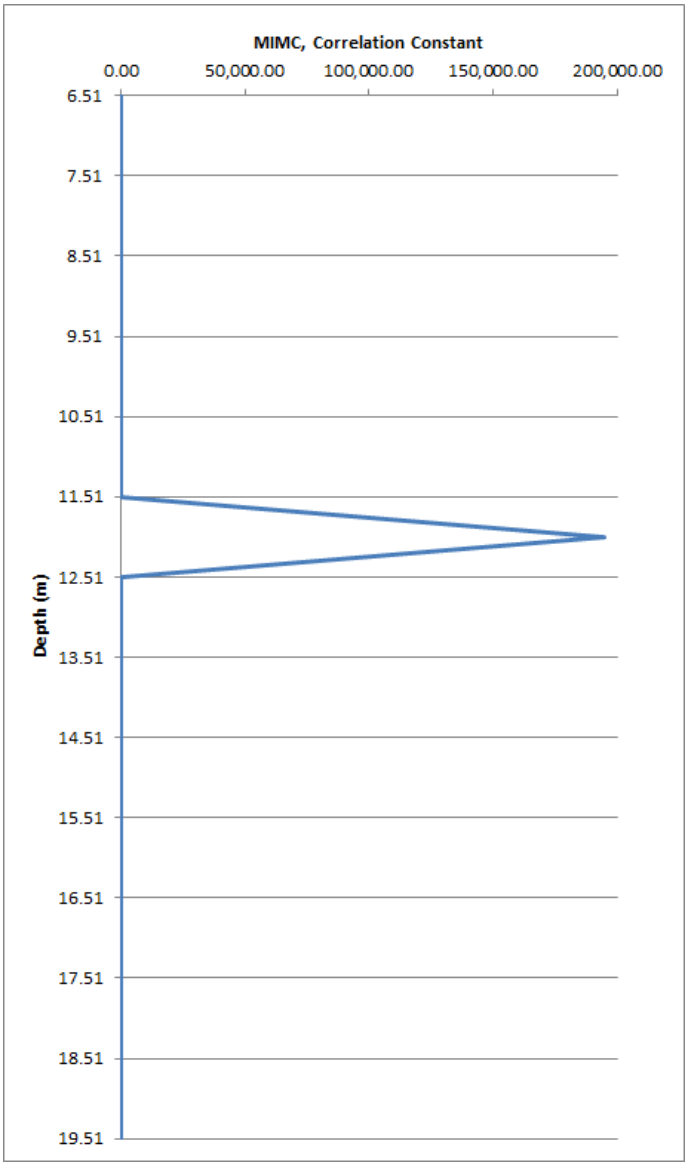

Figure 4.10 Jinju data showing correct correlation depth after using MIMC

4.4 Case Study: Panoma Gas Field, Kansas

A group of gas wells were drilled in Grant County in the southwestern corner of Kansas in a section of the Panoma Gas Field (Figure 4.11). This field lies underneath a section of the Hugoton embayment, a keel-like extension of the larger and deeper Anadarko Basin that stretches through Texas and Oklahoma. A massive trough forms the Hugoton embayment arranged in a southward orientation and uplift on the north, west and east (Carr & Sawin, 1996). The Hugoton Field has the capability to produce 70 trillion cubic feet of gas, making it one of the largest gas fields in the world (Newell, Watney, Cheng, & Brownrigg, 1987).

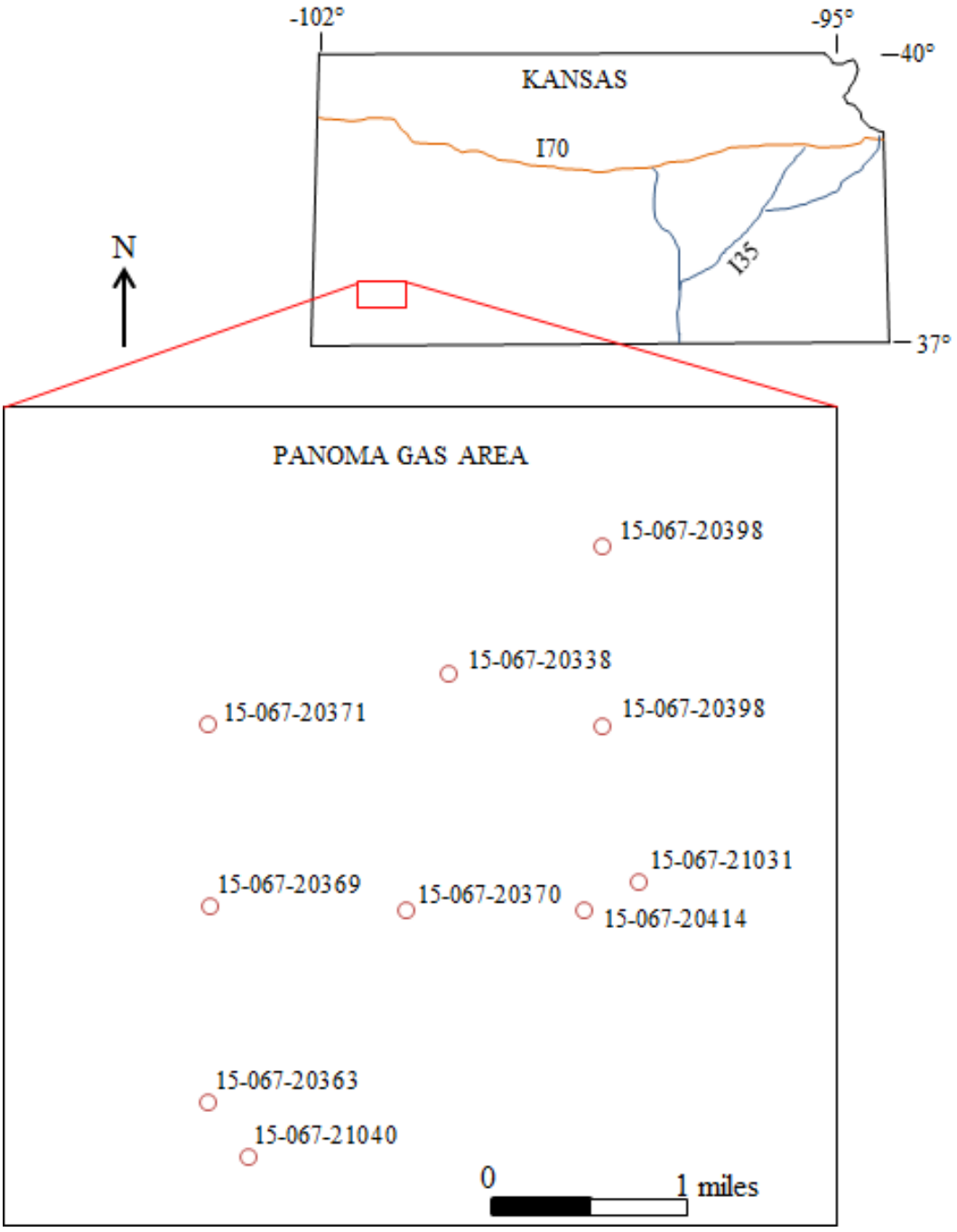

Figure 4.11, Site map of wells in the Panoma Gas Field, Grant County, Kansas

The producing formation for these wells is the Council Grove Group of Lower Permian age, with a formation top depth around 1800 feet (Figure 4.12). During the Permian, this area rested in an immense transgressing and regressing marine environment forming characteristic cyclothems. The Council Grove Group comprises intercalcalated limestones and shales. The limestones, vacillating from wackestones to dolomites, and the shaley silt mudstones developed in a shallowing marine environment (Newell et al., 1987).

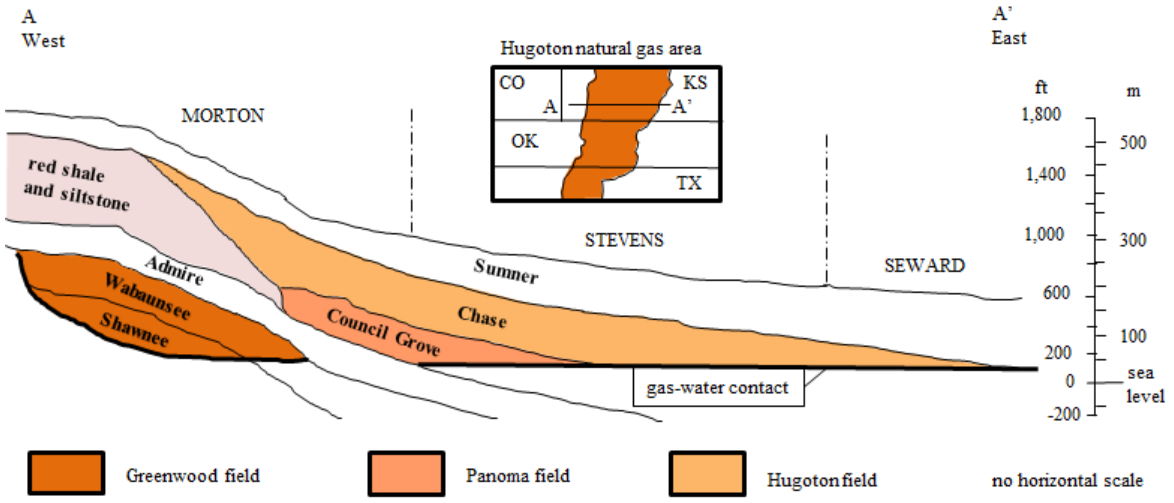

Figure 4.12, Cross section of Hugoton and Panoma Field, (adapted from Carr & Sawin, 1996)

The datasets came from eleven Log ASCII Standard (LAS) files downloaded from the Kansas Geological Survey and focused on a small section of the Council Grove Group in the Panoma Gas Field. Measurements were taken every 0.5 feet for depths from 1800 feet to

3100 feet. Depths focusing around the 3000 foot depth were selected, limited by one hundred feet in each direction.

The porosity for the Panoma Gas Field data was derived from the grain density determined by core analysis from a section of Well 20338. The grain density, ρ_{ma}, fluctuated negligibly around the average density of limestone, 2.71 g/cc. As Well 20338 and ten nearby wells were used in this study, the assumption was made that the formation's grain density did not fluctuate wildly through the depth investigated. The fluid density, ρ_f, was assumed to be 1.0 g/cc, the density of fresh water.

The bulk density, ρ_b, was determined by inserting the identified variables from Well 20338 into the porosity equation (1) and solving for the bulk density. Then by relating the bulk density to the electron density equation (20) to the equation connecting the observed gamma intensity to the electron density (21), equation 22 is derived:

$$\rho_b = \frac{\rho_e}{A/_{2Z}} \tag{20}$$

$$\gamma_{obs} = \frac{k}{\rho_e} \tag{21}$$

$$\rho_b = \frac{k}{\gamma_{obs}} \tag{22}$$

where ρ_e is the electron density, A is the molecular weight, Z is the number of electrons per molecule, γ_{obs} is the observed gamma-ray measurement and k is a constant (Serra, 1984; Kim et al., 2001).

This formulated a constant that was applied when calculating the porosity data from the gamma-ray data available in the LAS files. The equations are based on a series of

assumptions: there is no significant amount of noise in the gamma-ray data produced by natural gamma-ray in the formation; the molecular weight to number-of-electron ratio is near unity; the grain density fluctuates nominally; and fluid density remains constant throughout the distribution.

A linear regression is performed to bring the well-log measurements to every tenth-of-a-foot for data robustness. For the CT scan data, the smaller volume measurements are chosen from a foot-long section of the larger well, and random number generation (Equation 19) is applied to create data every hundredth-of-a-foot. Histograms and variograms are generated for the well-log and CT datasets. Figures 4.13 and 4.14 are the histograms showing the porosity distribution for both the well-log and CT datasets. The omni-directional variograms for the well-log data and porosity data are shown in Figures 4.15 and 4.16. Statistics for mean, variance, skewness, kurtosis and standard deviation were generated on the porosity data for the entire CT core length, one foot, as well as on a moving window on the well-log data on intervals corresponding with the core length.

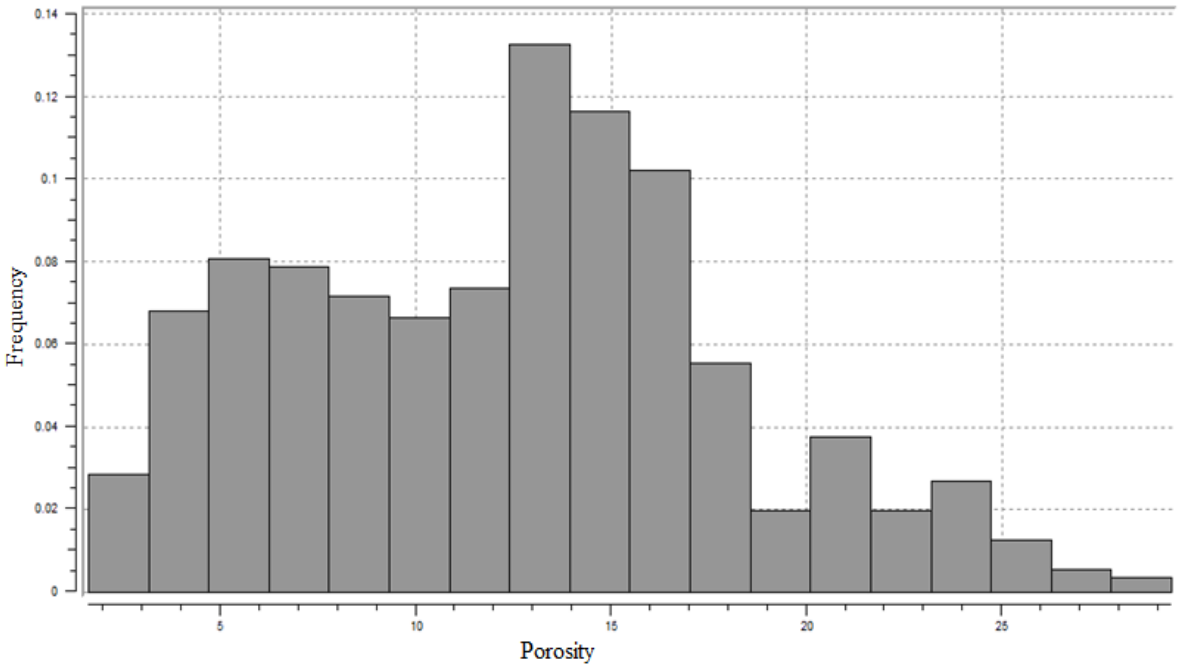

Figure 4.13, Distribution of the Panoma Field well-log data

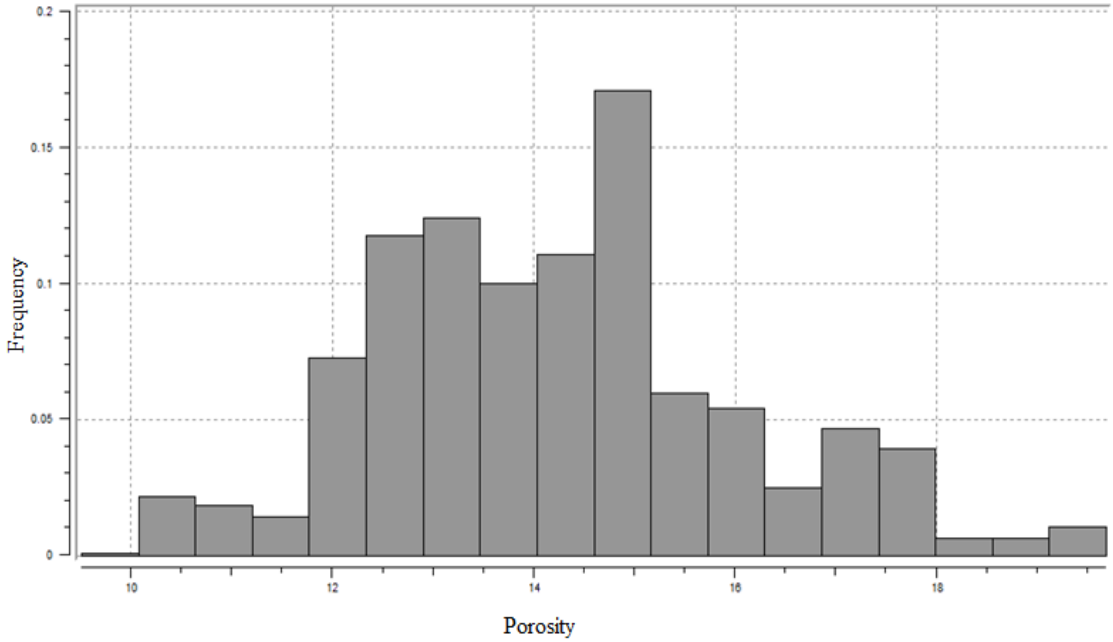

Figure 4.14, Distribution of the Panoma Field CT data

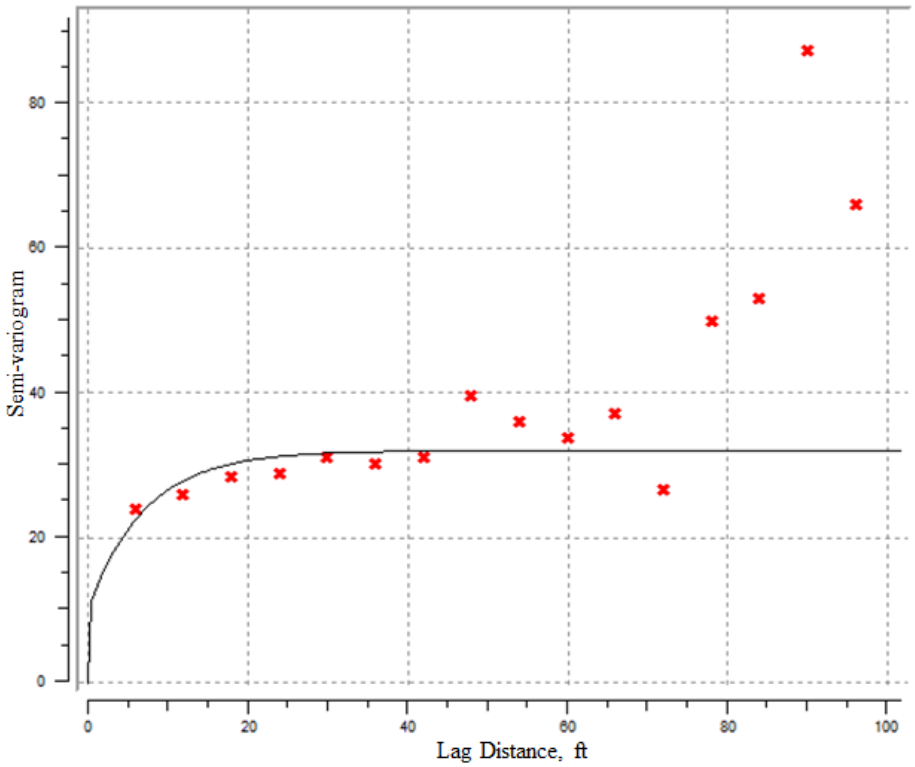

Figure 4.15, Variogram for the Panoma Field well-log data

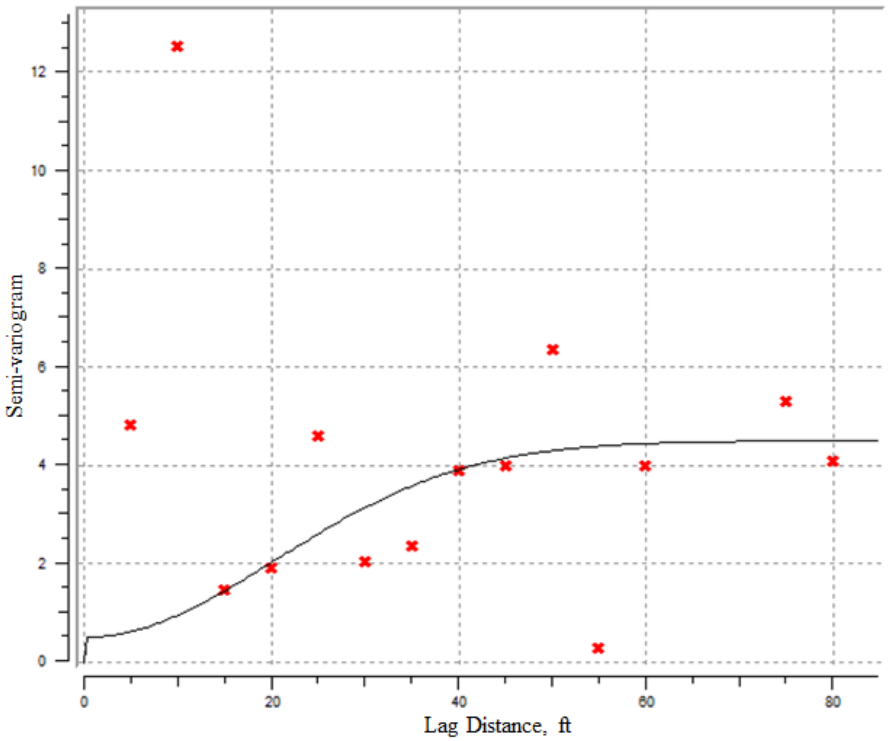

Figure 4.16, Variogram for the Panoma Field CT data

A coefficient of correlation, used in the SGcS, is determined to be 0.997 after comparing both datasets at the 3022 foot marker. The original porosity data from the Panoma Field consisted of point data that served as the backbone for basic upscaling and downscaling using SK and SGS algorithms. The geostatistical program SGeMS loaded the 3D point dataset (Figure 4.17) for the well-log data and the CT data to prepare for the integration and scaling processes.

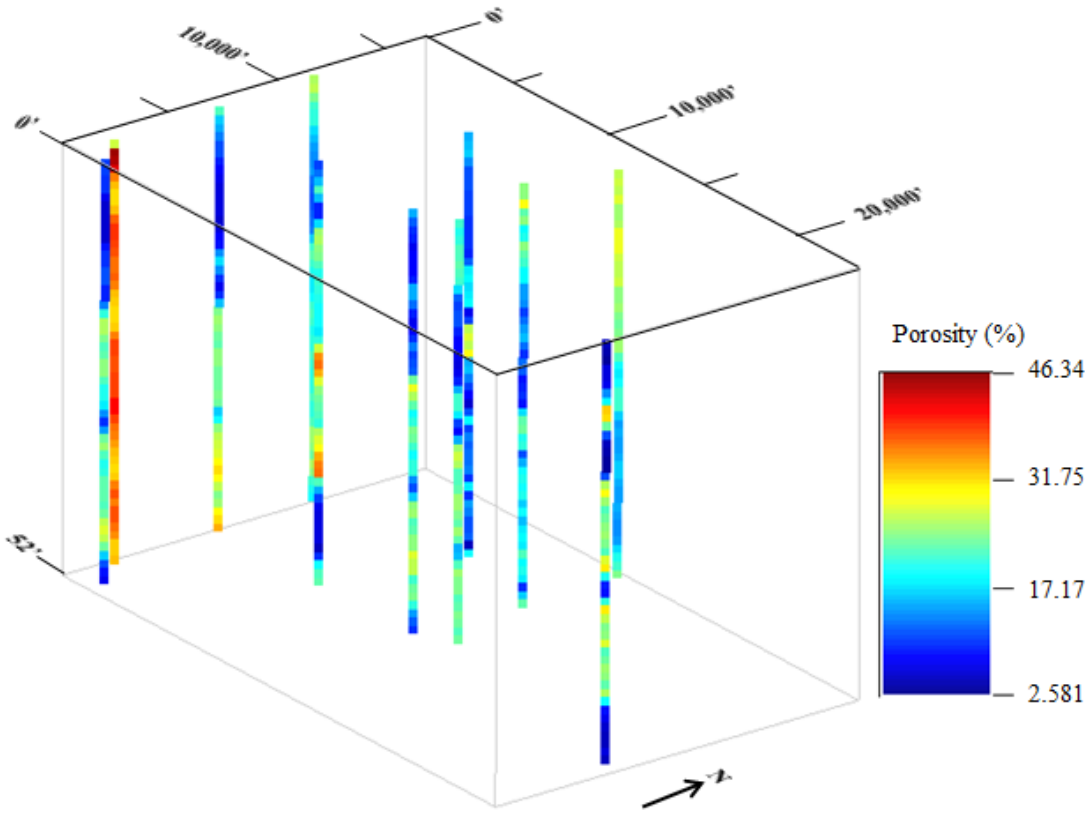

Figure 4.17, 3D point dataset of well-log porosity from Panoma Gas Field

4.5 Results for Panoma Gas Field, Kansas

A model variogram was created for all eleven Panoma Gas Field wells at both the well-log scale and the CT scale, in order to define the sill values for the scaling relationship in the upscaling equation (Equation 9) for each well. The well-log experimental variograms were constructed using 20 lags at a distance of eight feet and the tolerance set to four feet. The CT experimental variograms also had twenty lags used in their creation but the lag distance was 0.0625 feet with 0.0313 feet for the lag tolerance. Figures 4.18 and 4.19, the variograms for Well 20369, are characteristic of the results demonstrated in the Panoma Gas Field data. The remaining variograms for each well are located in the Appendix.

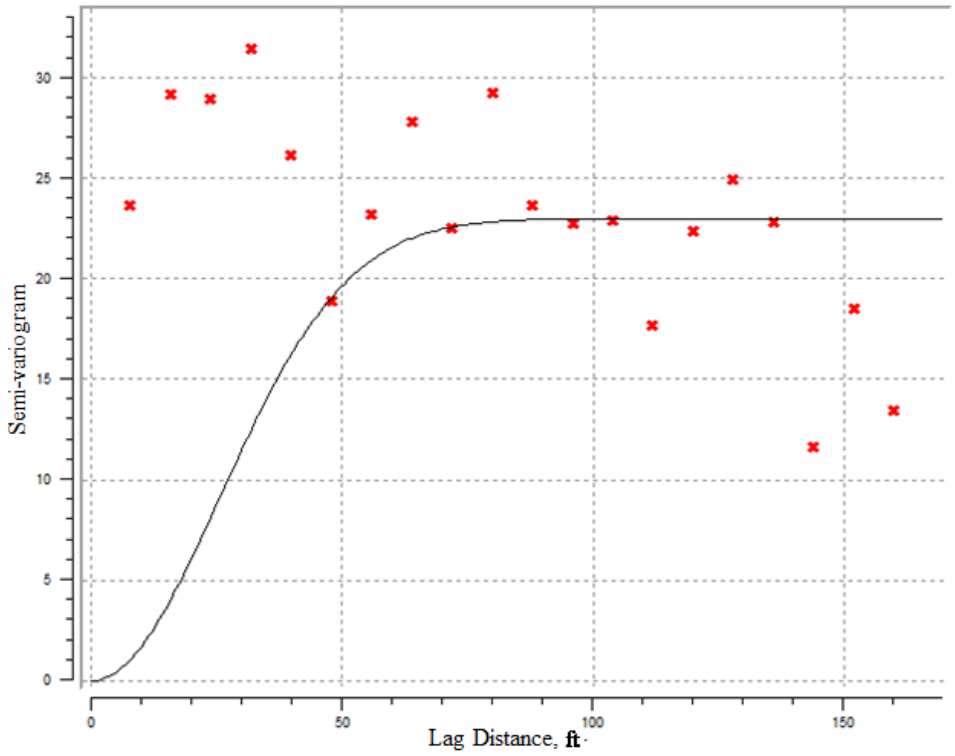

Figure 4.18 Variogram for well-log scale of Well 20369

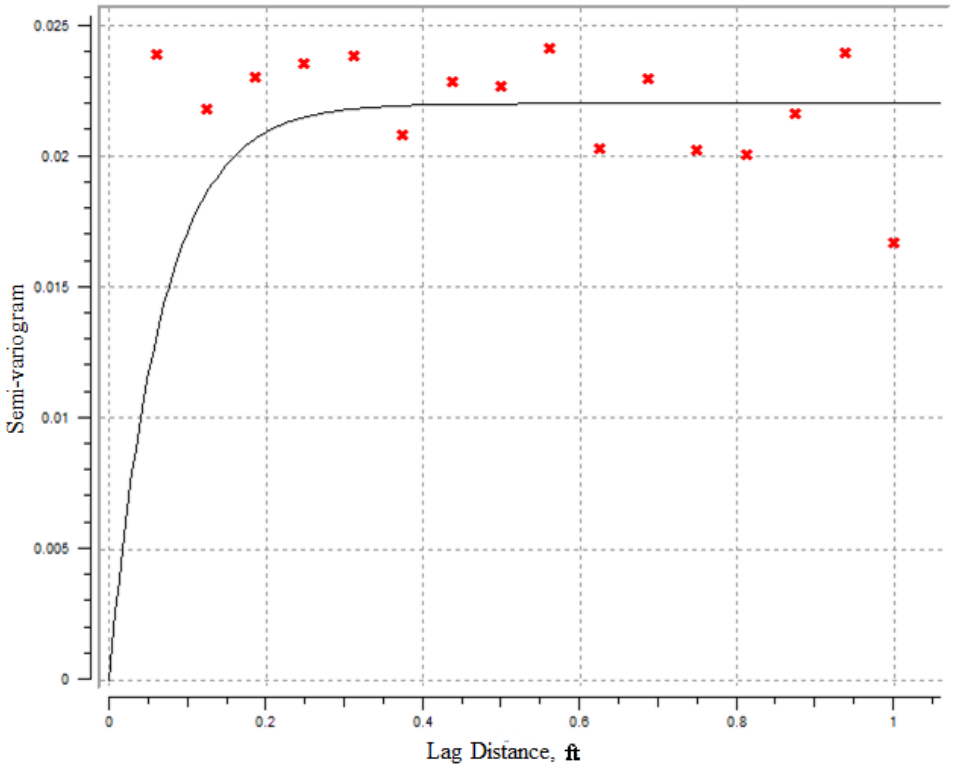

Figure 4.19 Variogram for CT scale of Well 20369

The porosity values from the Panoma Gas Field for both the well-log data and the CT data also were evaluated using the misfit and likelihood functions on the upscaled and non-scaled statistical parameters. Figures 4.20 through 4.23 show the Panoma Gas Field data for two wells, 20363 and 20370. The graphs illustrate the results from the likelihood function on the upscaled parameters and the results following the MIMC method. Recall that the greatest peak indicates the largest correlation constant and denotes the depth correlation. The graphs showing likelihood and MIMC results, using misfit, for the remaining Panoma Gas Field wells can be found in the Appendix.

Much like the Jinju data, the Panoma Gas Field data displays a point of coalescence following transformation with the likelihood function on the scaled parameters; however, the convergence of the parameter value is often indistinguishable within the disorder of the graph. Furthermore, as seen with the Jinju data, the correlation with depth distinctly emerged following the transformation of the misfit values with the MIMC method. The likelihood results also patently revealed the depth after the MIMC transformation.

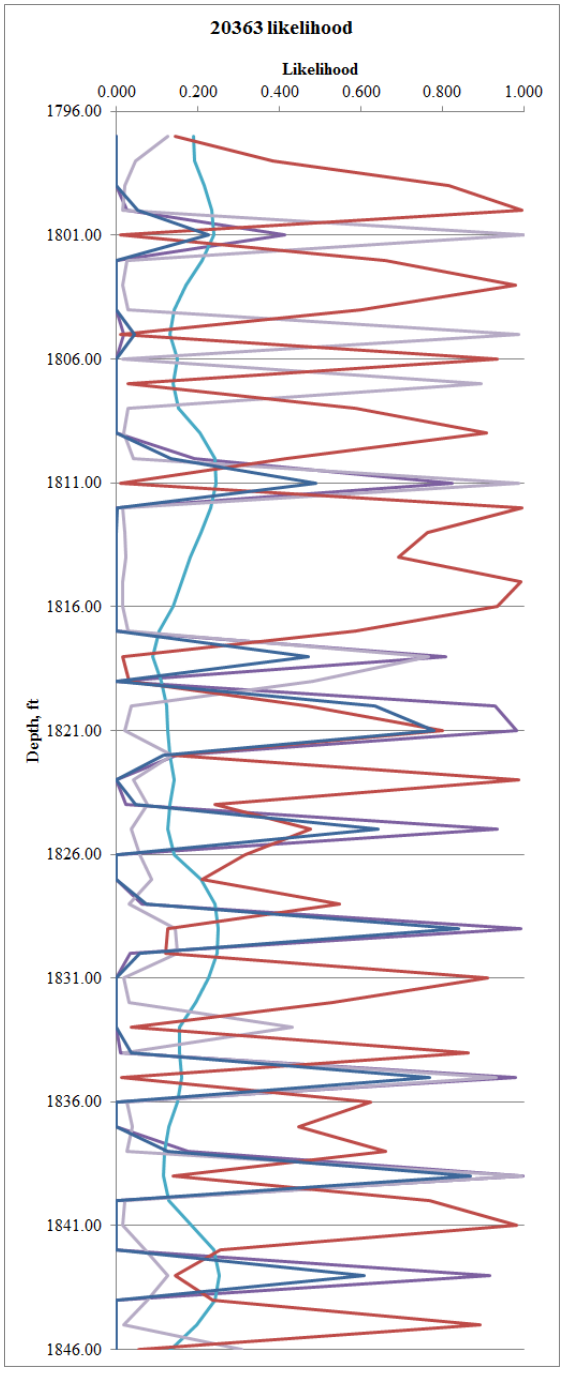

Figure 4.20 Likelihood for Well 20363

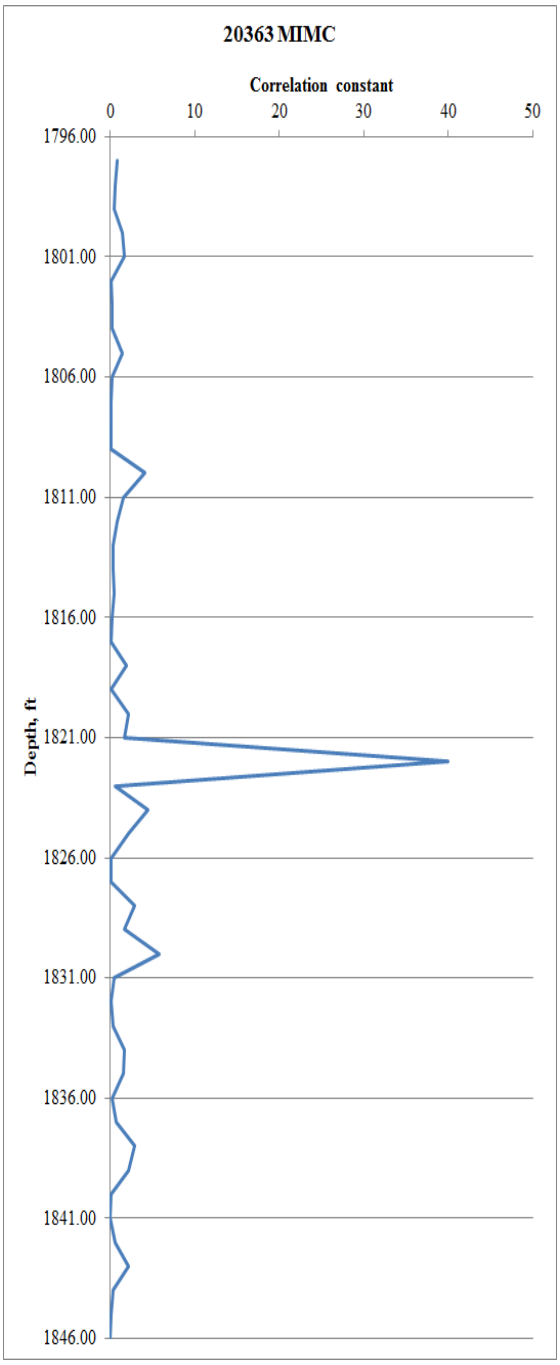

Figure 4.21 MIMC for Well 20363

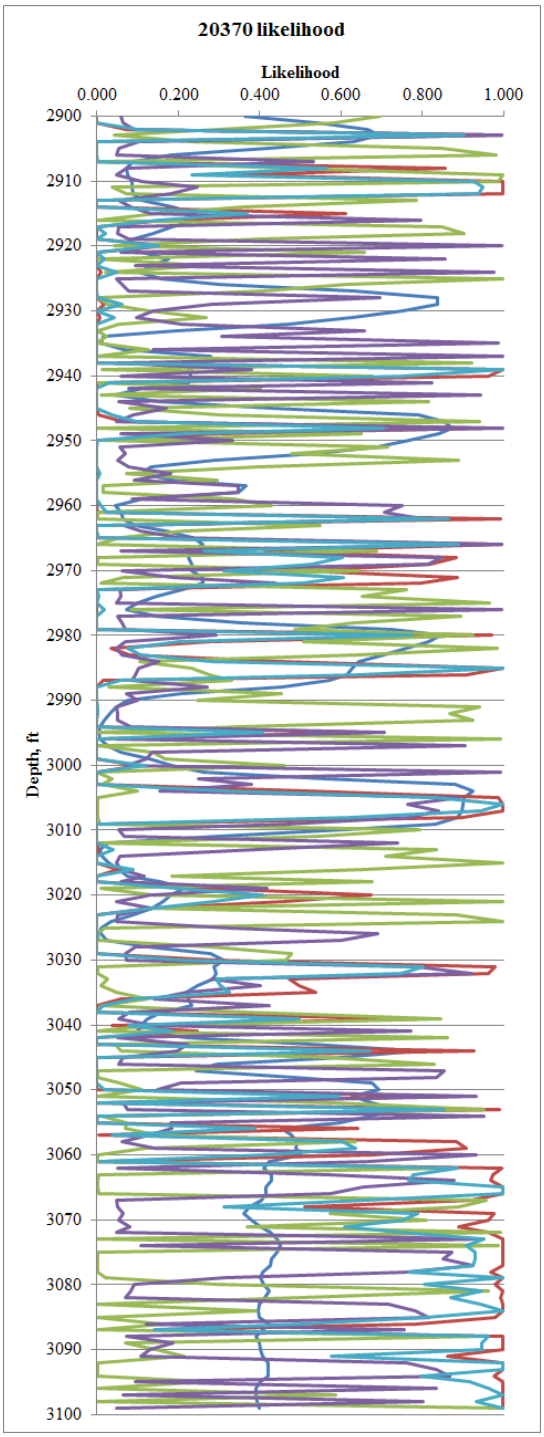

Figure 4.22 Likelihood for Well 20370

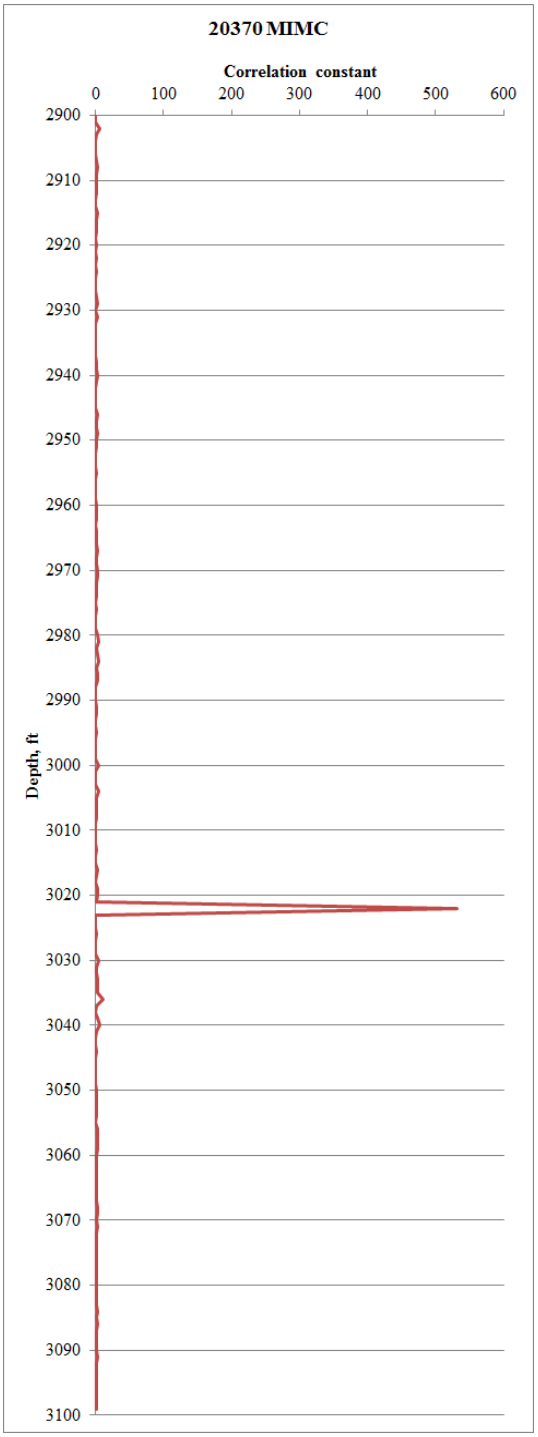

Figure 4.23 MIMC for Well 20370

4.6 SGS Results for Panoma Gas Field, Kansas

A 3D Cartesian grid of size 80 x 50 x 52 was specified with the cell dimension set to 1 x 1 x 1 on which to perform the SK and SGS interpolations. The well-log porosity data from the Panoma Gas Field was then interpolated to the reservoir field extent. This interpolation was accomplished through SK (Figure 4.24) and then with SGS (Figure 4.25) to determine the best method for retaining porosity distribution information. Both interpolations applied the model variogram calculated from the well-log data.

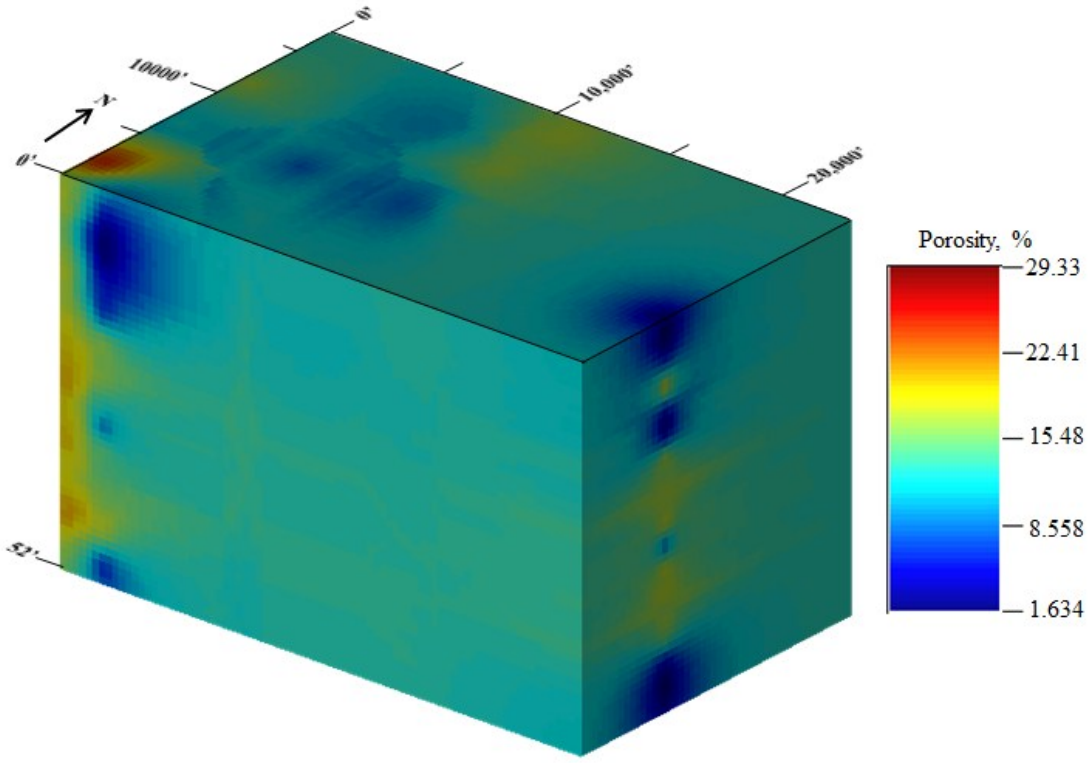

Figure 4.24, Interpolation of Panoma Gas Field to 1x1x1 cell size using SK

The SGS (Figure 4.25) used simple kriging in order to maintain a target distribution and a smoother interpolation. The search ellipsoids specified for the SGS method had ranges set at 25 feet while the SK estimation used ranges of 40 feet. Both had azimuth, dip and rake fixed to zero and involved 20 for the conditioning data.

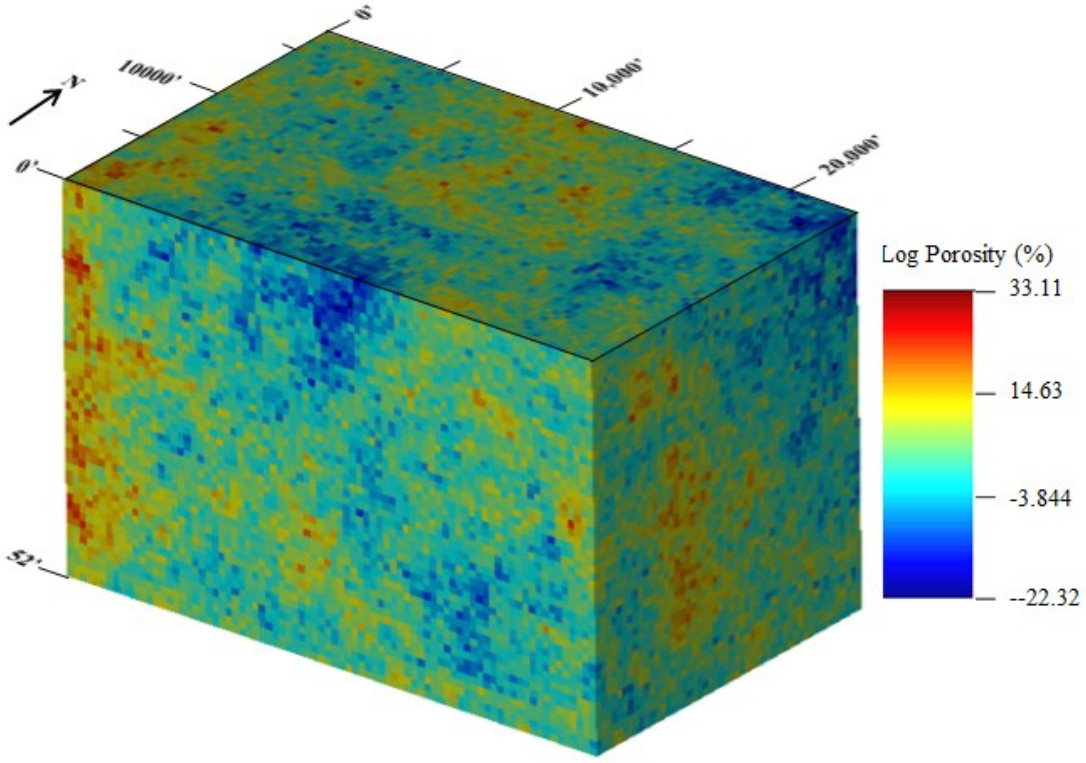

Figure 4.25, Interpolation of Panoma Gas Field to 1x1x1 size using SGS

A 3D Cartesian grid of size 17 x 10 x 11 was specified for upscaling with the cell dimension set to 5 x 5 x 5. Averaging of the data points upscaled the well-log data to the 5 x

5 x 5 scale on the SGS interpolation (Figure 4.26) and the SK interpolation (Figure 4.27) where the well-log porosity distribution is still visible in the coarser resolution. SGcS brought in the CT porosity data to constrain the well-log porosity to the higher porosity resolution of the CT data. Since a larger volume support for the secondary variable is required for Markov Model 2, MM1 is chosen for the co-kriging method (Remy et al., 2009).

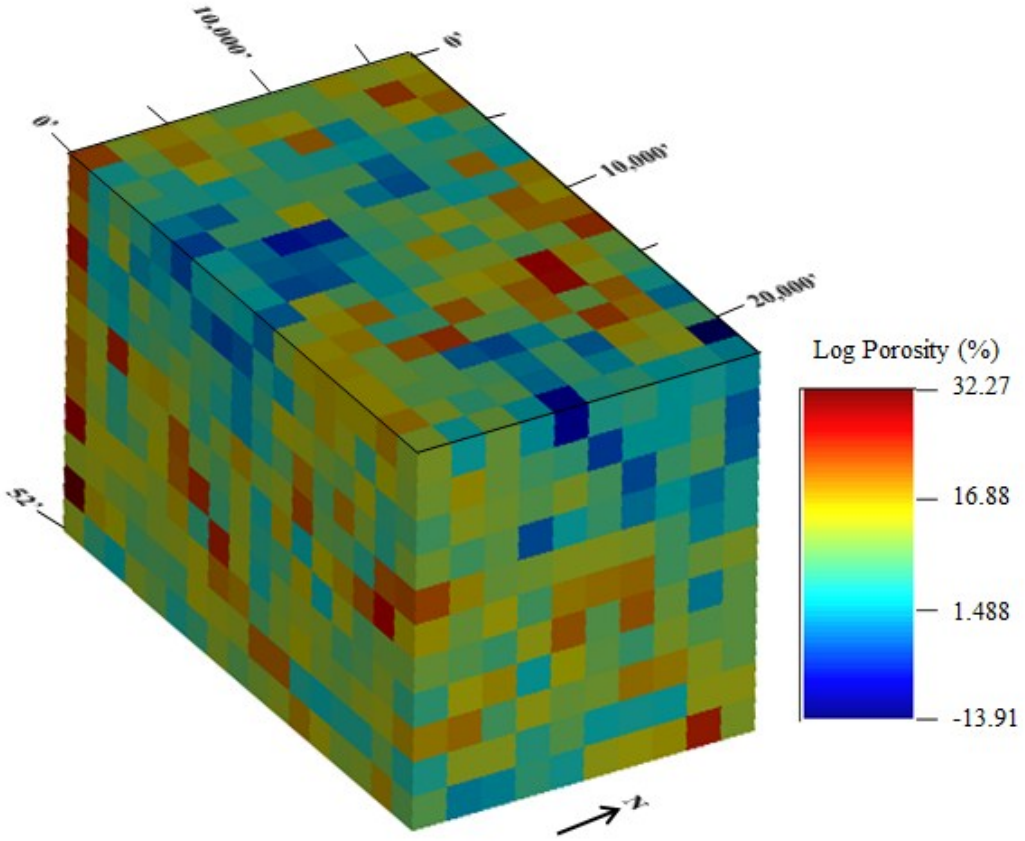

.

Figure 4.26, Upscaled Panoma Gas Field to 5x5x5 cell size from SGS

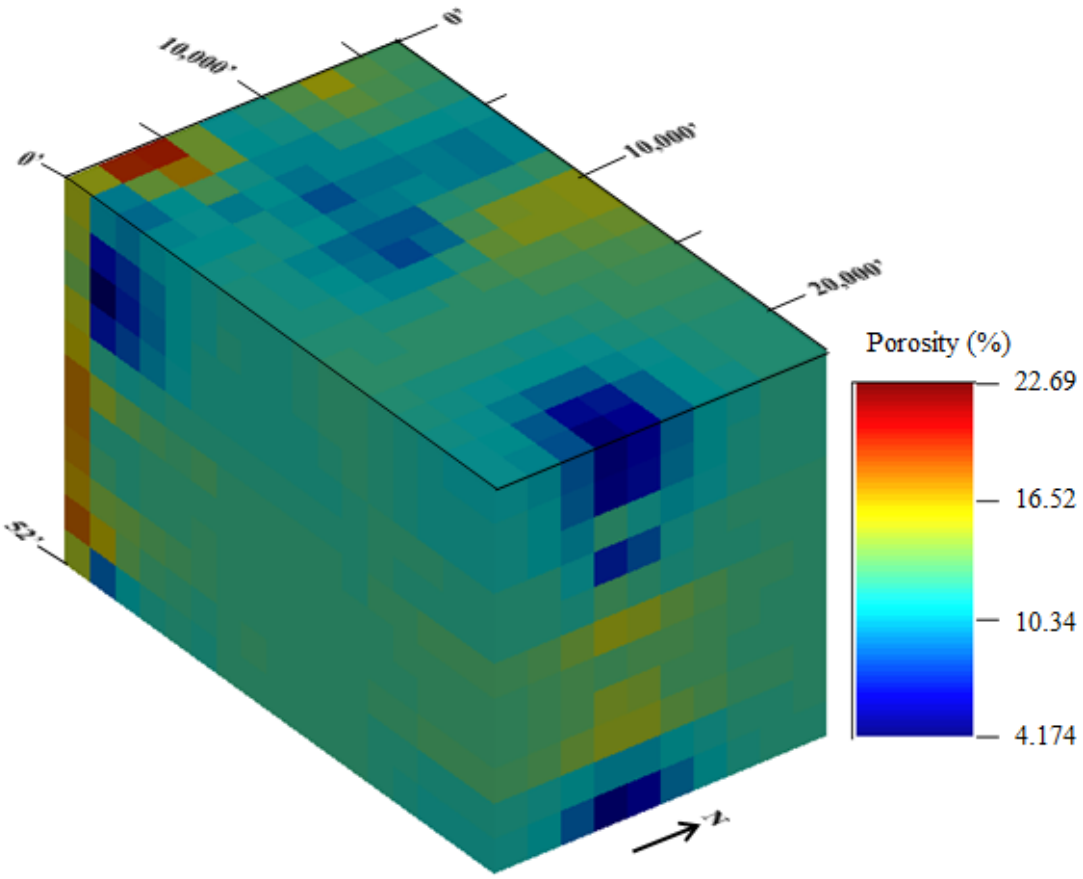

Figure 4.27, Upscaling of SK Panoma Gas Field to 5x5x5 cell size

The search ellipsoids retained the same specifications as used for the earlier simulations methods: ranges set at 25 feet, azimuth, dip and rake fixed to zero, and 12 for the conditioning data. Once finished, the integrated data was downscaled back to the 1x1x1 cell size (Figures 4.28 and 4.29), using the model variogram described earlier.

The results from originally upscaling to the field extent in the 1x1x1 between using the SK (Figure 4.24), and SGS (Figure 4.25) then downscaling display certain variations from each other. The SGS interpolation (Figure 4.28) contained numerous lower porosity

locations while the SK (Figure 4.29) conversely showed increased higher porosity distribution. Additionally, the result from running the SGS without adding the CT data shows higher porosity in a greater distribution (Figure 4.30).

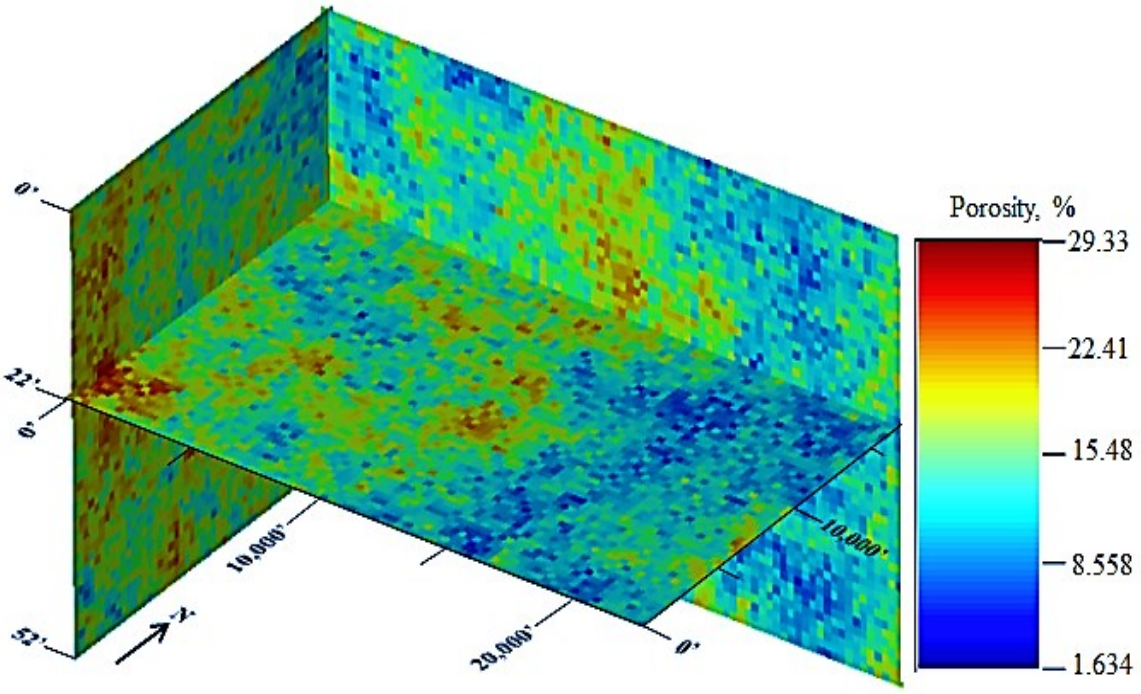

Figure 4.28, Downscaling of SGS Panoma Gas Field to 1x1x1 cell size after SGcS

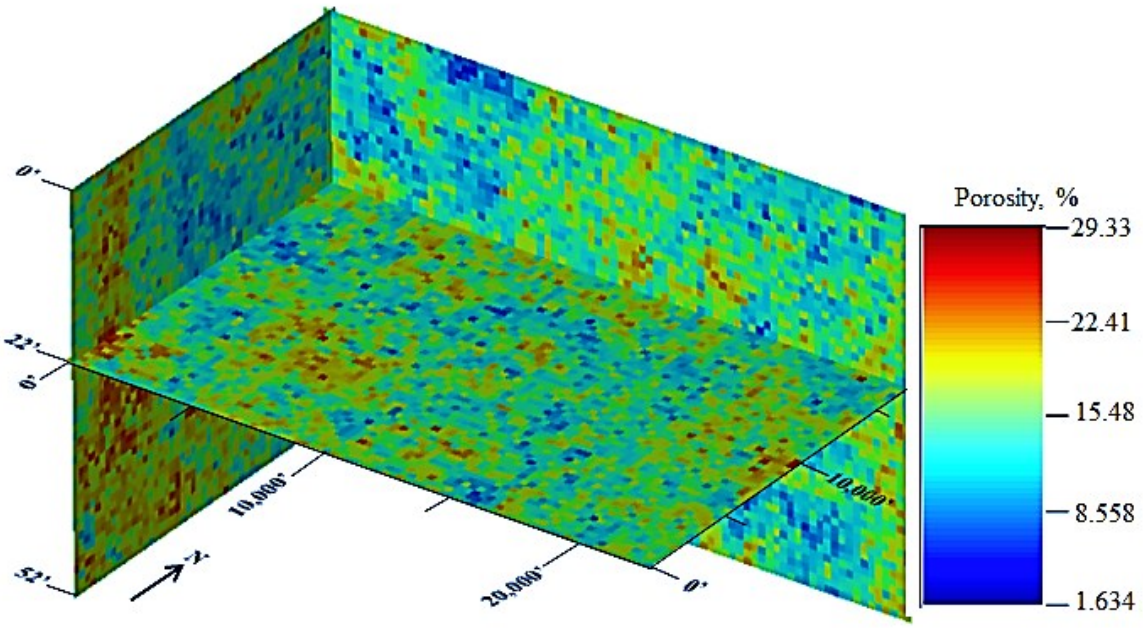

Figure 4.29, Downscaling of SK Panoma Gas Field to 1x1x1 cell size after SGcS

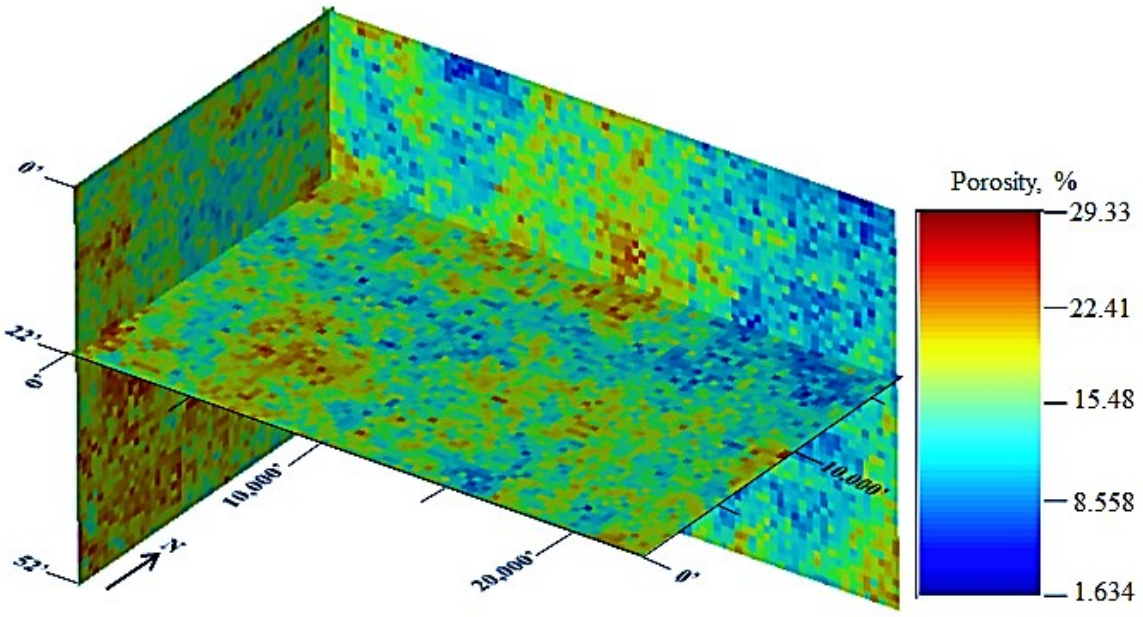

Figure 4.30, SGS results for Panoma Gas Field to 1x1x1 cell size
with no co-simulation

CHAPTER 5

DISCUSSION OF RESULTS

5.1 Misfit and Likelihood

The use of solely the misfit or likelihood algorithm to determine the depth from which the CT data originated yielded insufficient results. The Jinju well exhibited a cohesive response to likelihood, which was not prominent although it was at the correct depth. The Panoma Gas Field wells likely displayed a similar response; however, the graphs are too chaotic to elucidate the depth. Additionally, when the likelihood and misfit transformed parameters were compared based on whether the CT data had been upscaled or not upscaled, the best results were seen in the upscaled data. Entropy alone would not identify the CT depth but is a useful step when determining the amount of information contained in the parameters and thus which parameters should be included in the MIMC method.

After the MIMC method transformed the results from both misfit and likelihood functions, the misfit-derived results for each well yielded comparable findings to the likelihood results. However, the likelihood results required an adjustment, based on the value of the parameter which added a slower development, whilst the misfit results worked well on their own. The correct depth of the CT plug data appeared for every well following the use of the MIMC method.

5.2 MIMC Discussion

The histograms for the Panoma Gas Field (in the Appendix) and the Jinju (Figures 4.3 and 4.4) well-log and CT porosity data have different shapes of distribution, shifting from normal, to bi-modal, to uniform and to skewed. The Jinju well-log and CT data share the same distribution shape, both being positive or slightly skewed to the right. The most common distribution in the Panoma Gas Field well-log data was negatively skewed or a skewed-left distribution suggesting the data has a natural upper bound.

The Panoma Gas Field CT data were all uniform in their distribution shape, which might be a result of the random number generation. The well-log data distributions are all representative of natural varying data and suggest that the data does not need to be Gaussian or normalized to work in the MIMC method. Interesting to note, the individual well-log variograms did not have a nugget effect, but when the data was combined together to represent the field, the variogram then had a nugget effect.

The variograms for the Panoma Gas Field well-log data (Figure 4.18 and Appendix) were all very similar to each other, in terms of range, and mostly found to be Gaussian. The sills tended to vary the most with values ranging from ten to forty. One interesting aspect in several of the variograms was the falling tendency, where the data falls back towards zero after reaching the sill and range point. It is possible this is just one curve of the data representative of cyclical behavior but without a larger dataset, this is merely speculation.

The variograms for the Panoma Gas Field CT data (Figure 4.19 and Appendix) are even more similar than the well data. All the variograms have an exponential shape and 0.2 feet for the range. The sill changes minimally, ranging from 0.085 to 5.5 with 0.3 the most

common value. In contrast to the well-log variograms, the CT variograms did not have erratically behaving data.

The likelihood function had the capability to identify the depth for the CT data in the well-log data; however, a graph examining solely these results is not always clear enough to locate the depth. This is also seen when graphing the misfit function results. Determining the entropy of the data was not always a necessary step in the correlation.

The MIMC method demonstrated remarkable ability to identify and correlate the depths of CT data to well-log data. The MIMC method combined with the misfit function performed to a better capacity than using the depth-correlation constant with the likelihood function. The MIMC method joined with misfit instead of adding the likelihood step shows a clearer and more readable graph, meaning depth correlation occurs quicker and more easily.

The mean parameter originally was included in the MIMC process but disregarded as after transforming the value it repeatedly had a value that varied significantly from the other statistical parameters, which then skewed the final results. This often occurred when the parameters were non-scaled or scaled incorrectly (Table 5.1). However, when the mean had a reasonable value, the inclusion of the parameter to the correlation method will either show no difference in the result or helps tighten the correlation enough to increase the value of the correlation constant and reveal the depth.

Table 5.1, Showing how the mean skews the final results

	misfit					likelihood				
depth	mean	var	skew	kurt	std dev	mean	var	skew	kurt	std dev
1797	378.85	0.77	1.40	1.20	0.62	0.0E+00	0.55	0.14	0.24	0.68
1798	390.63	0.45	1.06	1.95	0.34	0.0E+00	0.82	0.33	0.02	0.89
1799	523.09	0.40	0.12	4.22	0.30	0.0E+00	0.85	0.99	1.86E-08	0.92
1800	610.34	1.32	0.31	4.78	1.26	0.0E+00	0.17	0.91	1.20E-10	0.20
1801	634.87	1.49	1.52	15.08	1.57	0.0E+00	0.11	0.10	1.92E-99	0.09
1802	493.75	3.74	0.28	3.60	1.85	0.0E+00	0.00	0.93	2.40E-06	0.03

As noted in generating basic statistics (Section 3.2) the likelihood function may derive a very small number, often smaller than 10^{-6}. These smaller numbers, however, never showed in the parameters at the correct depth which generally were greater than zero but have little variation or deviance from each other. Due to these conditions, the decision was made to set the average deviation values to one or alternatively the correlation constant to zero to reduce the influence of the extremely small values. This modification, again, is not necessary when using solely the misfit function, and as such MIMC joined with misfit is recommended.

Well 20338, located in the Panoma Gas Field, displayed results showing irregular repeating sequences due to the skewness and kurtosis values not varying through the entire depth (Appendix A1.1). Due to this, the data transformation with MIMC did not reach as clear of a result as the other wells. However, after factoring in the depth correlation uncertainty, as determined in the Kansas Geological Survey well database to be 2.5 feet, the peak at the depth of 3022 feet still has the best depth correlation.

Error variance equations compared the highly resolved CT porosity values to the well-log porosity values. The largest variances between the datasets occur in wells that had

negative values in one of the parameters, such as skewness or kurtosis, which described the porosity distribution. These error variance values are all larger than one. However, the remaining error values are smaller than one, often by an order of magnitude, reflecting the relationship between the values (Table 5.4). The correlation coefficient was also calculated for each set of parameters, analyzing well-log to CT values at the MIMC determined depth (Table 5.2). Tables 5.3 and 5.4 show the statistical parameters for well-log data and CT data and corresponding error values, respectively.

Table 5.2, Correlation coefficients for the statistical parameters between well-log and CT at the best fit depth

Parameter	mean	var	skew	kurt	std dev
Correlation	0.9975	0.9920	0.0605	-0.2414	0.9898

Table 5.3, Comparing statistical parameters for well-log and CT for each well

	Well-Log					CT				
well	mean	var	skew	kurt	std dev	mean	var	skew	kurt	std dev
20338	9.65	0.00	0.00	-1.20	0.04	10.71	0.10	1.12	2.82	0.29
20363	38.68	0.03	-0.74	-0.83	0.17	38.66	0.18	0.16	-0.92	0.43
20369	23.05	0.02	1.06	-0.31	0.15	23.26	0.06	0.11	-1.22	0.24
20370	24.15	0.13	-0.59	-0.98	0.36	24.38	0.26	0.01	-1.12	0.51
20371	21.87	0.08	-1.13	0.03	0.28	22.20	0.83	-0.11	-1.16	0.91
20398	20.32	0.35	-0.53	-1.02	0.59	20.45	0.77	-0.02	-1.12	0.88
20414	21.50	0.76	1.05	0.18	0.87	22.16	0.82	-0.18	-1.26	0.91
20416	19.90	3.15	0.22	-1.17	1.78	19.36	4.77	0.07	-1.19	2.18
20592	26.04	13.27	-0.37	-1.11	3.64	24.56	13.99	0.22	-1.28	3.74
21031	27.32	0.73	-1.11	0.13	0.86	26.91	0.78	-0.13	-1.09	0.88
21040	19.65	0.05	1.13	0.04	0.23	19.77	0.21	-0.02	-1.17	0.46
Jinju	5.02	11.31	0.59	-1.81	3.36	5.57	14.42	0.25	-1.29	3.80

Table 5.4, Error variances for each well at the correlated depth

	Error Variances				
Well	mean	var	skew	kurt	std dev
20338	0.0992	0.9885	1.0000	1.4262	0.8716
20363	-0.0004	0.8486	5.6210	0.0918	0.6109
20369	0.0090	0.6050	-8.6146	0.7456	0.3715
20370	0.0092	0.5016	41.7434	0.1310	0.2941
20371	0.0151	0.9032	-8.8469	1.0278	0.6888
20398	0.0060	0.5475	-27.3846	0.0928	0.3273
20414	0.0298	0.0743	6.8016	1.1447	0.0379
20416	-0.0280	0.3388	-2.2664	0.0154	0.1869
20592	-0.0601	0.0511	2.7148	0.1274	0.0259
21031	-0.0150	0.0537	-7.2329	1.1169	0.0272
21040	0.0061	0.7593	48.4268	1.0346	0.5093
Jinju	0.0975	0.2156	-1.3407	-0.3998	0.1143

The statistical parameters were compared further in order to examine the correlation between each parameter at the well-log and CT scale. The mean, variance and standard

deviation all show high correlation values, while skewness and kurtosis values are low. The low skewness and kurtosis correlation is likely a response to both values fluctuating between positive and negative values, while the other parameters are only positive. These values can be seen both in Table 5.2 and in the cross plots in Figure 5.1 for porosity and Figure 5.2 for skewness.

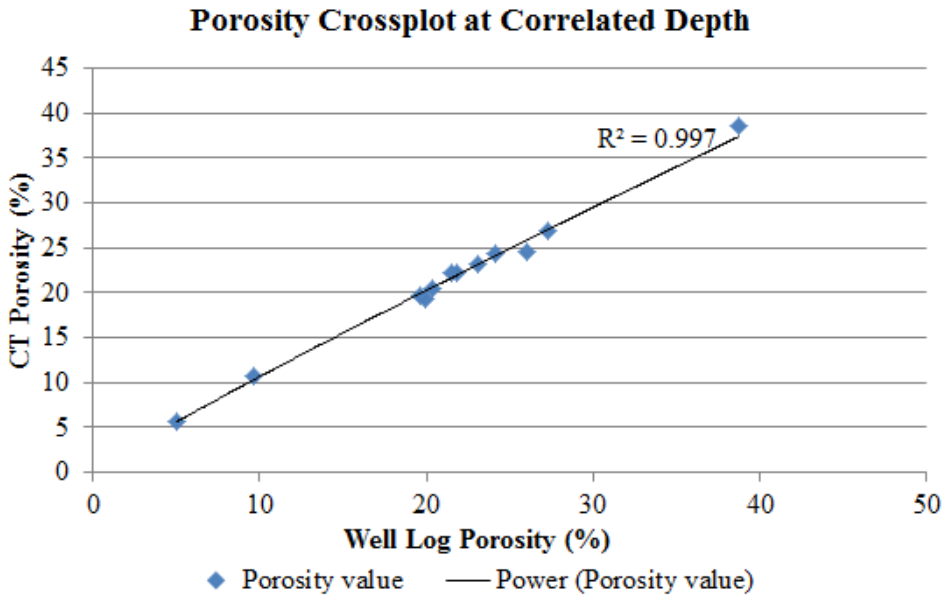

Figure 5.1, Cross plot showing correlation of porosity values

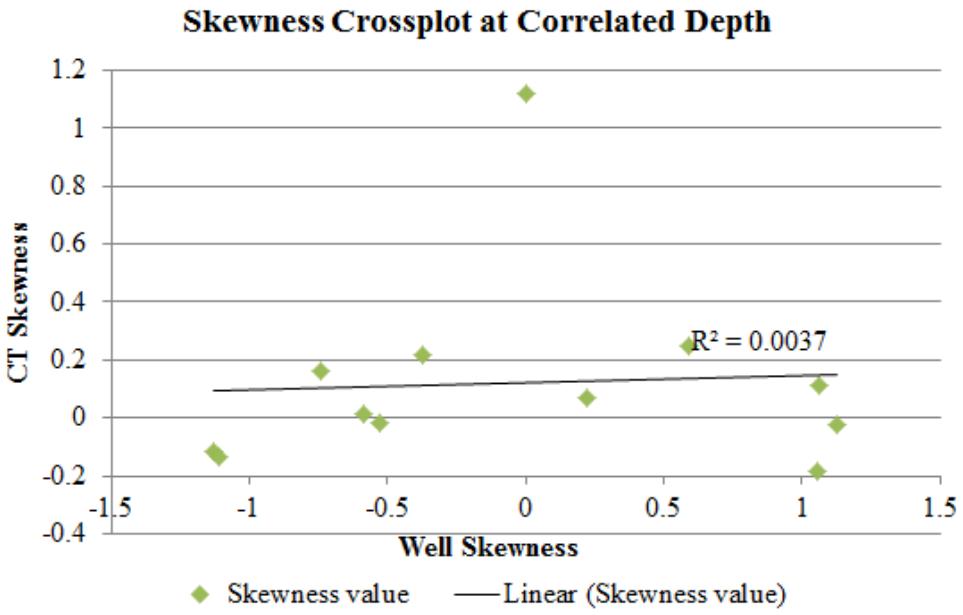

Figure 5.2, Cross plot showing correlation of skewness values

For circumstances when the depth from which the CT core is sampled is unknown or has a high uncertainty, a modified correlation method can be used to find a best-fit depth to the well-log data. However, this requires a more rigorous process using unscaled CT data, where likelihood and the MIMC method are run twice. The first time the process is done on a larger section, the second time the process is only run using the depths of interest. To begin, the depth interval for running the statistics should be narrowed down to within a five to ten foot window on either side from where the sample plug is believed to originate. Table 5.5 illustrates how the variances, used in misfit to compare the parameters, are calculated at every depth interval instead of just a single known depth.

Table 5.5
The progression from primary statistics to Misfit results with unknown correlation depth

	primary derived statistics					constants from CT data				
depth (ft)	mean	var	skew	kurt	std dev	mean	var	skew	kurt	std dev
1817.0	25.7	0.3	-0.4	-1.1	0.6	24.5	0.1	-0.2	-1.1	0.3
1818.0	26.7	0.0	-1.1	-0.3	0.1	24.5	0.1	-0.2	-1.1	0.3
1819.0	25.4	0.4	1.0	-0.5	0.6	24.5	0.1	-0.2	-1.1	0.3
1820.0	24.8	0.0	0.5	-1.1	0.0	24.5	0.1	-0.2	-1.1	0.3
1821.0	24.7	0.0	-0.2	-1.2	0.0	24.5	0.1	-0.2	-1.1	0.3
1822.0	24.5	0.0	-0.7	-0.8	0.1	24.5	0.1	-0.2	-1.1	0.3
1823.0	24.0	0.0	-0.1	-1.0	0.2	24.5	0.1	-0.2	-1.1	0.3
1824.0	24.4	0.0	-0.6	-0.9	0.1	24.5	0.1	-0.2	-1.1	0.3
1825.0	24.7	0.0	-0.5	-1.1	0.0	24.5	0.1	-0.2	-1.1	0.3
1826.0	24.0	0.4	-0.6	-1.0	0.6	24.5	0.1	-0.2	-1.1	0.3
1827.0	21.5	0.5	0.7	-0.9	0.7	24.5	0.1	-0.2	-1.1	0.3

	Variances between derived & CT					Misfit				
depth (ft)	mean	var	skew	kurt	std dev	mean	var	skew	kurt	std dev
1817.0	0.4	0.0	0.0	0.0	0.0	2.0	2.0	2.0	2.0	2.0
1818.0	1.1	0.0	0.2	0.2	0.0	2.0	2.0	2.0	2.0	2.0
1819.0	0.2	0.0	0.4	0.1	0.0	2.0	2.0	2.0	2.0	2.0
1820.0	0.0	0.0	0.1	0.0	0.0	2.0	2.0	2.0	2.0	2.0
1821.0	0.0	0.0	0.0	0.0	0.0	2.0	2.0	2.0	2.0	2.0
1822.0	0.0	0.0	0.1	0.0	0.0	2.0	2.0	2.0	2.0	2.0
1823.0	0.1	0.0	0.0	0.0	0.0	2.0	2.0	2.0	2.0	2.0
1824.0	0.0	0.0	0.0	0.0	0.0	2.0	2.0	2.0	2.0	2.0
1825.0	0.0	0.0	0.0	0.0	0.0	2.0	2.0	2.0	2.0	2.0
1826.0	0.1	0.0	0.0	0.0	0.0	2.0	2.0	2.0	2.0	2.0
1827.0	2.3	0.0	0.2	0.0	0.0	2.0	2.0	2.0	2.0	2.0

The CT plug data is not upscaled throughout this process. Once the misfit function has been applied, the results are transformed with the average group deviation (Equation 11) and then followed by taking the log of results ($\log_{10}(x)$), where x is the result. Misfit is combined with the correlation in this process as the subsequent values are slightly greater

which aids in ascertaining the depths for testing; however, the likelihood function also can be utilized.

The largest values specify the depths that are tested. Table 5.6 and Figure 5.3 show the MIMC values, of which the best depths to test for are at 1821 and 1822 feet, within the 2.5 foot uncertainty. The graph elucidates the data which facilitates choosing the depths for the best-fit determination.

Table 5.6

Continuing the progression from Misfit to best-fit with unknown CT depth

unknown	Misfit results					MIMC	
depth (ft)	mean	var	skew	kurt	std dev	avg dev	log
1817.0	2.0	2.0	2.0	2.0	2.0	6.44E-03	-2.191
1818.0	2.0	2.0	2.0	2.0	2.0	2.44E-05	-4.613
1819.0	2.0	2.0	2.0	2.0	2.0	2.32E-05	-4.635
1820.0	2.0	2.0	2.0	2.0	2.0	1.50E-04	-3.823
1821.0	2.0	2.0	2.0	2.0	2.0	1.34E-03	-2.874
1822.0	2.0	2.0	2.0	2.0	2.0	2.13E-04	-3.671
1823.0	2.0	2.0	2.0	2.0	2.0	1.29E-04	-3.890
1824.0	2.0	2.0	2.0	2.0	2.0	1.40E-04	-3.854
1825.0	2.0	2.0	2.0	2.0	2.0	1.63E-04	-3.787
1826.0	2.0	2.0	2.0	2.0	2.0	8.55E-05	-4.068
1827.0	2.0	2.0	2.0	2.0	2.0	3.36E-05	-4.474

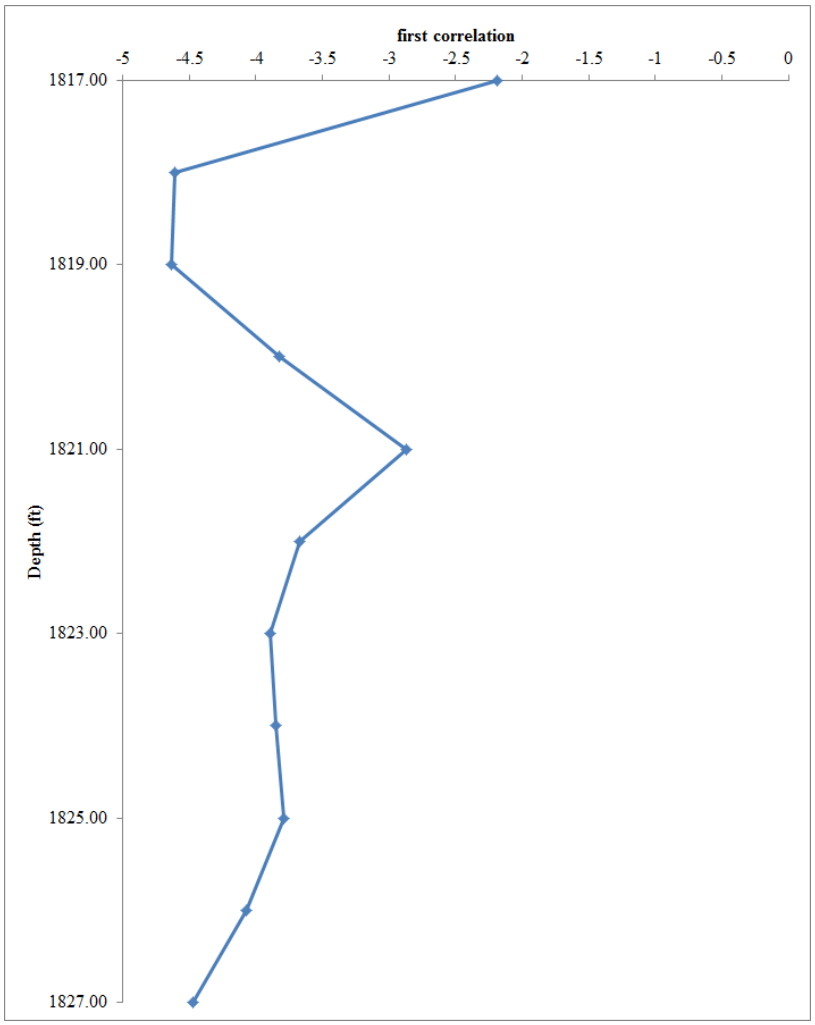

Figure 5.3, The greatest values within the uncertainty range can be seen with the graph

Once the depths with the highest peak have been identified, usually within the uncertainty recorded from the coring, the misfit function and MIMC are executed. The variances are set to the selected depths (Table 5.7) as when running the MIMC method as detailed in the generating basic statistics (Section 3.2). The MIMC columns (in Table 5.7) show the values following the misfit transformation with the MIMC method (Equation 13). Table 5.8 demonstrates the greatest value, 287.6, seen between the two selected depths, 1821

and 1822 feet, is in the column for the correct depth, depth 1822. These correlated depths then can help guide the reservoir simulation. If plotting the results, the peak with the greatest value from the different depths will be the best fit for the correct depth.

Table 5.7
Setting the variance to the selected depths when the best-fit depth is unknown

	primary derived statistics					CT values and variance by depth				
Depth (ft)	mean	var	skew	kurt	std dev	mean	var	skew	kurt	std dev
1818.0	26.7	0.0	-1.1	-0.3	0.1	24.5	0.1	-0.2	-1.1	0.3
1819.0	25.4	0.4	1.0	-0.5	0.6					
1820.0	24.8	0.0	0.5	-1.1	0.0					
1821.0	24.7	0.0	-0.2	-1.2	0.0	1821.0 variances				
1822.0	24.5	0.0	-0.7	-0.8	0.1		0.0	-0.2	-1.2	0.0
1823.0	24.0	0.0	-0.1	-1.0	0.2	var	0.0	0.0	0.0	0.0
1824.0	24.4	0.0	-0.6	-0.9	0.1	1822.0 variances				
1825.0	24.7	0.0	-0.5	-1.1	0.0		0.0	-0.7	-0.8	0.1
1826.0	24.0	0.4	-0.6	-1.0	0.6	var	0.0	0.1	0.0	0.0

Table 5.8
MIMC results of selected depths to determine the best-fit depth when it is unknown

	1821.0 misfit				1821.0		1822.0 misfit				1822.0	
Depth (ft)	var	skew	kurt	std dev	MIMC		var	skew	kurt	std dev	MIMC	
1818.0	1.4	82.7	21.4	1.3	28.0	0.0	1.6	2.3	4.1	1.8	0.8	1.2
1819.0	6.1	120.7	16.1	2.1	42.2	0.0	7.1	3.4	3.1	2.9	1.5	0.7
1820.0	1.4	69.0	1.1	1.3	25.4	0.0	1.6	1.9	0.2	1.9	0.6	1.7
1821.0	1.4	1.4	1.4	1.4	0.0	118.4	1.6	0.0	0.3	2.0	0.8	1.2
1822.0	1.2	50.7	7.4	1.0	17.8	0.1	1.4	1.4	1.4	1.4	0.0	287.6
1823.0	0.7	17.6	1.6	0.4	6.3	0.2	0.8	0.5	0.3	0.6	0.1	7.2
1824.0	1.2	39.0	4.4	0.9	13.8	0.1	1.3	1.1	0.8	1.3	0.2	6.0
1825.0	1.4	21.7	1.0	1.3	7.7	0.1	1.6	0.6	0.2	1.9	0.7	1.5
1826.0	5.7	33.0	3.0	2.0	11.0	0.1	6.6	0.9	0.6	2.8	2.0	0.5

5.3 SGS Scaling Discussion

The SGS scaling results produced several different models: original SK (Figure 4.29), original SGS (Figure 4.28), and the interpolation without the SGcS (Figure 4.30). Most interesting was how the SK downscaled model did not retain the porosity distribution as seen in the upscaled SK model. Even after varying the range distances and number of conditioning data, the smooth distribution was not retained. The simulation model that had a porosity distribution most similar to the SK original interpolation (Figure 4.24) was the SGS after the SGcS (Figure 4.28). Multiple realizations produced by upscaling and downscaling by SGS produced results that varied negligibly, indicating an increase in confidence in the model.

Another interesting feature arising from the different simulation techniques, SGS, SK and SGcS, was the increase in the porosity in the SK realization (Figure 4.29) and the interpolation without the SGcS (Figure 4.30). It is often thought that SK has the greatest capacity for retaining the spatial structure of the data and SGS tends to lose the information. The results seen in this study insinuate that this may not always be the case. However, the SGS did use simple kriging for its interpolation method, which likely helped in the modeling (Figure 4.28).

The SGS interpolation, unlike the SK, produced negative values, undoubtedly as a result of creating a normal distribution. In order to evaluate the performance of the porosity values under better conditions, the values were transformed into a lognormal distribution (Figure 5.4). These new porosity values were then run through the SGS upscaling then the SGcS and then downscaled back to the higher resolution model (Figure 5.5).

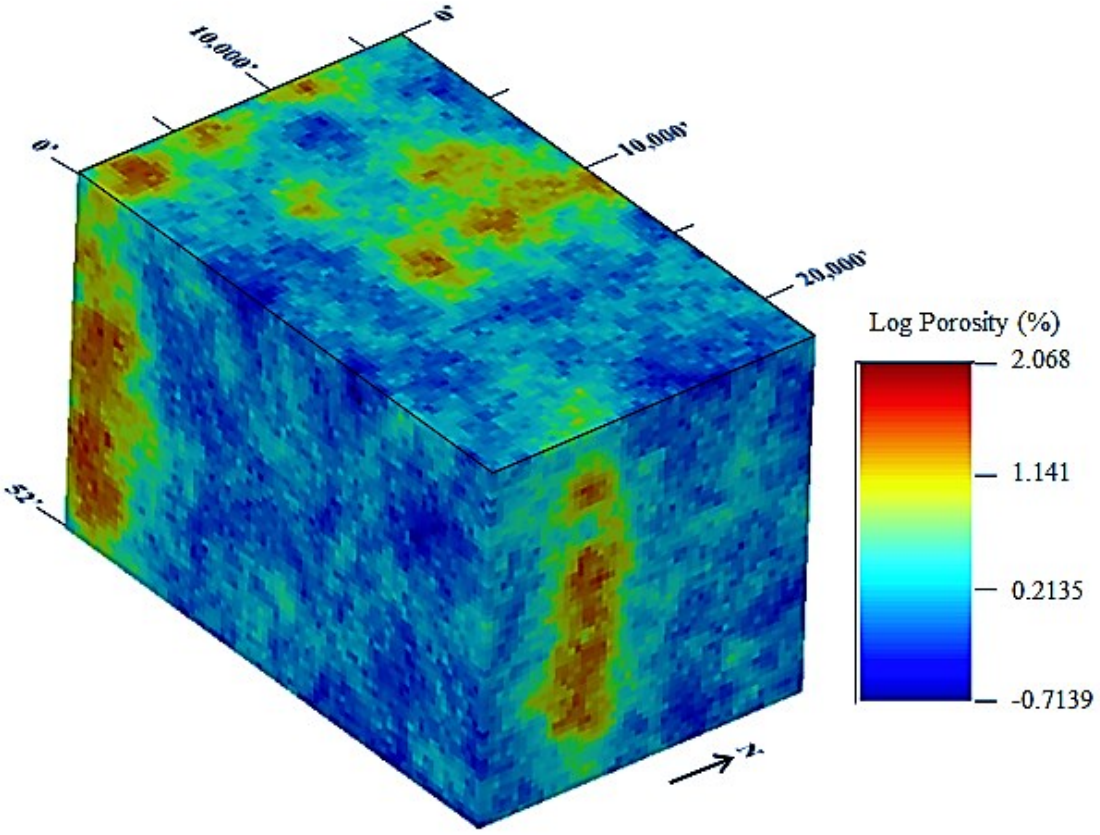

Figure 5.4, SGS simulation on log porosity values to 1x1x1.

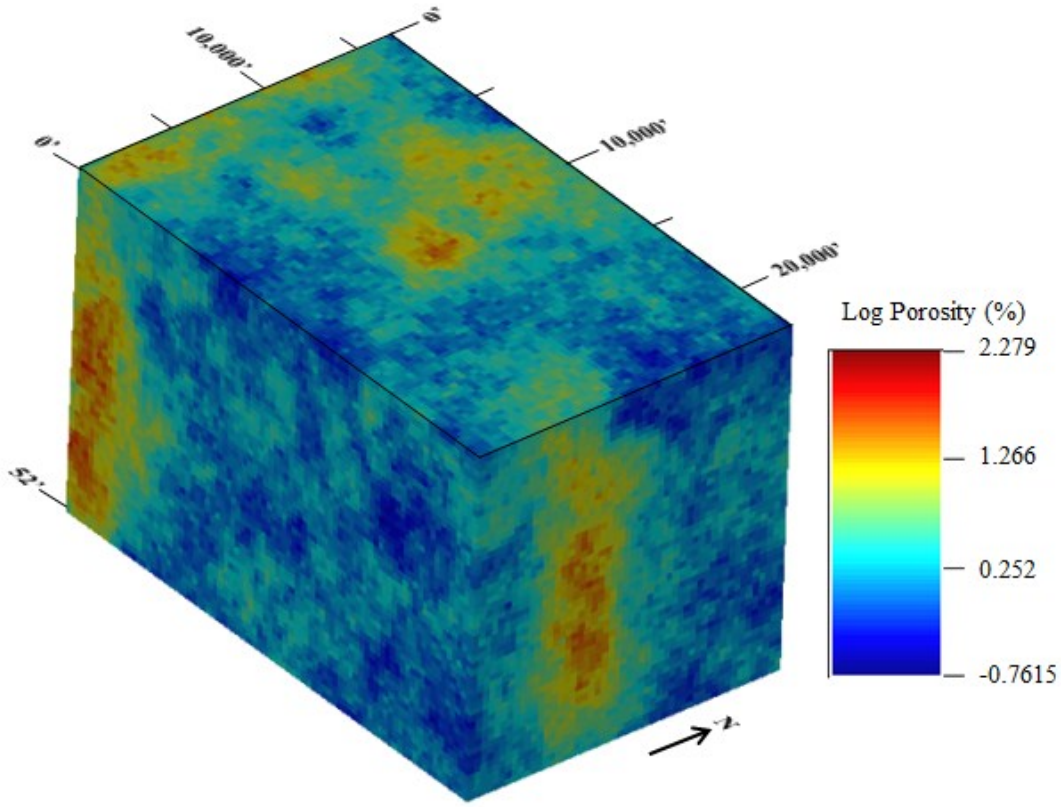

Figure 5.5, After SGcS and downscaled back to 1x1x1 size.

The log transformed porosity simulation reveals a tighter distribution of higher porosity areas concentrating around the wells before and after the co-simulation than the other interpolations. Additionally, it appears the CT data constrains the whole modeled reservoir to slightly lower porosity and a greater part of the reservoir to lower porosity values except for the areas immediately around the wells. This porosity structure or distribution retention is closest to the normal porosity simulation from SK as well. However, for projecting new locations to drill or for synthesizing fluid flow, this structural clustering resulting from the log transformed porosity becomes insufficient.

5.4 Further Work

The co-simulation renders a greater refinement in determining or refining the porosity structure than the interpolation of exclusively the well log data. This difference would likely intensify when multiple depths of CT or core-plug data is available per well. The SGS method also yields improved results than simple kriging alone, even though the results are not as smooth when interpolating the data to field extent. It appears that SGS has the capability to retain a more vibrant and accurate interpretation of the porosity distribution. In order to realize or determine a superior reservoir model, these implications should be fully considered.

An area of interest concerns the variogram models (see Appendix), in which instead of the exponential model chosen for some of the well-log variograms a dampened-hole effect variogram model would have been a more appropriate choice. This is in part due to the hole effect or cyclical behavior seen in the experimental variogram. It is unknown if this change in variogram model would have a significant effect on the scaling equation and subsequent correlation.

The data integration model produced from this study would benefit from further exploration in achieving easier methods for locating the unknown correlation depth. As it stands now, the depth can be determined but the process is intensive requiring multiple calculations in order to determine then compare each suspect depth. Several methods involving comparing the likelihood derived correlation to the misfit derived correlation or MIMC, by adjusting the parameters in the algorithms, have been attempted with limited success. Perhaps finding the correlated depth shall remain a complex process or ascertaining

the hidden component to solve this issue demands more time than this project allowed, as that was not the focus of this research.

While extensive research into the usefulness of SGS to model reservoir characteristics has occurred, further research into improving porosity estimations from correlated depth would benefit reservoir modeling. This research only investigated including one depth for CT or plug examination yet incorporating several depths for constraining would likely enhance the reservoir characterization.

Much investigation has been done incorporating seismic data in order to delineate larger scale structure into the reservoir model. This study did not have the opportunity to integrate this much larger volume of measurement into the reservoir characterization. It is unknown if the addition of seismic data would have affected the simulation results to a great degree or would instead have minimal impact.

CHAPTER 6

CONCLUSION

This study investigated relating basic geostatistical methods to develop a model for integrating data of varying scales. Well-log and CT data from twelve different wells in geologic reservoirs formed under varying environmental conditions provided the data. The geostatistical scaling model incorporated several geostatistical stages in order to achieve correlation depths and integrate the porosity data from well-log and CT data.

Basic histograms and variogram models defined the scaling parameter that brought the CT data to the same resolution as the well-log data plus to integrate the data with SGcS. The histograms for the Panoma Gas Field and Jinju well-log and CT porosity data had multiple distribution shapes, shifting from normal, to bi-modal, to uniform and to skewed. Variance-based statistics were computed within specific intervals then a best-fit for depth correlation was differentiated.

Misfit and likelihood algorithms transformed the data, but cannot be used alone for depth correlation as they yielded insufficient results to determine the depth from which the CT data originated. The likelihood function had the capability to identify the depth for the CT data in the well log data; however a graph examining solely these results is not always clear enough to locate the depth. The likelihood and misfit transformed parameters were compared based on whether the CT data had been upscaled or not upscaled, with the best results seen in the upscaled data. Entropy was implemented to identify which statistical

parameters should be utilized in the correlation algorithm but entropy could not identify the CT depth alone.

The development and application of the MIMC method delineated the depth to easily identify and correlate the well-log porosity and porosity from core-plugs or CT scans. The MIMC method proved its ability to correlate the depths of the CT data for every well, including within the determined uncertainty for the well with irregular data and resulting statistics. These depths then were employed during reservoir model building with SGcS to help realize a more accurate porosity distribution.

The SGS upscaling and downscaling produced several different models for the porosity distribution. Upscaling methods utilizing SGS and SK were compared to determine the retention of porosity structure and differences were noted between the procedures. The simulation model that had a porosity distribution most similar to the SK original interpolation was the SGS following the SGcS. Multiple realizations produced by the SGS produced results that varied insignificantly suggesting minimal uncertainty in the simulation. Another observation of the different simulation techniques, SGS, SK and SGcS, was an increase in the porosity values in the SK realization and the interpolation without the SGcS

Error variance equations compared the CT higher-resolution values to the well-log values with the largest variances between the datasets occurring in wells that had negative values in one of the statistical parameters of skewness or kurtosis. For circumstances when the depth, from which the CT core is sampled, is unknown or has a high uncertainty, a modified MIMC method can be used to find the appropriate depth. The porosity values were transformed into a lognormal distribution and run through the SGS upscaling then the SGcS and then downscaled back to the higher-resolution model. The CT data appeared to constrain

the reservoir to an overall lower porosity plus most of the reservoir to smaller porosity values except for the regions directly surrounding the wells.

This research showed the usefulness of geostatistics in examining several parameters in porosity data, while correlating the maximum-resolution data to the medium-resolution data, and then constraining said data to construct a high-resolution geostatistical model. This project examined and illustrated the efficacy of a geostatistical modeling approach to the integration of geophysical data from well-log and core experiments under different geologic settings of reservoir. This research culminated in the development of a multi-dimensional high-resolution modeling framework for the reconstruction of sequential rock formation of reservoirs using geostatistical techniques involving a misfit/likelihood method and sequential Gaussian simulation.

APPENDIX

Section Page

A1 Panoma Gas Field Results for Remaining Wells 76

A1.1 Well 20338 Likelihood & MIMC 76

A1.2 Well 20338 Well log & CT Variograms 77

A1.3 Well 20338 Well log & CT histograms 78

A1.4 Well 20363 Well log & CT Variograms 79

A1.5 Well 20363 Well log & CT histograms 80

A1.6 Well 20369 Likelihood & MIMC 81

A1.7 Well 20369 Well log & CT histograms 82

A1.8 Well 20370 Well log & CT Variograms 83

A1.9 Well 20370 Well log & CT histograms 84

A1.10 Well 20371 Likelihood & MIMC 85

A1.11 Well 20371 Well log & CT Variograms 86

A1.12 Well 20371 Well log & CT histograms 87

A1.13 Well 20398 Likelihood & MIMC 88

A1.14 Well 20398 Well log & CT Variograms 89

A1.15 Well 20398 Well log & CT histograms 90

A1.16 Well 20414 Likelihood & MIMC 91

A1.17 Well 20414 Well log & CT Variograms 92

A1.18 Well 20414 Well log & CT histograms 93

A1.19 Well 20416 Likelihood & MIMC 94
A1.20 Well 20416 Well log & CT Variograms 95
A1.21 Well 20416 Well log & CT histograms 96
A1.22 Well 20592 Likelihood & MIMC 97
A1.23 Well 20592 Well log & CT Variograms 98
A1.24 Well 20592 Well log & CT histograms 99
A1.25 Well 21031 Likelihood & MIMC 100
A1.26 Well 21031 Well log & CT Variograms 101
A1.27 Well 21031 Well log & CT histograms 102
A1.28 Well 21040 Likelihood & MIMC 103
A1.29 Well 21040 Well log & CT Variograms 104
A1.30 Well 21040 Well log & CT histograms 105

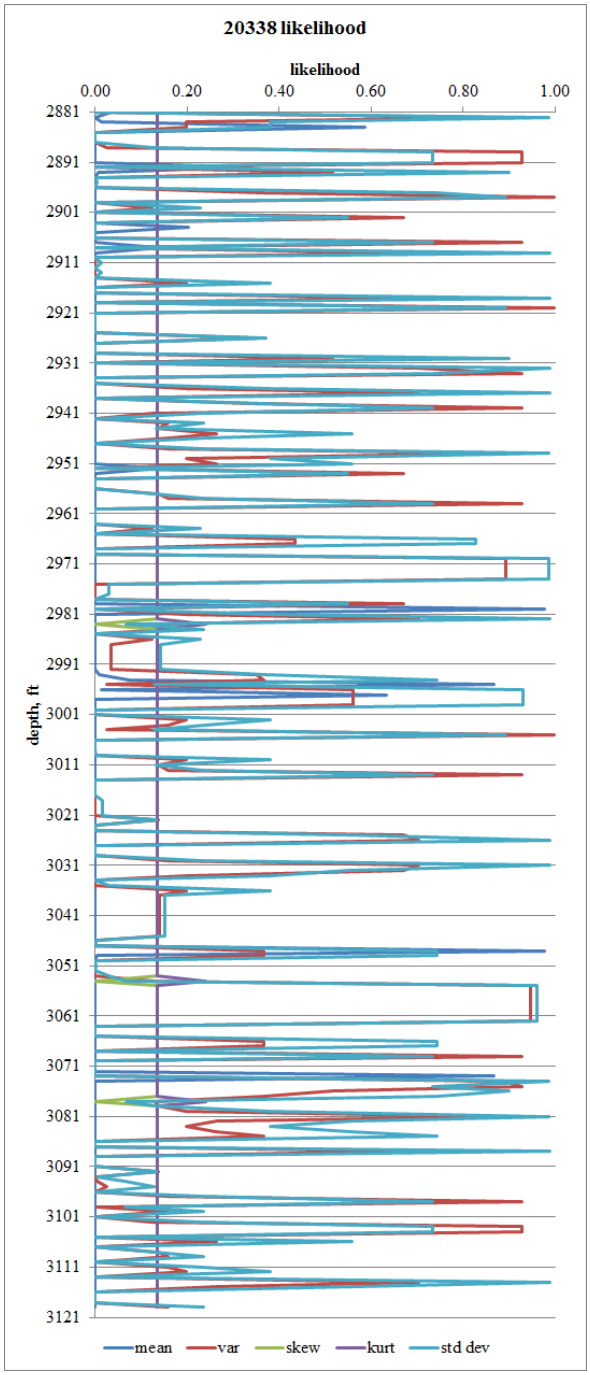

Likelihood for well 20338

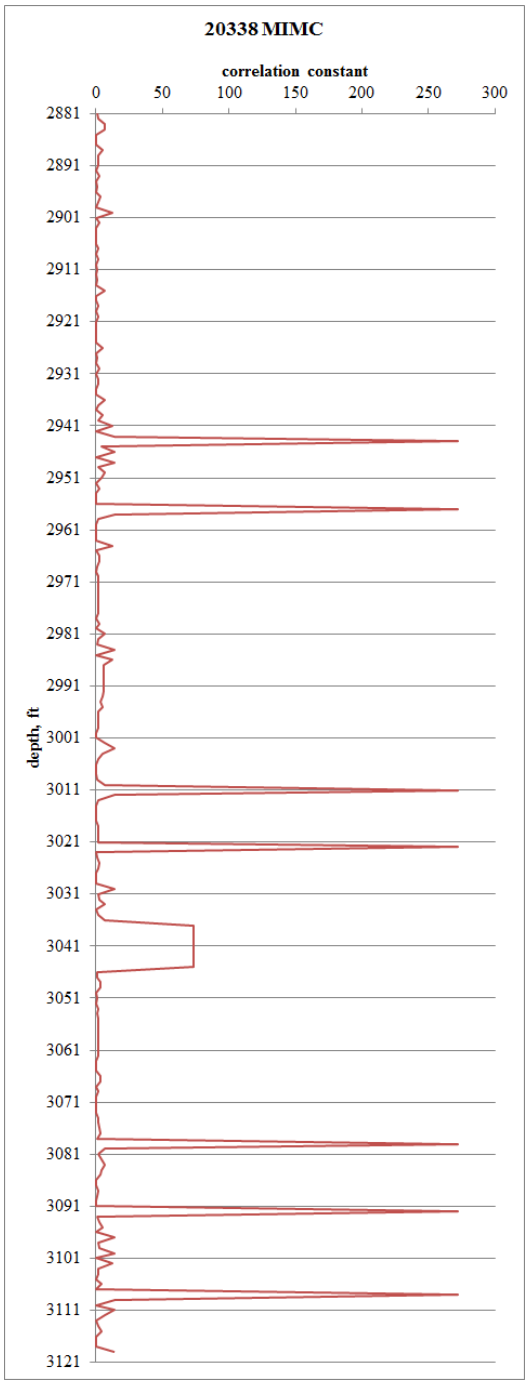

MIMC for well 20338

A1.1 Well 20338

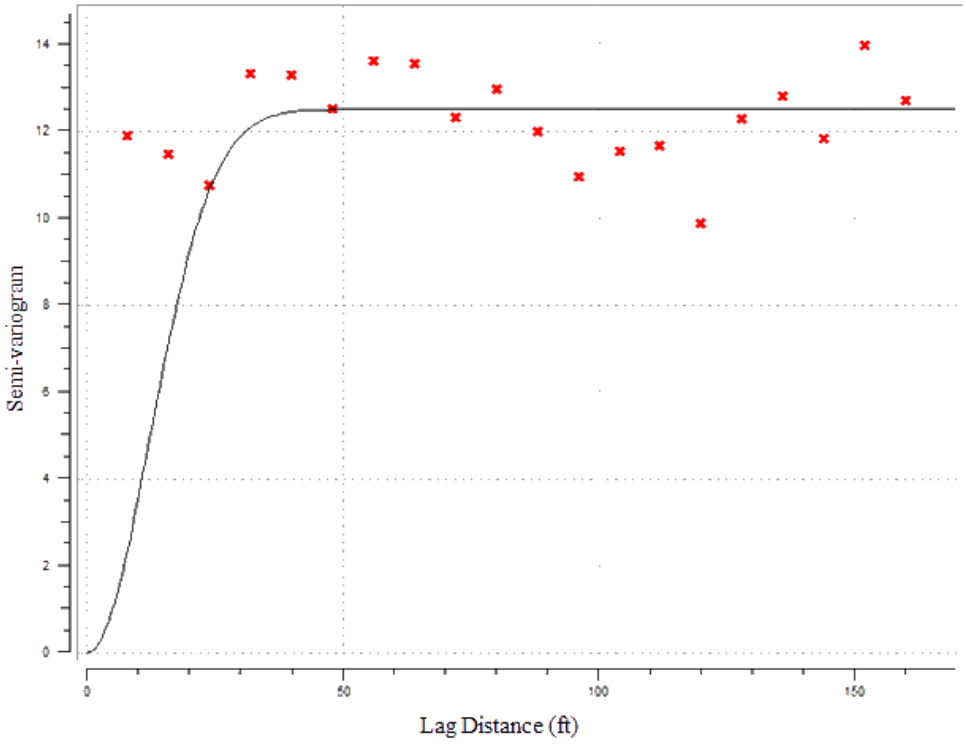

Well 20338 well log variogram

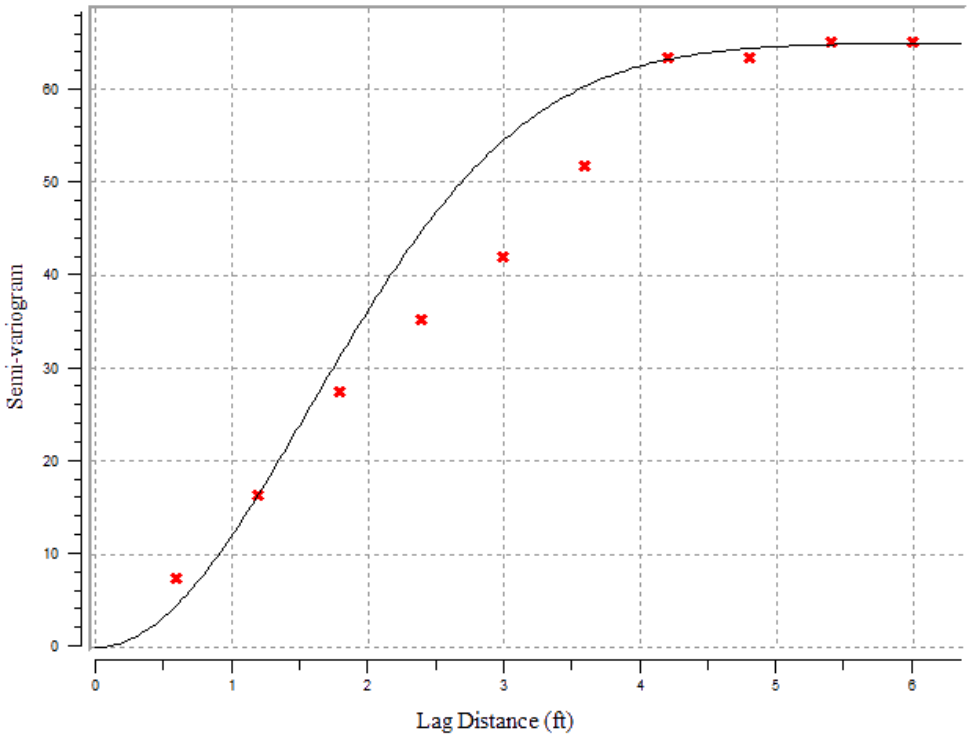

Well 20338 CT variogram

A1.2 Well 20338

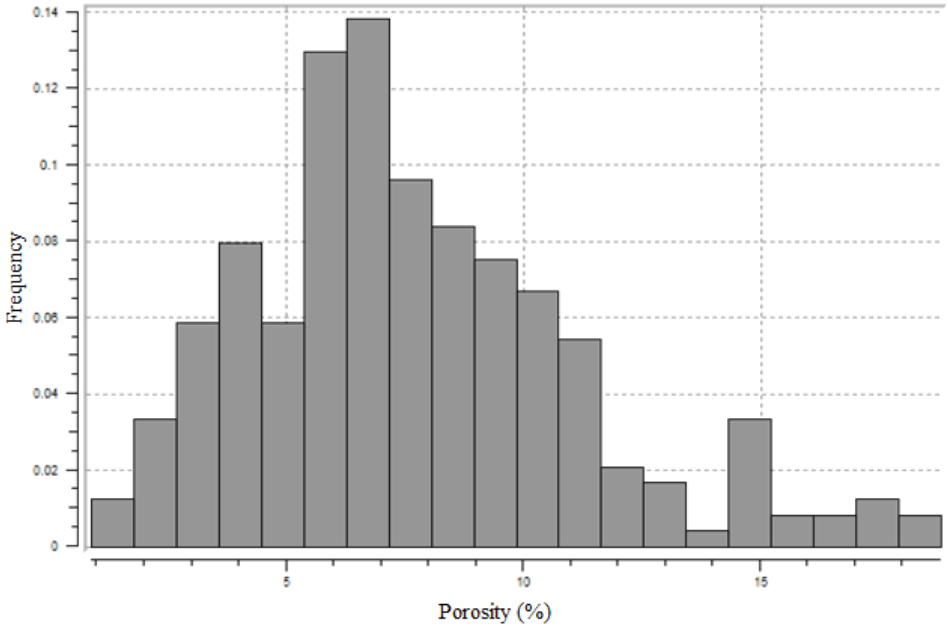

Well 20338 well log histogram

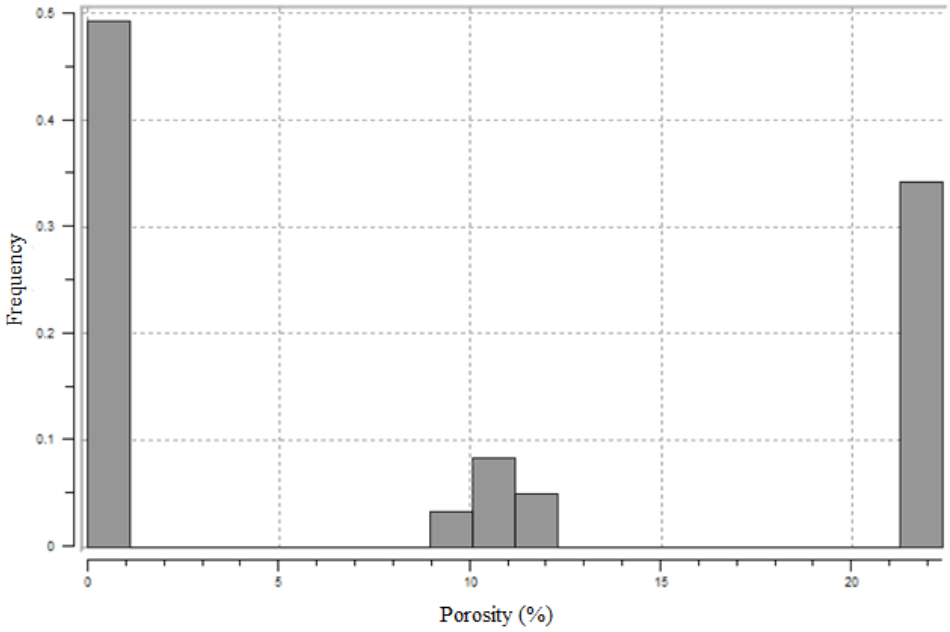

Well 20338 CT histogram

A1.3 Well 20338

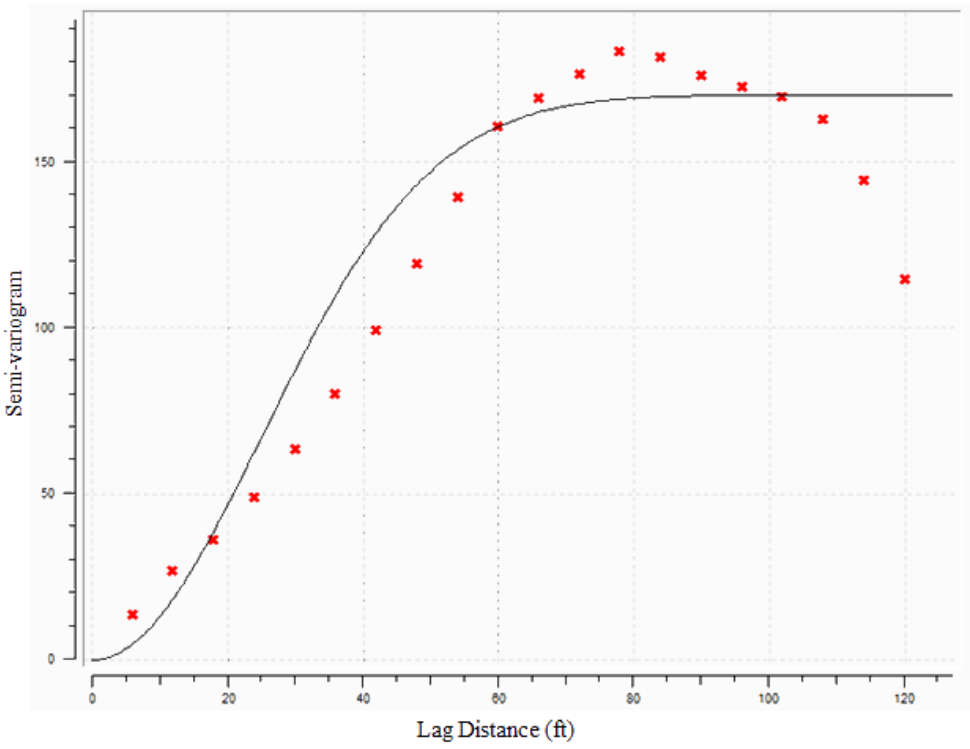

Well 20363 well log variogram

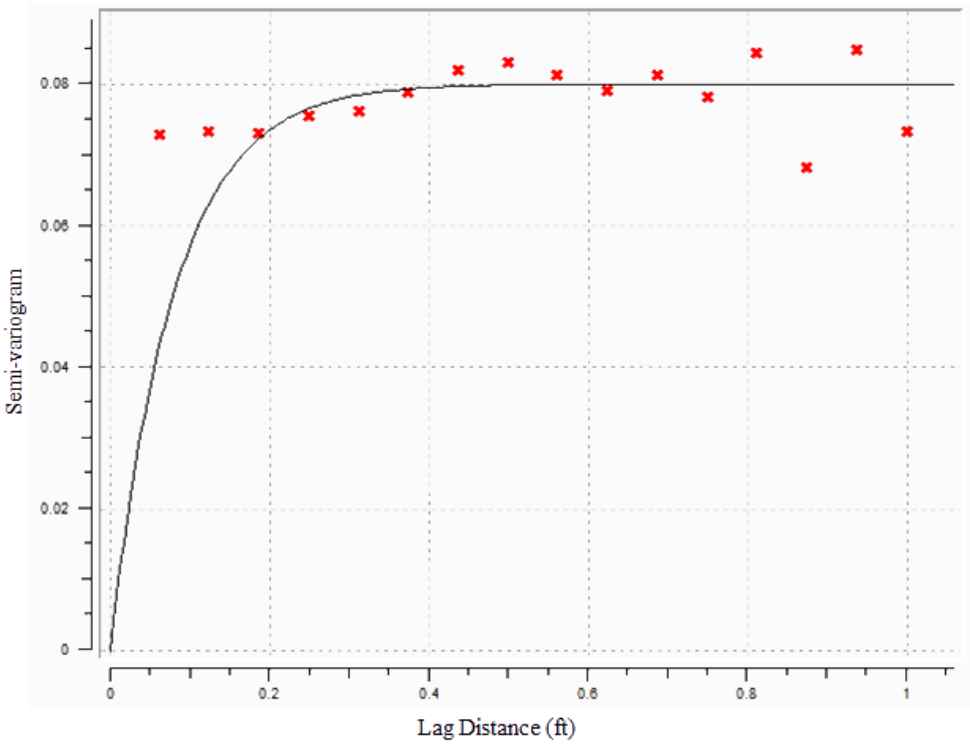

Well 20363 CT variogram

A1.4 Well 20363

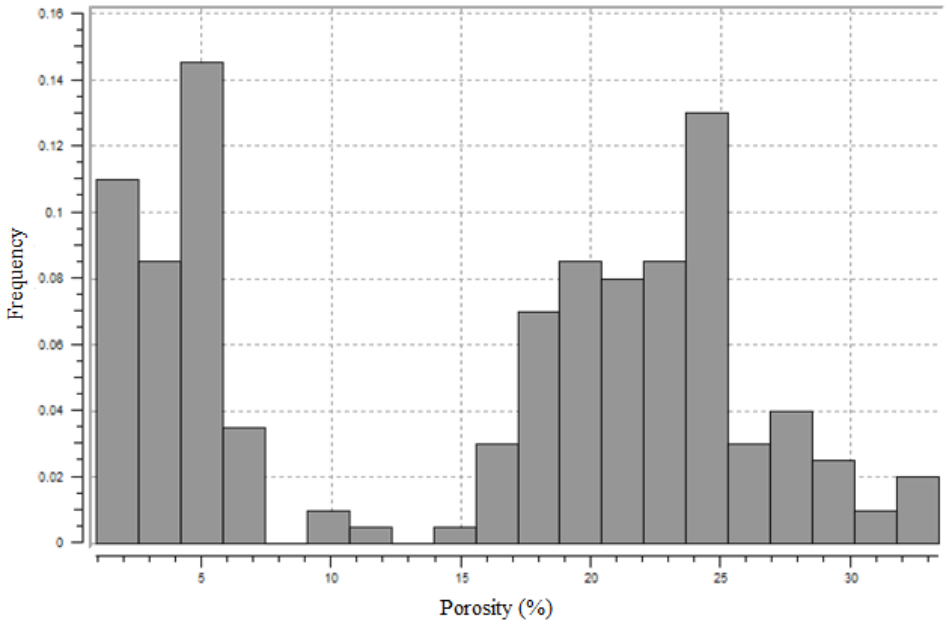

Well 20363 well log histogram

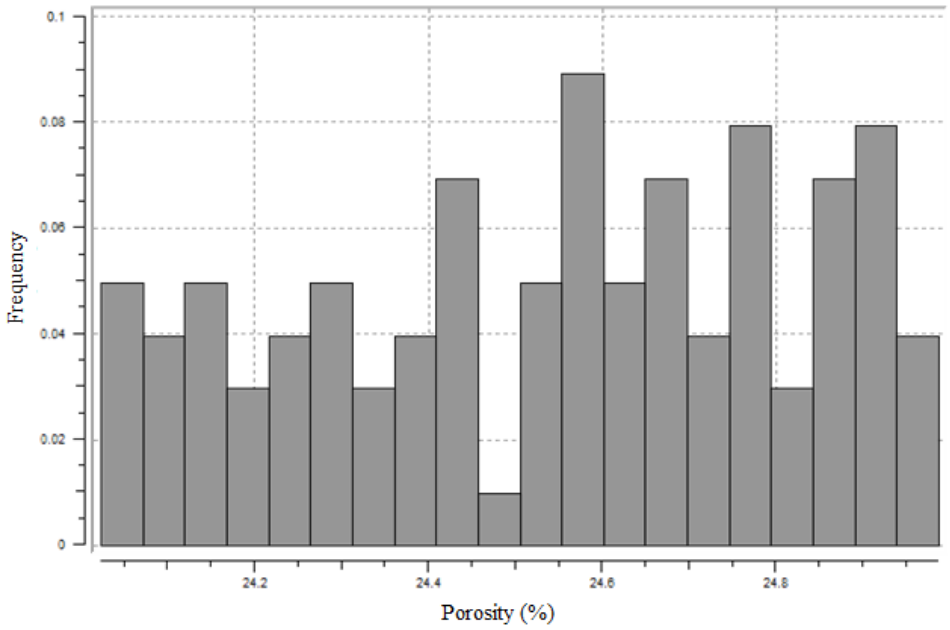

Well 20363 CT histogram

A1.5 Well 20338

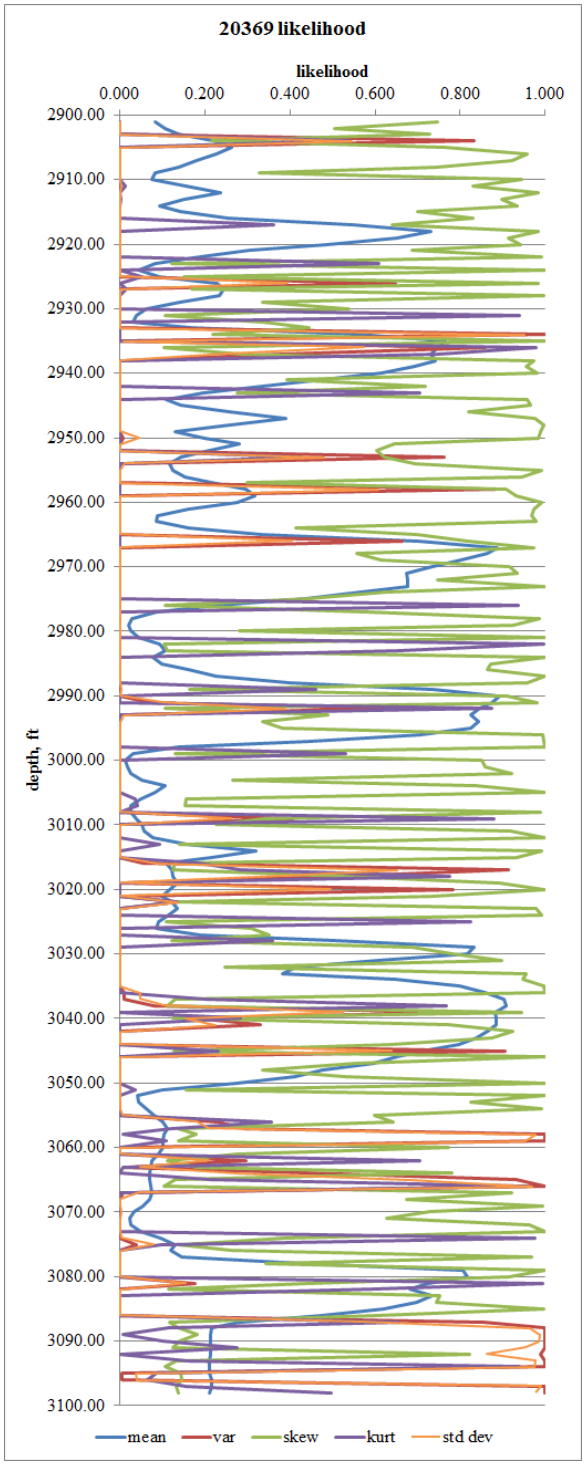

Likelihood for well 20369

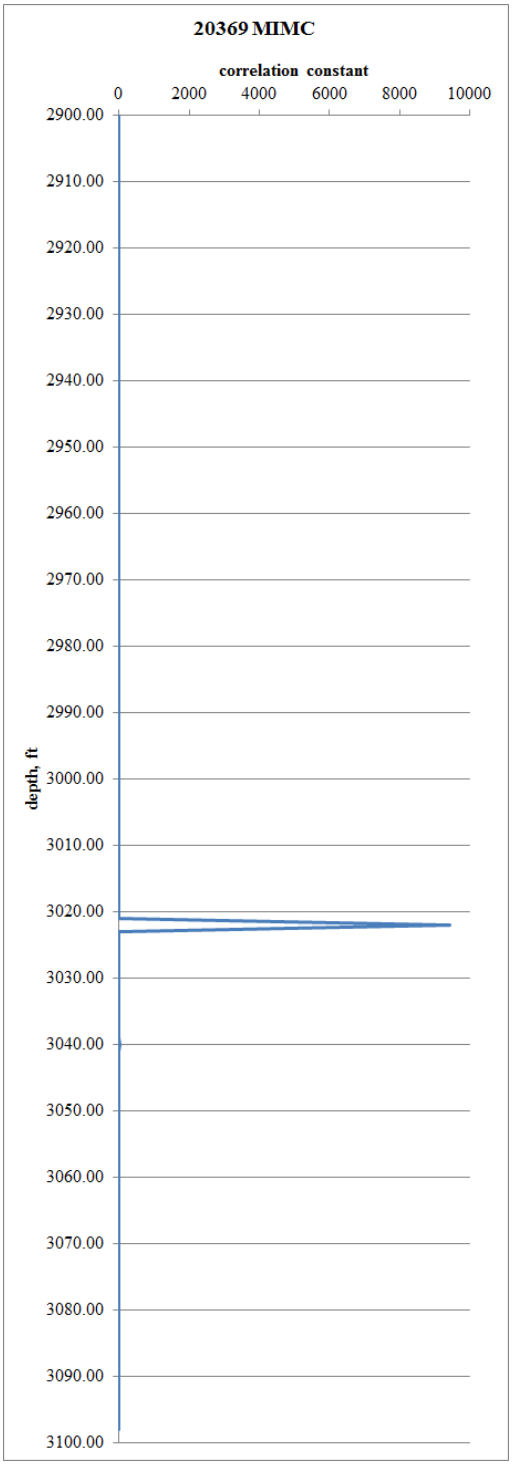

MIMC for well 20369

A1.6 Well 20369

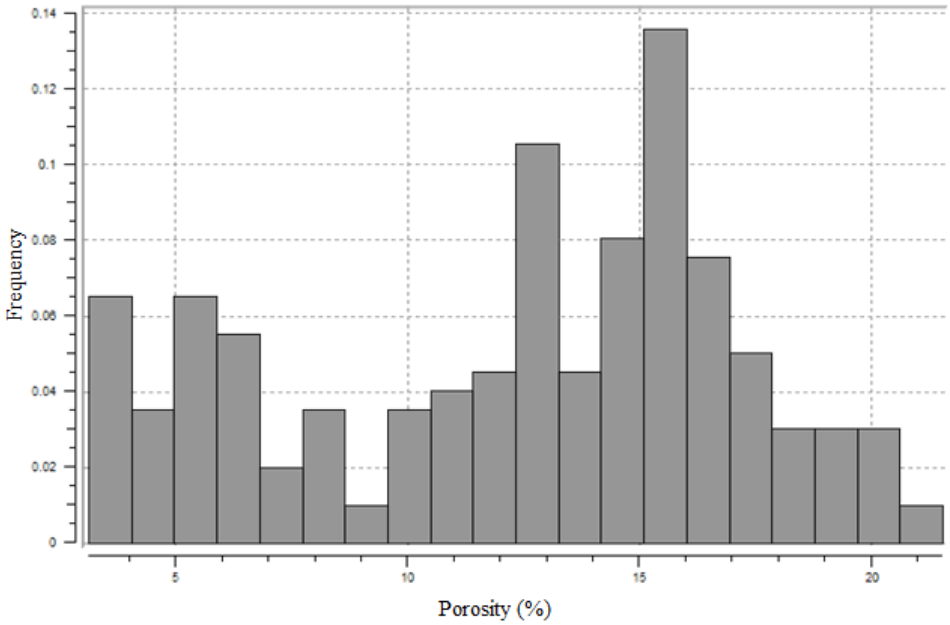

Well 20369 well log histogram

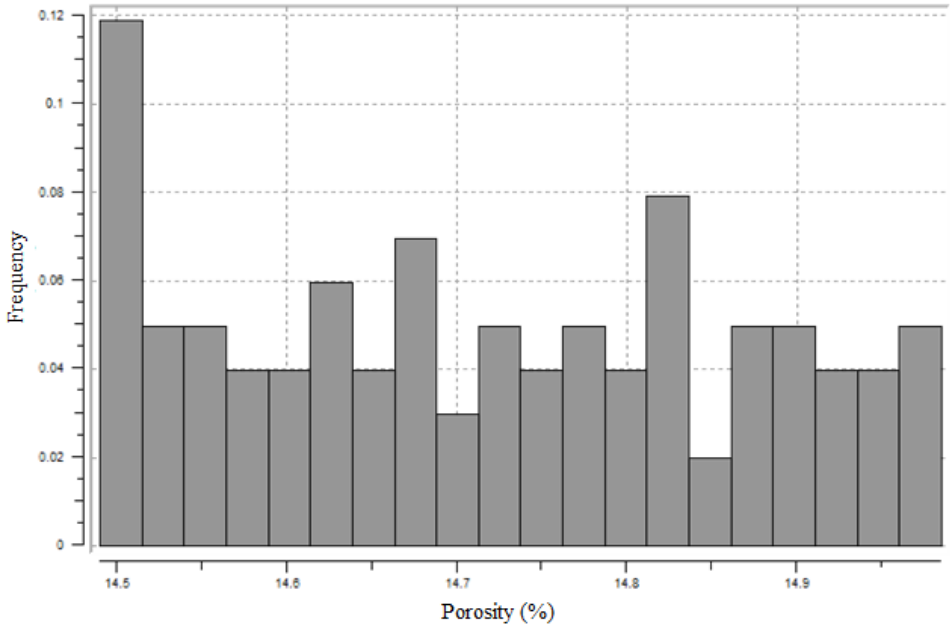

Well 20369 CT histogram

A1.7 Well 20338

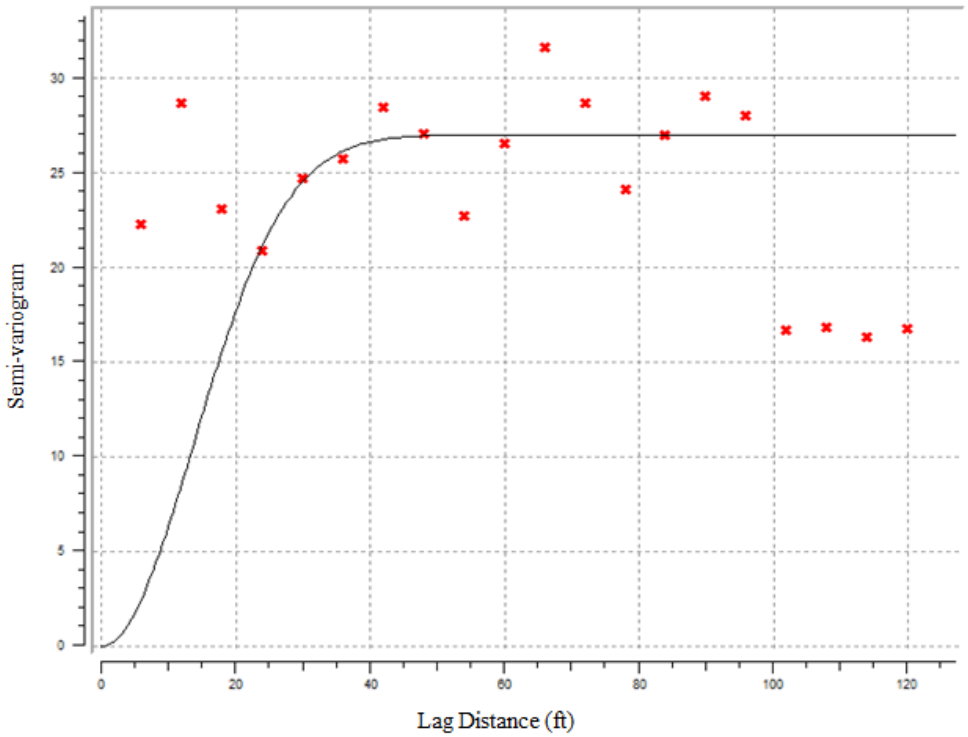

Well 20370 well log variogram

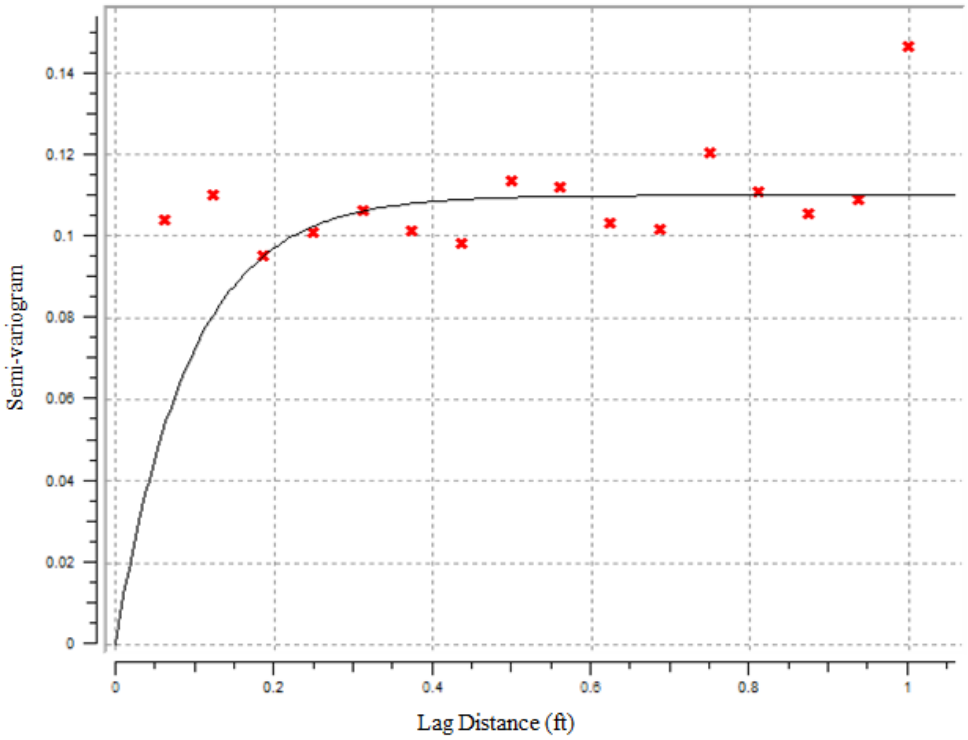

Well 20370 CT variogram

A1.8 Well 20370

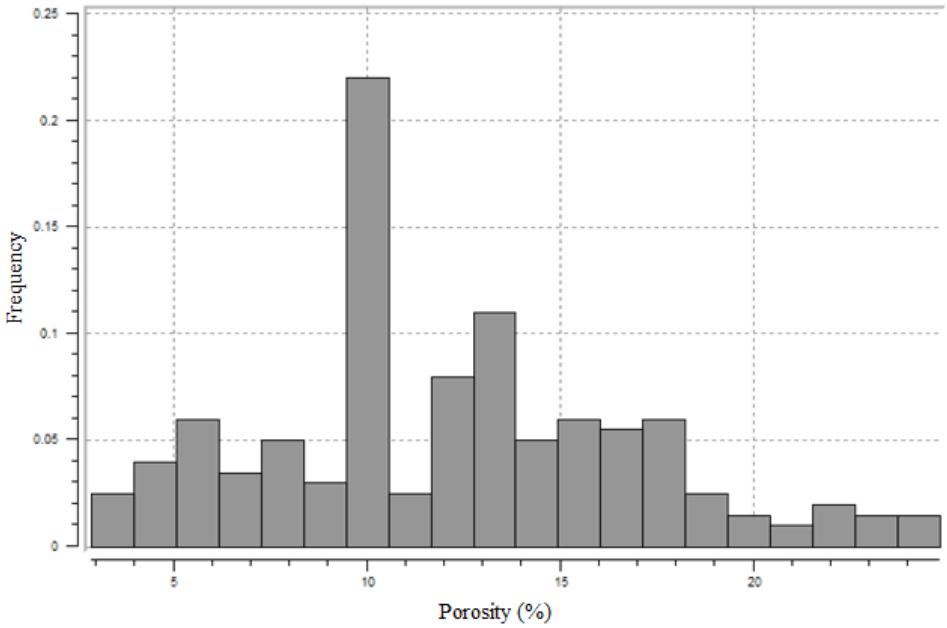

Well 20370 well log histogram

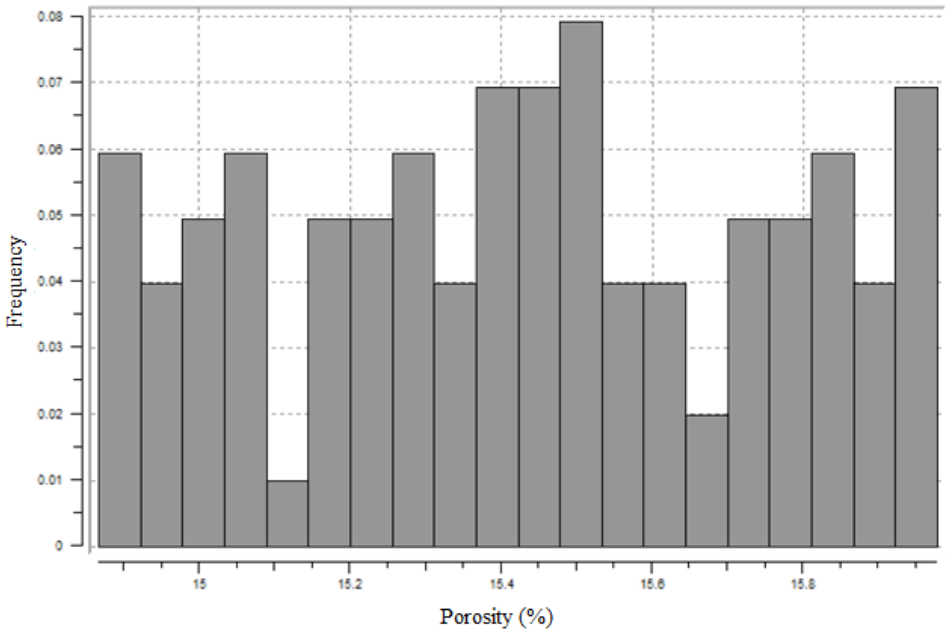

Well 20370 CT histogram

A1.9 Well 20338

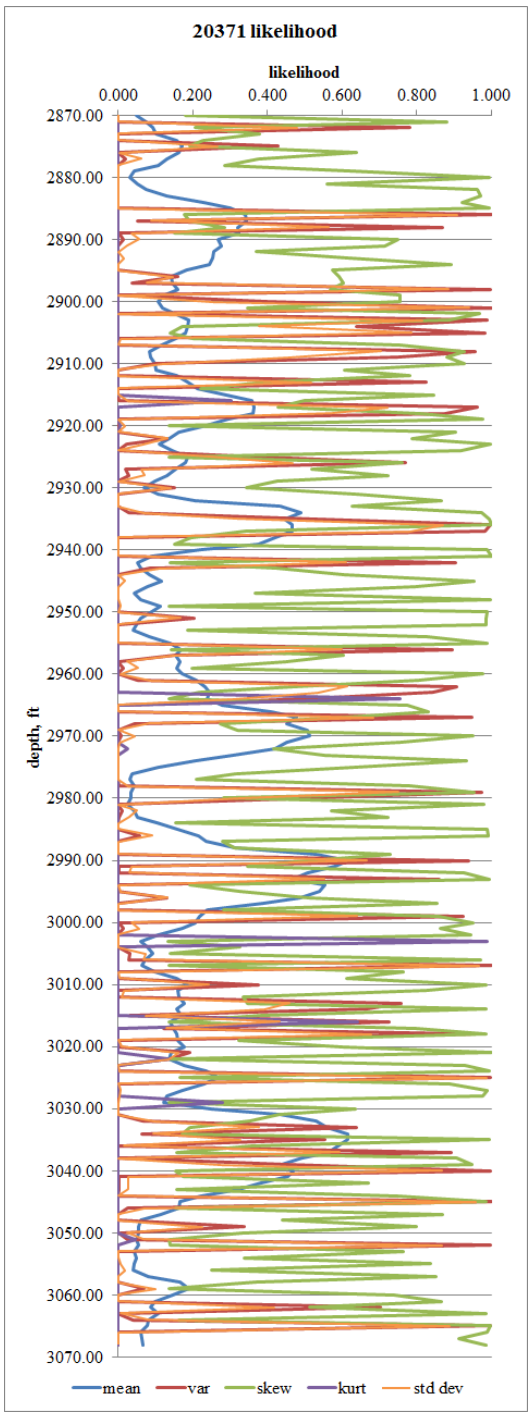

Likelihood for well 20371

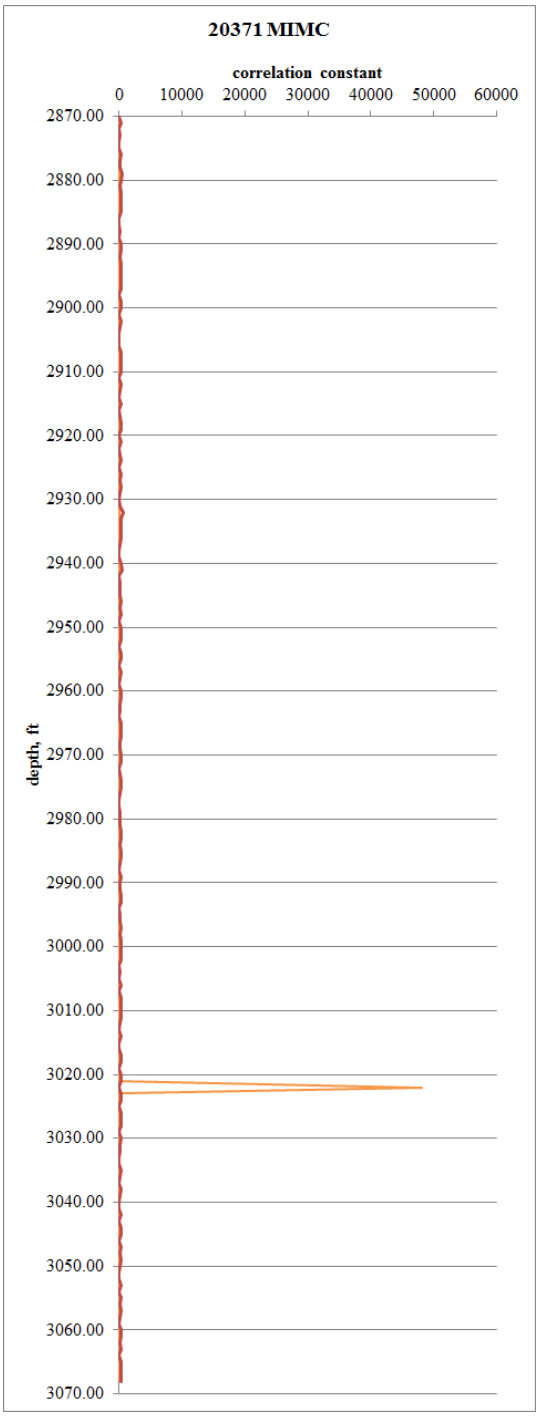

MIMC for well 20371

A1.10 Well 20371

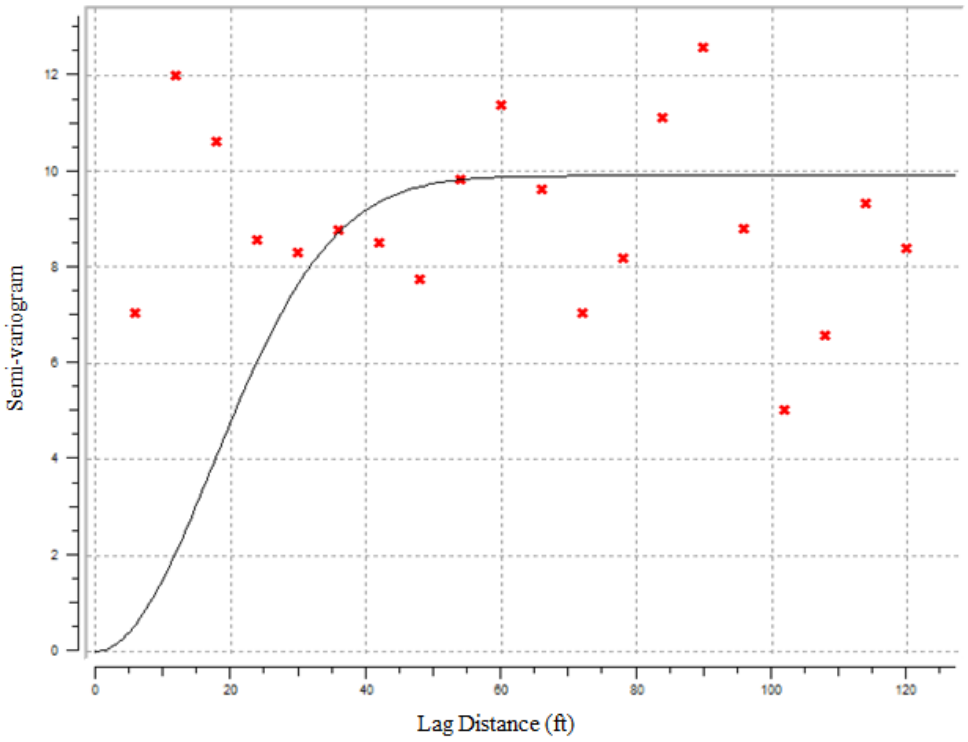

Well 20371 well log variogram

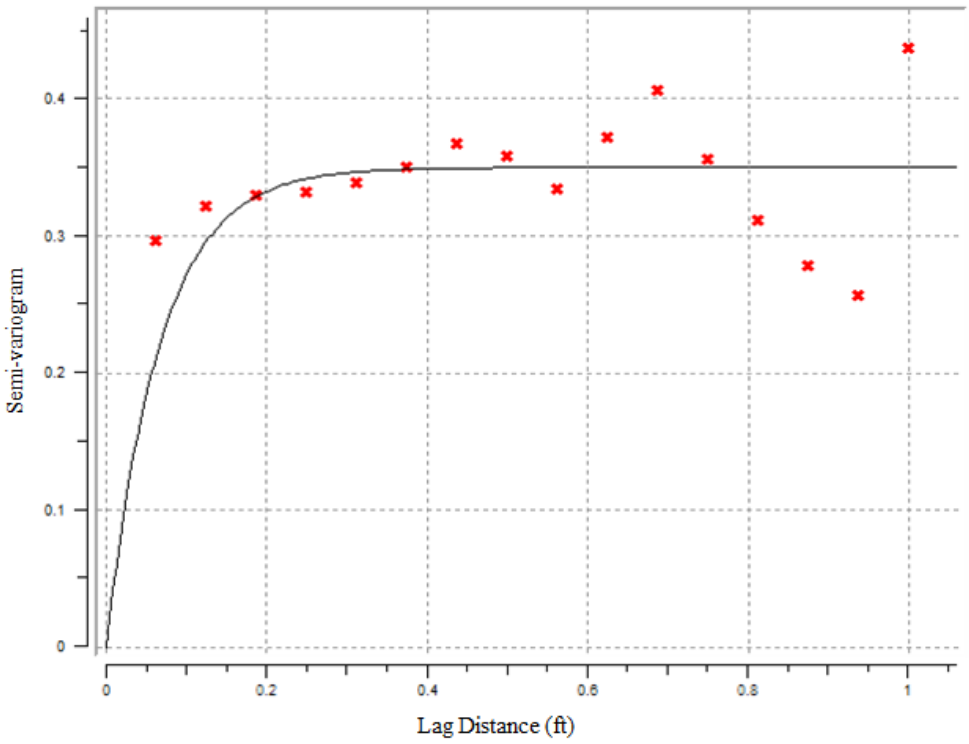

Well 20371 CT variogram

A1.11 Well 20371

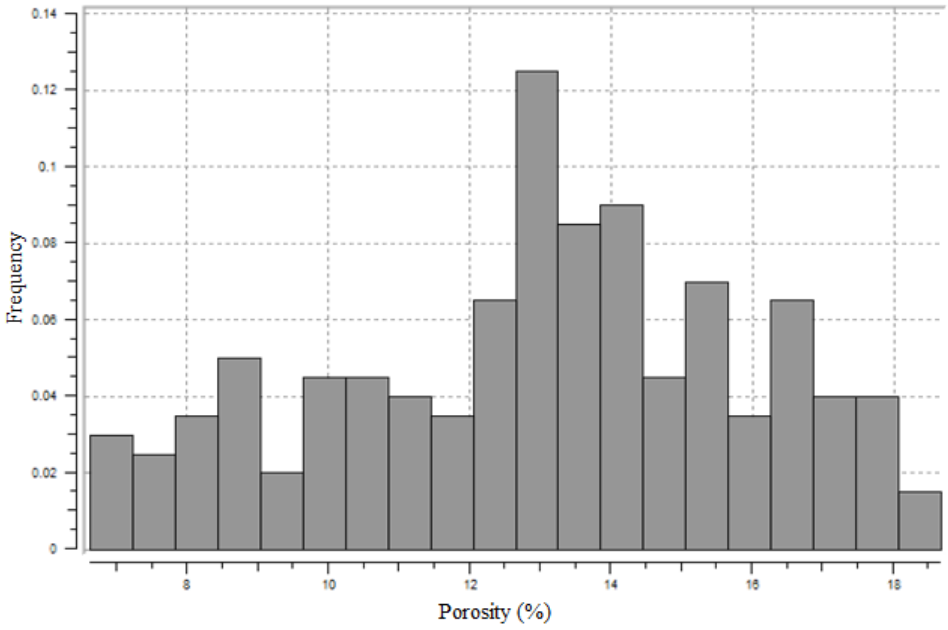

Well 20371 well log histogram

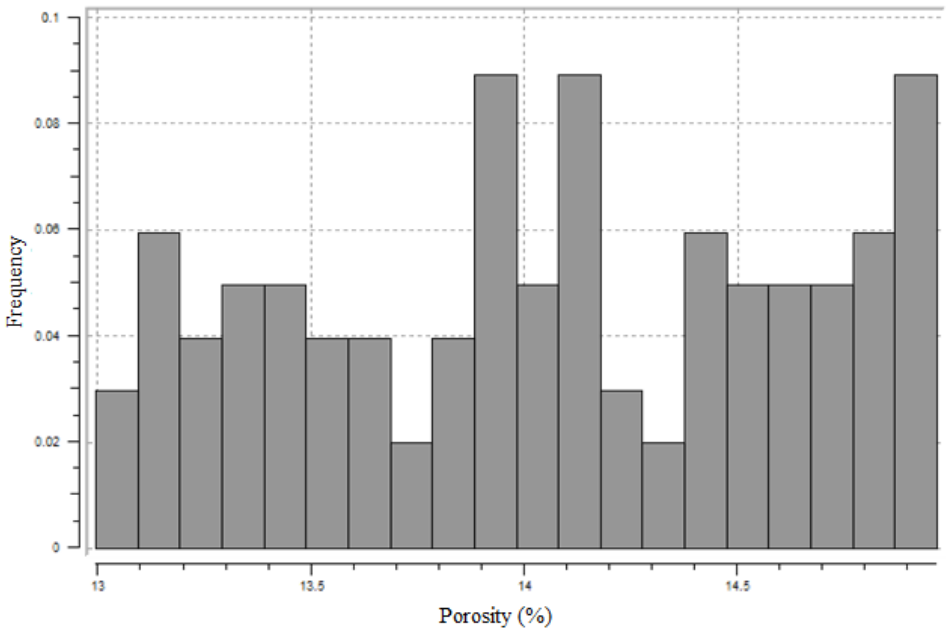

Well 20371 CT histogram

A1.12 Well 20371

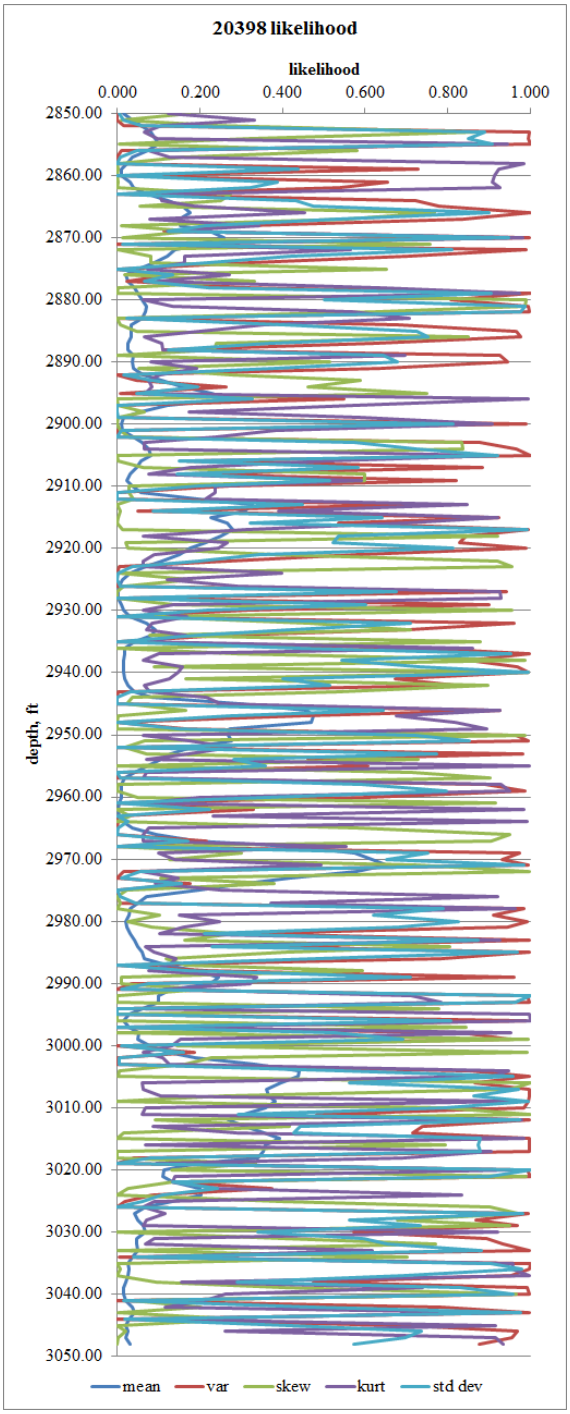

Likelihood for well 20398

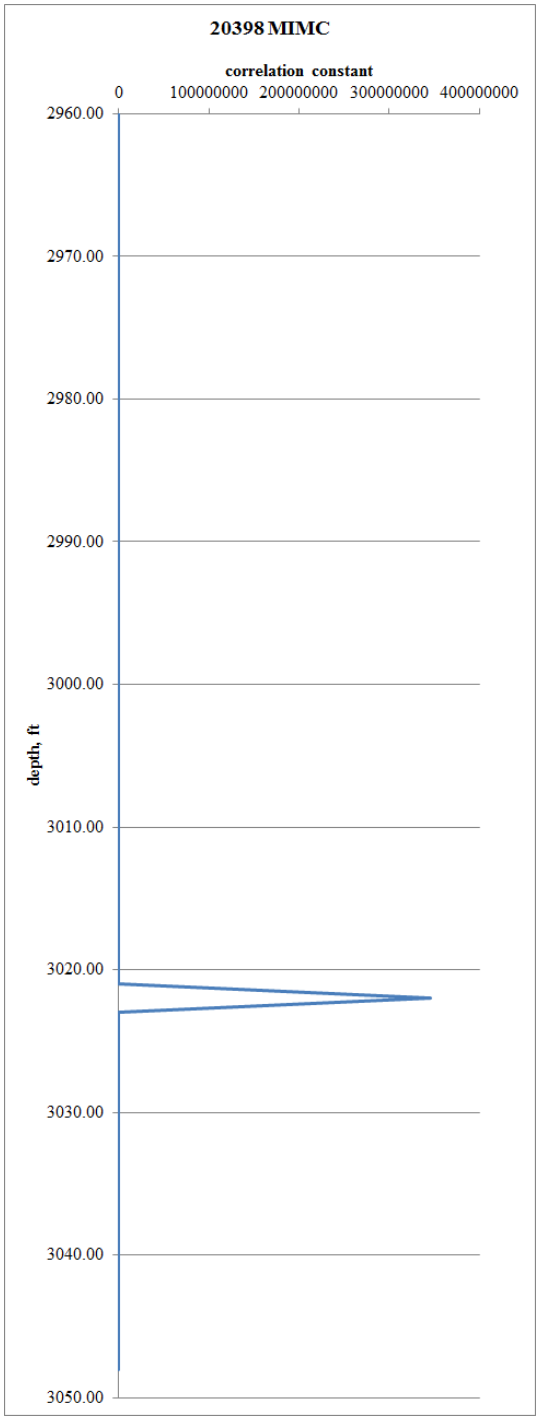

MIMC for well 20398

A1.13 Well 20398

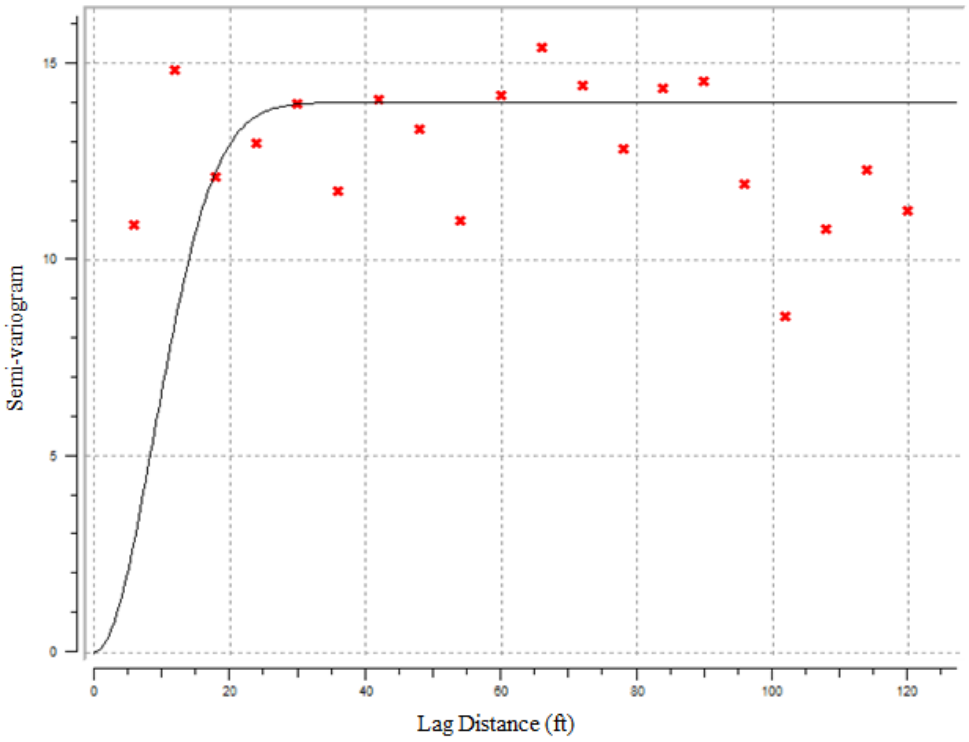

Well 20398 well log variogram

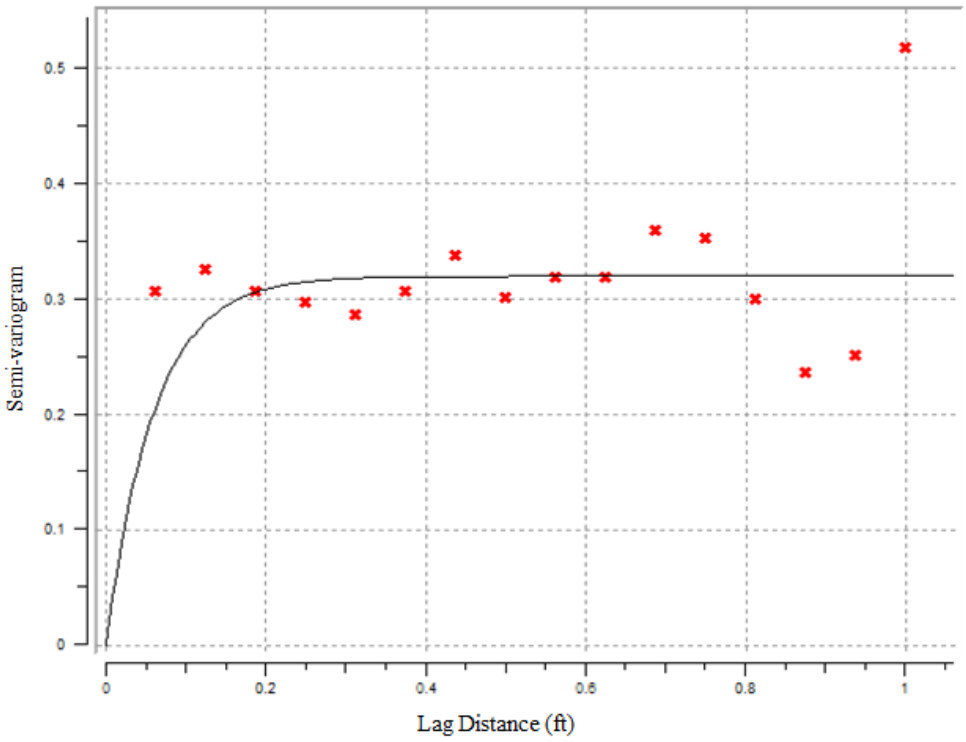

Well 20398 CT variogram

A1.14 Well 20398

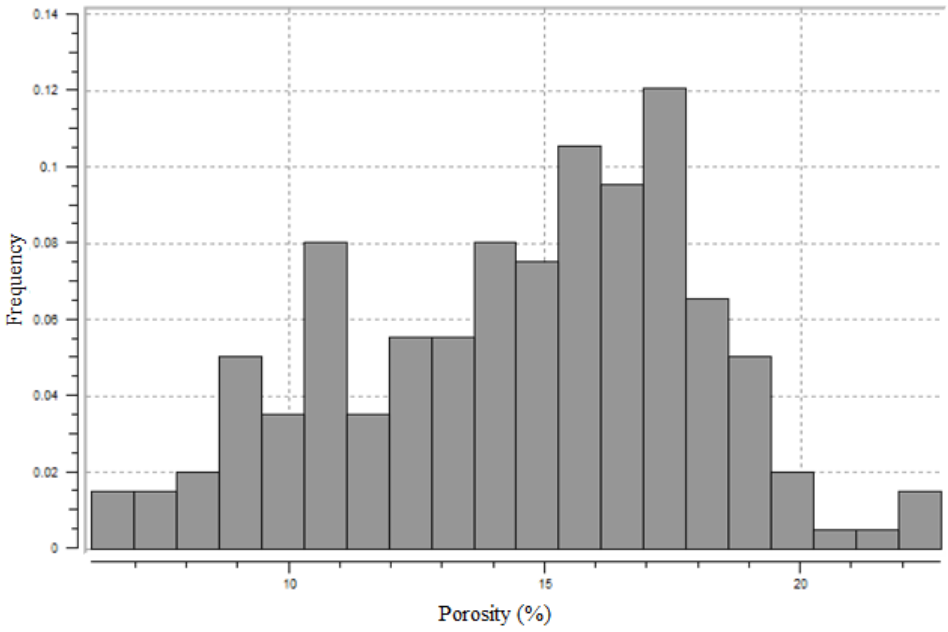

Well 20398 well log histogram

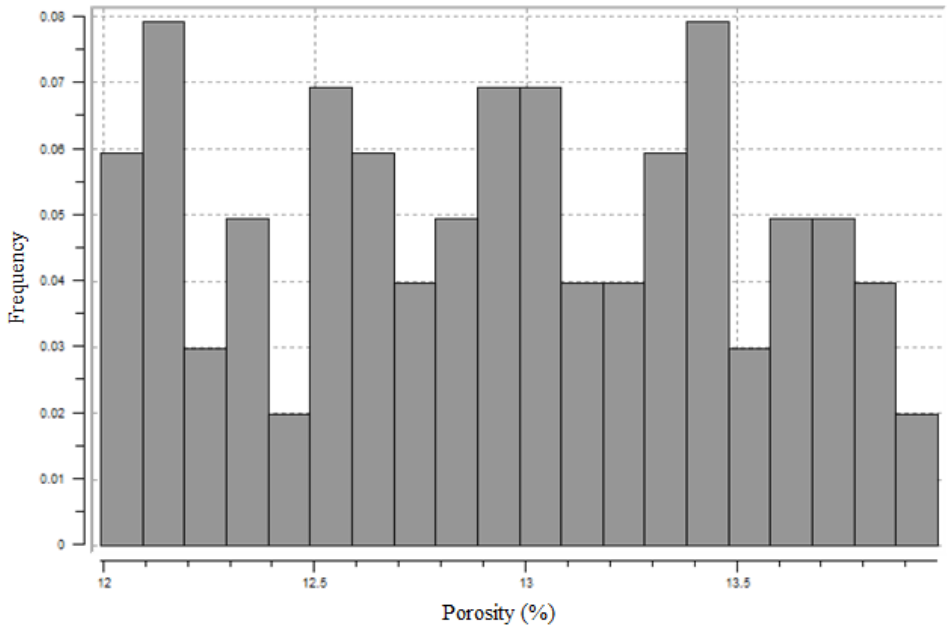

Well 20398 CT histogram

A1.15 Well 20398

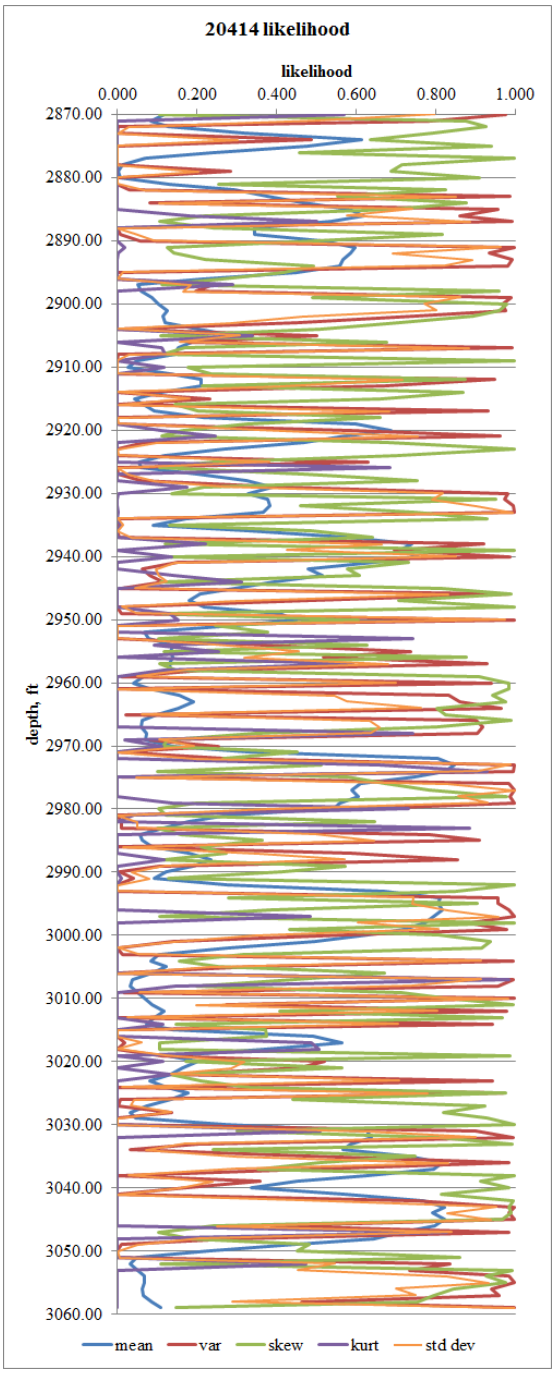

Likelihood for well 20414

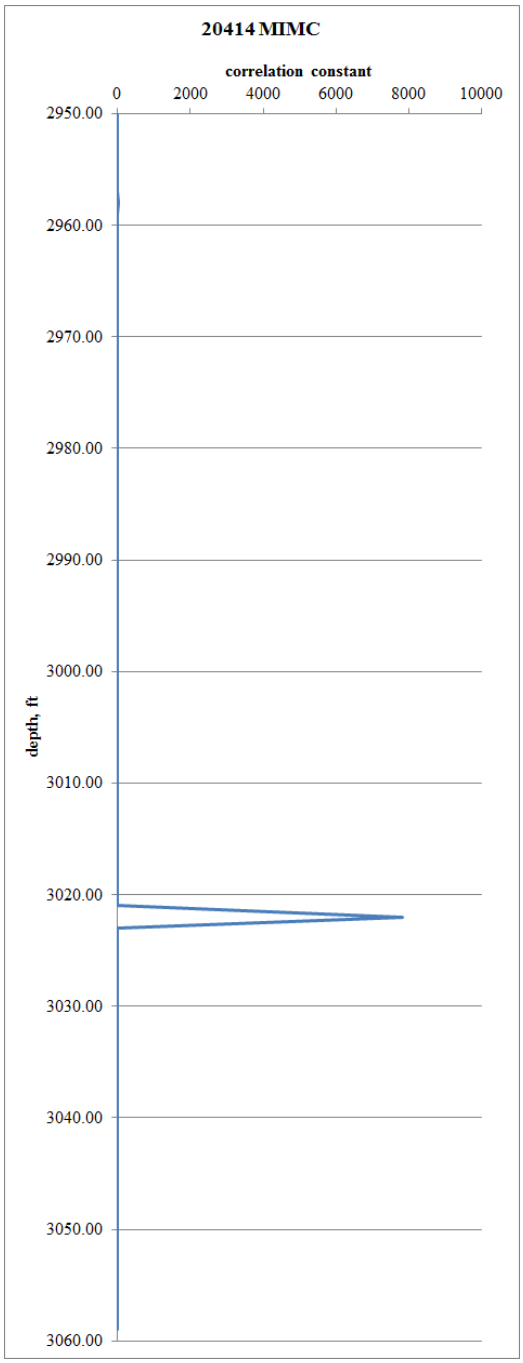

MIMC for well 20414

A1.16 Well 20414

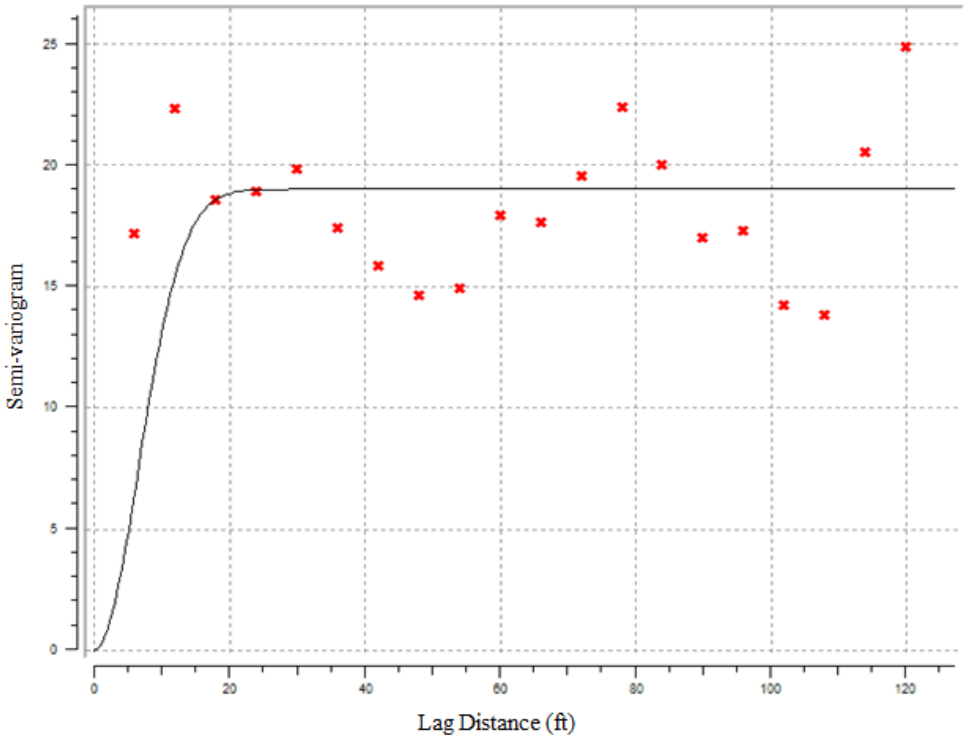

Well 20414 well log variogram

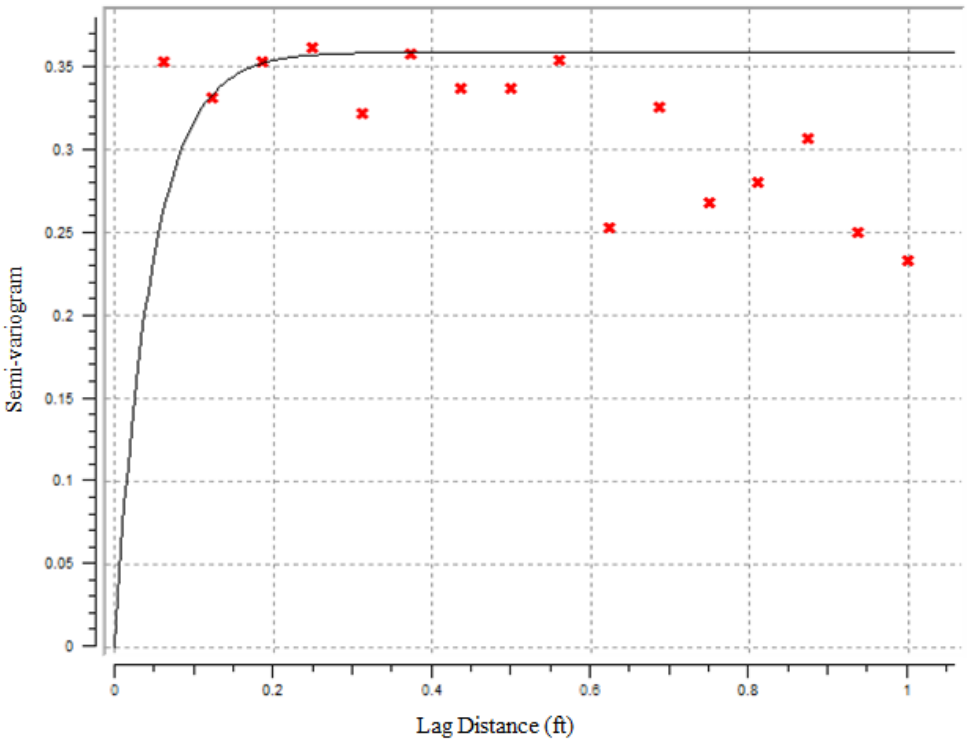

Well 20414 CT variogram

A1.17 Well 20414

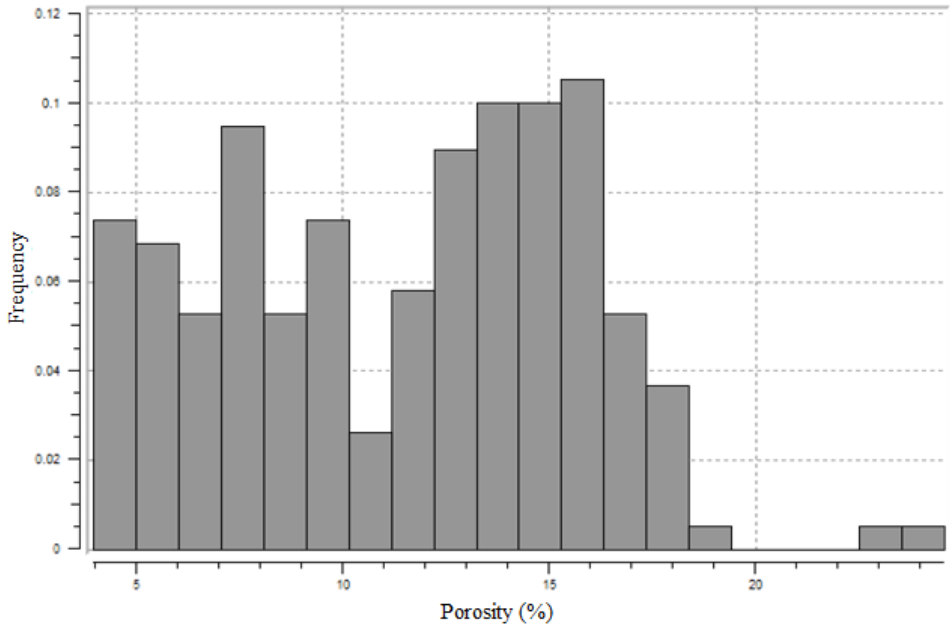

Well 20414 well log histogram

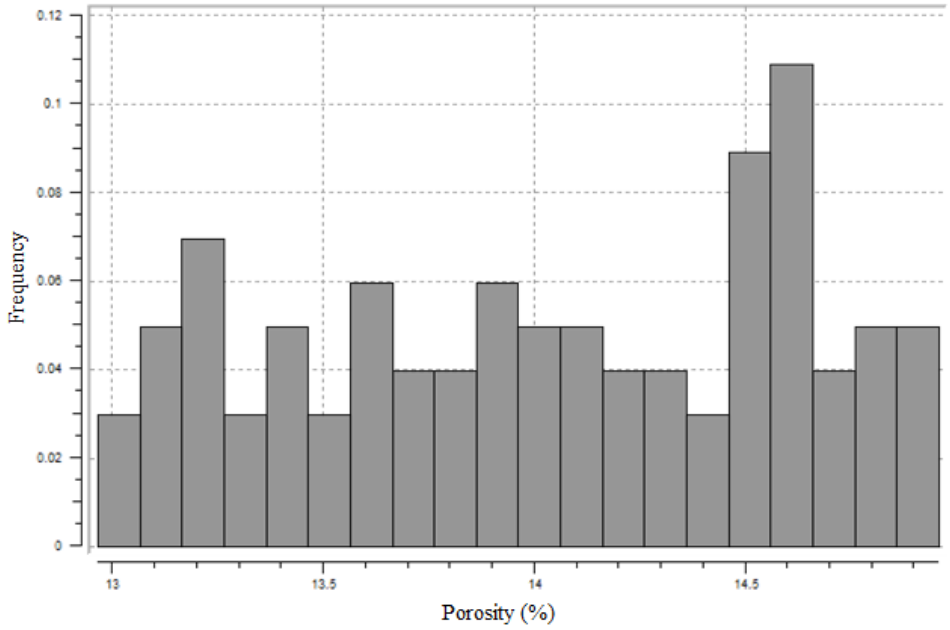

Well 20414 CT histogram

A1.18 Well 20414

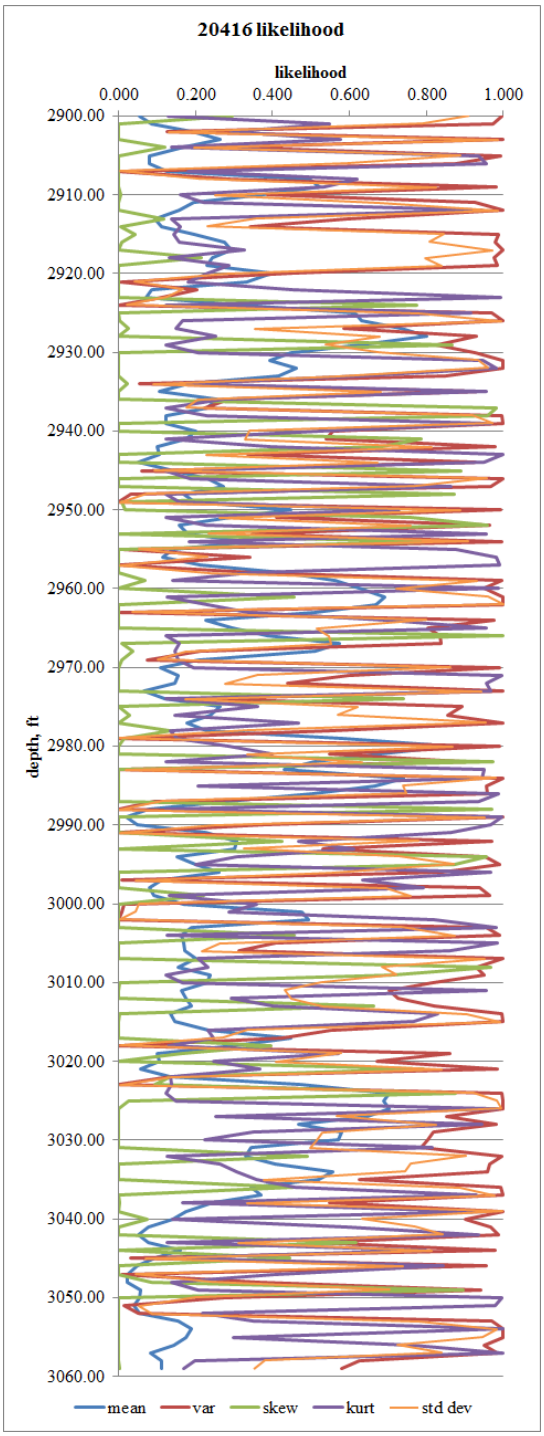

Likelihood for well 20416

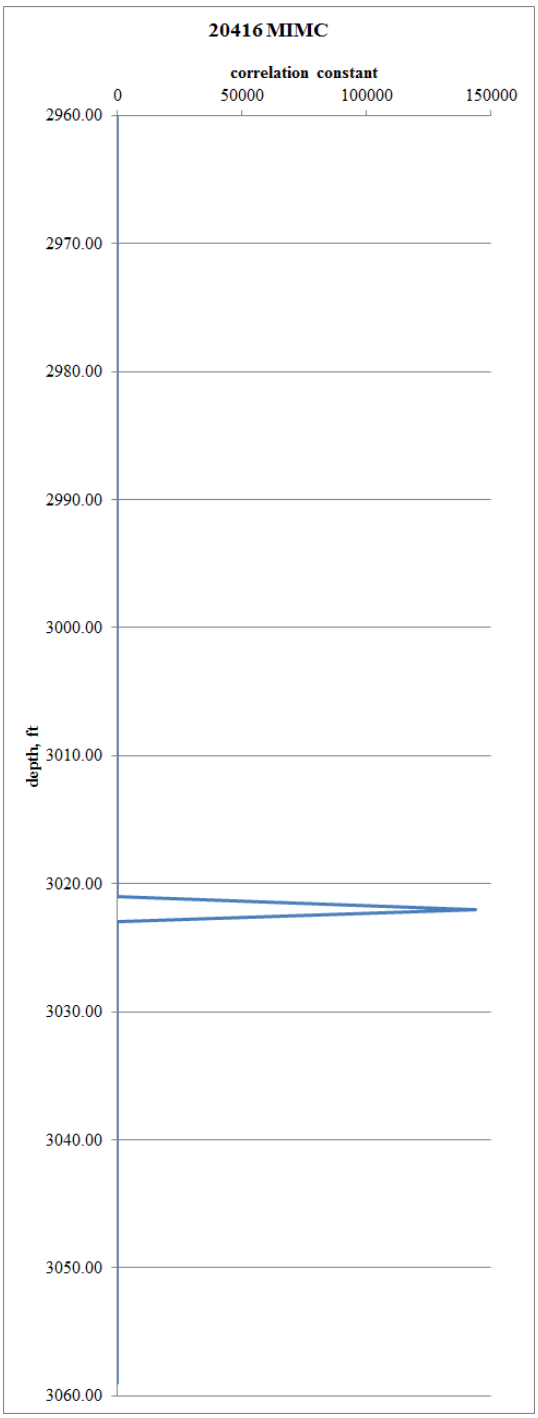

MIMC for well 20416

A1.19 Well 20416

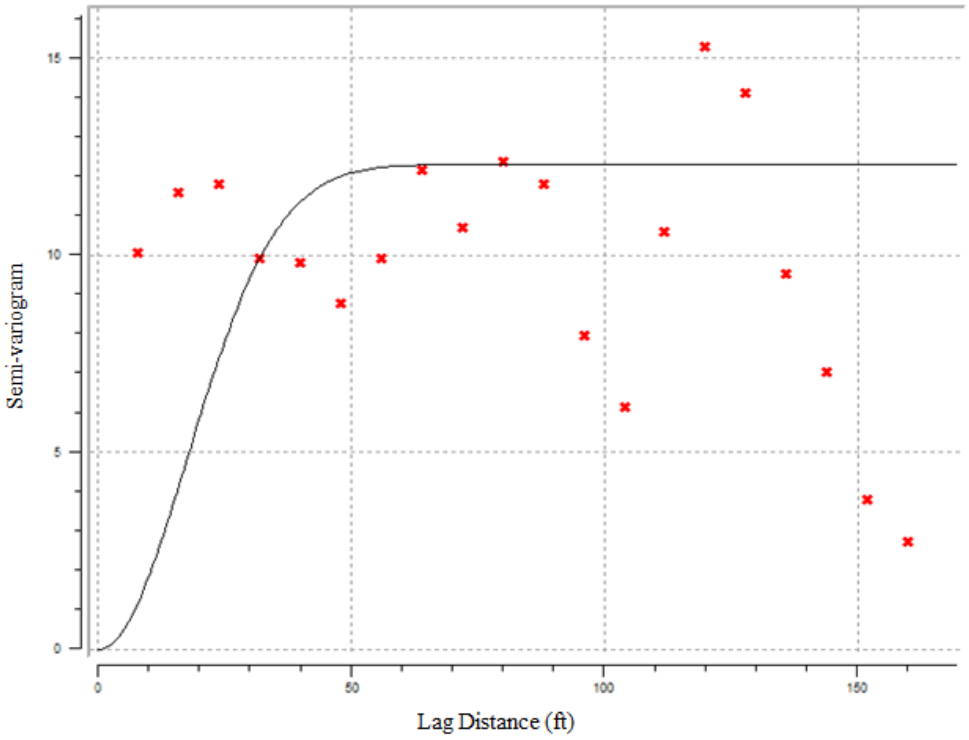

Well 20416 well log variogram

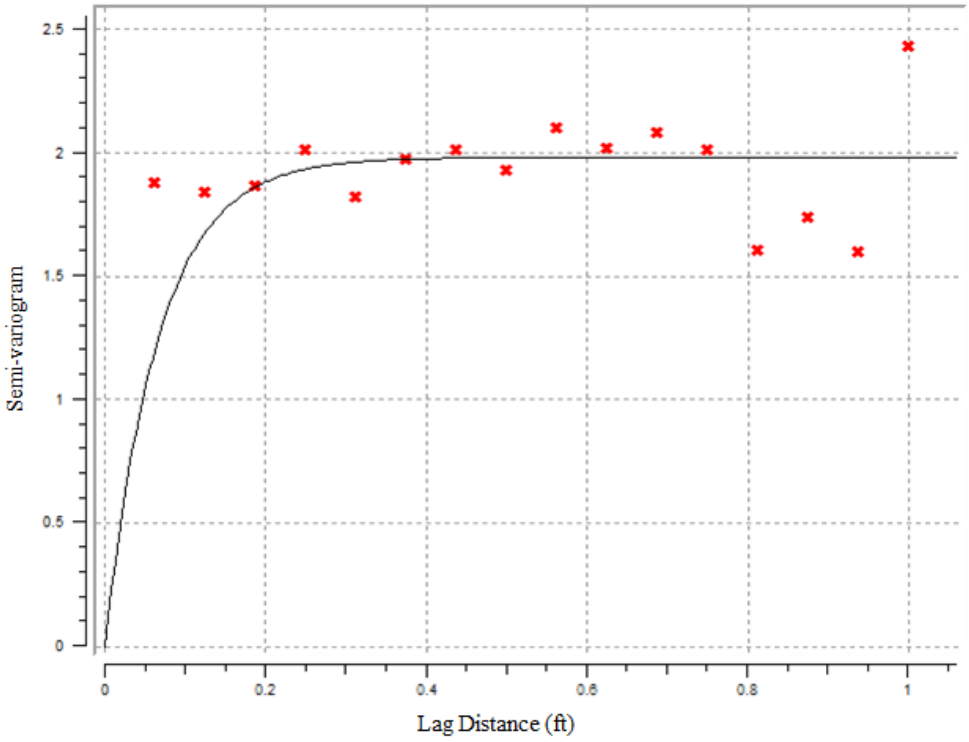

Well 20416 CT variogram

A1.20 Well 20416

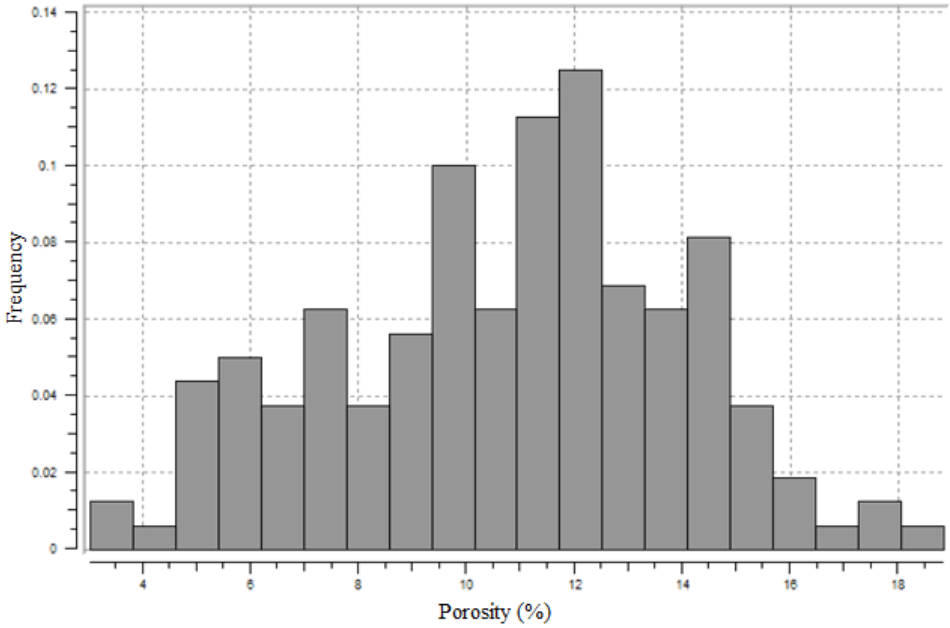

Well 20416 well log histogram

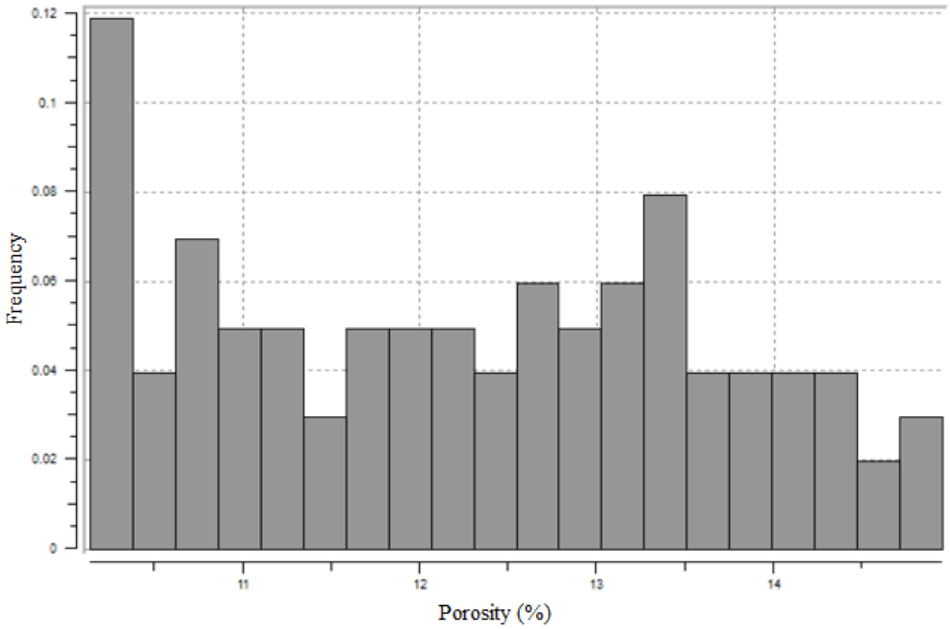

Well 20416 CT histogram

A1.21 Well 20416

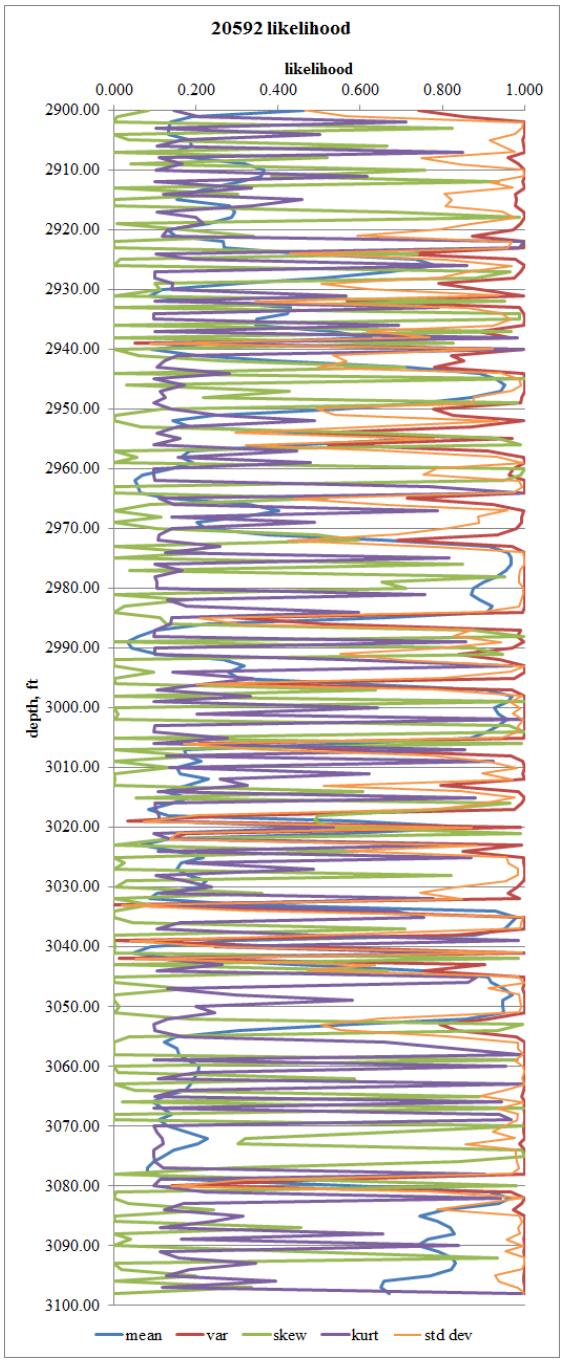

Likelihood for well 20592

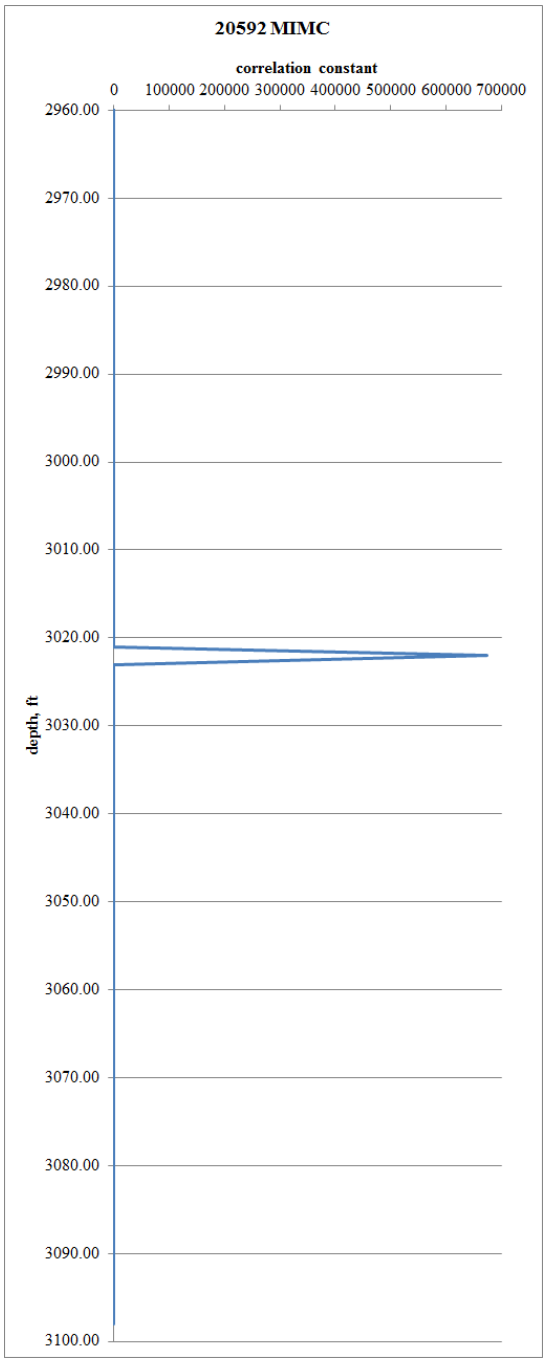

MIMC for well 20592

A1.22 Well 20592

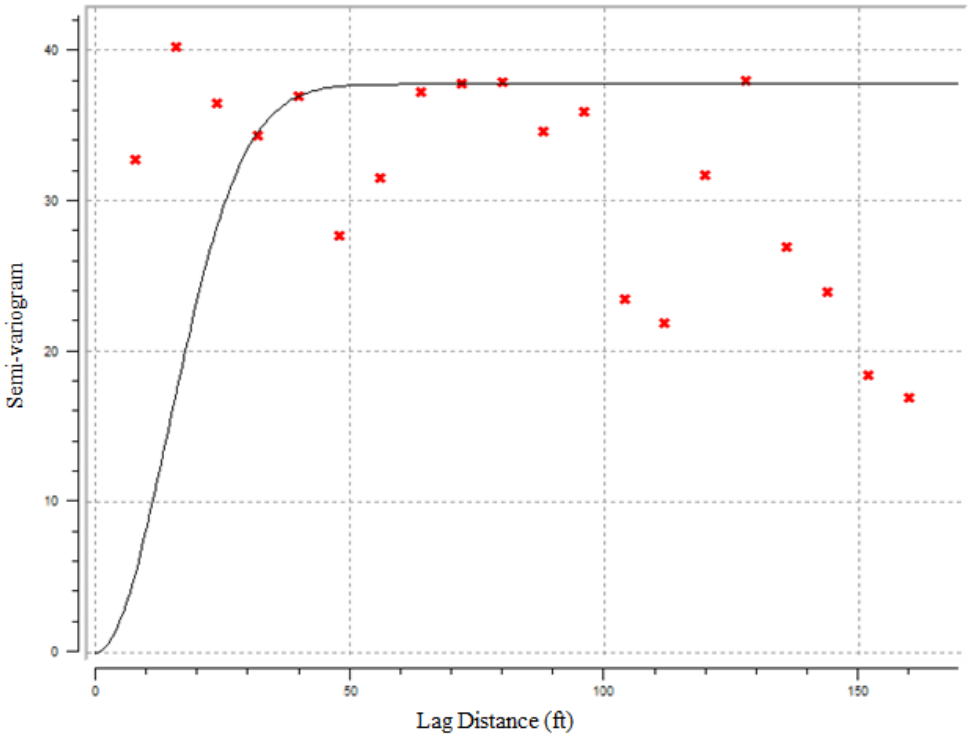

Well 20592 well log variogram

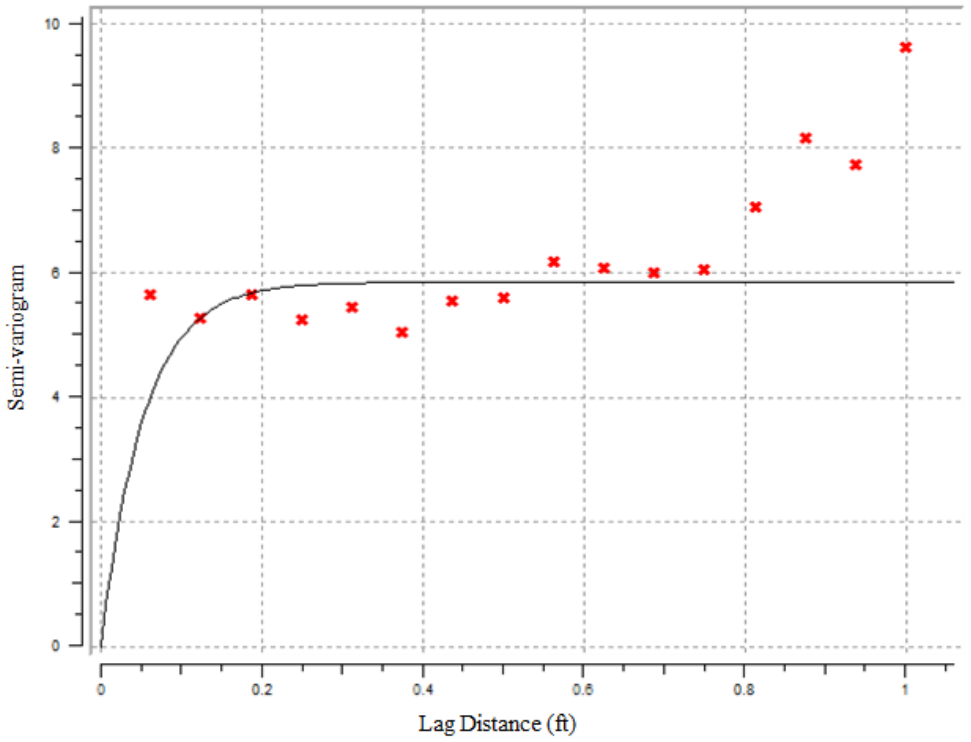

Well 20592 CT variogram

A1.23 Well 20592

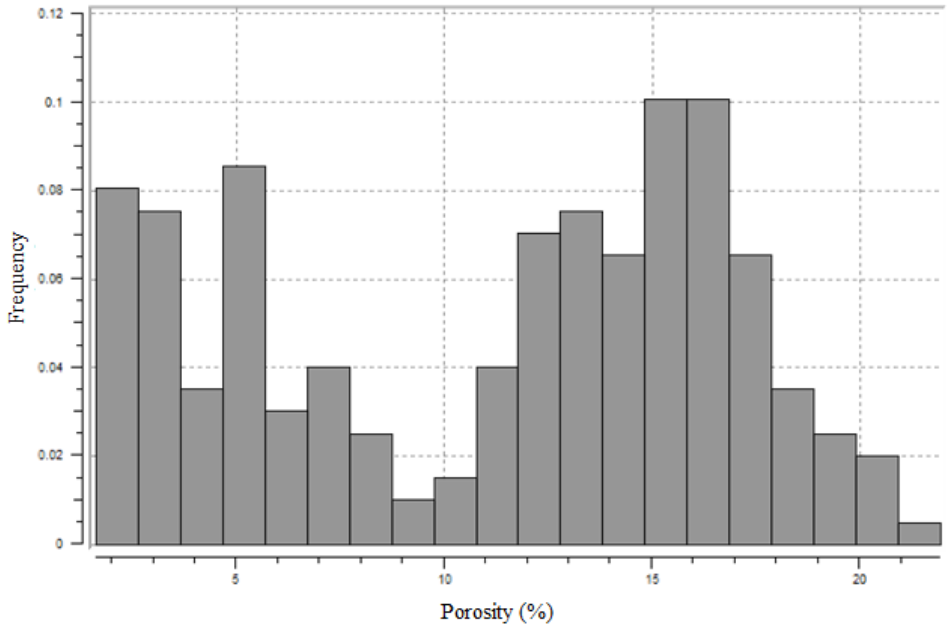

Well 20592 well log histogram

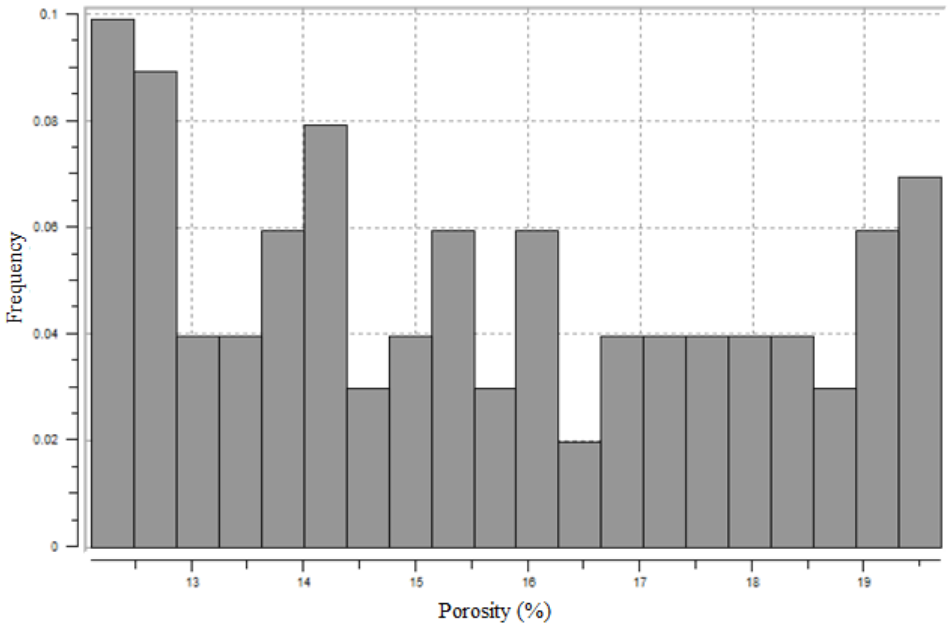

Well 20592 CT histogram

A1.24 Well 20592

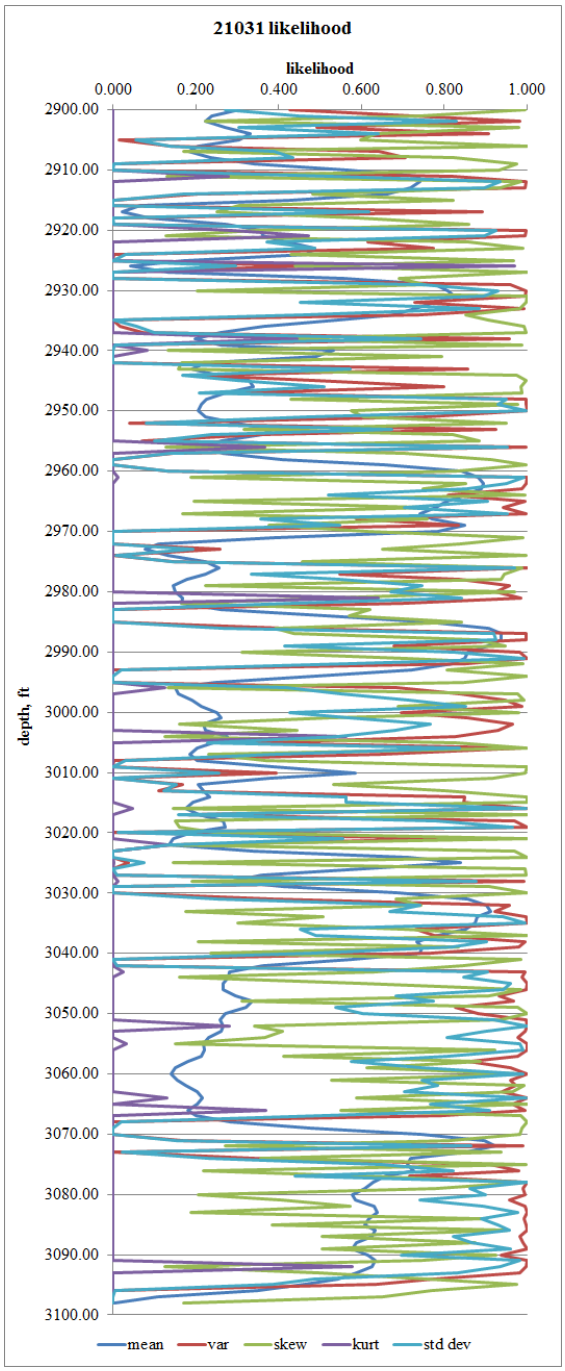

Likelihood for well 21031

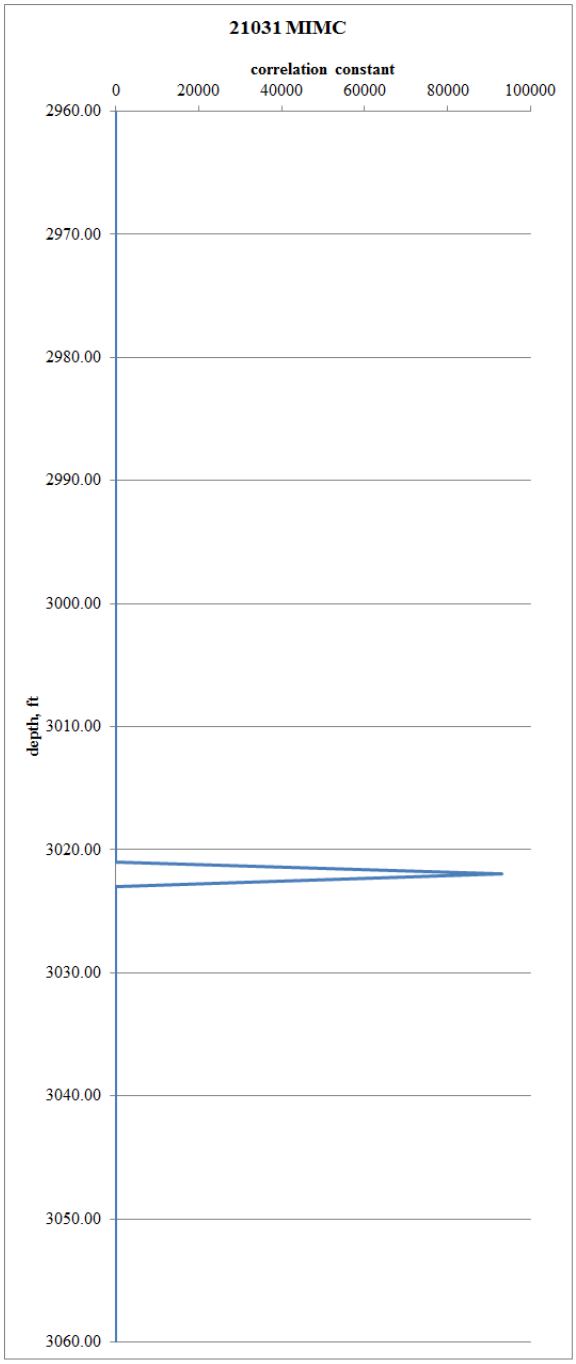

MIMC for well 21031

A1.25 Well 21031

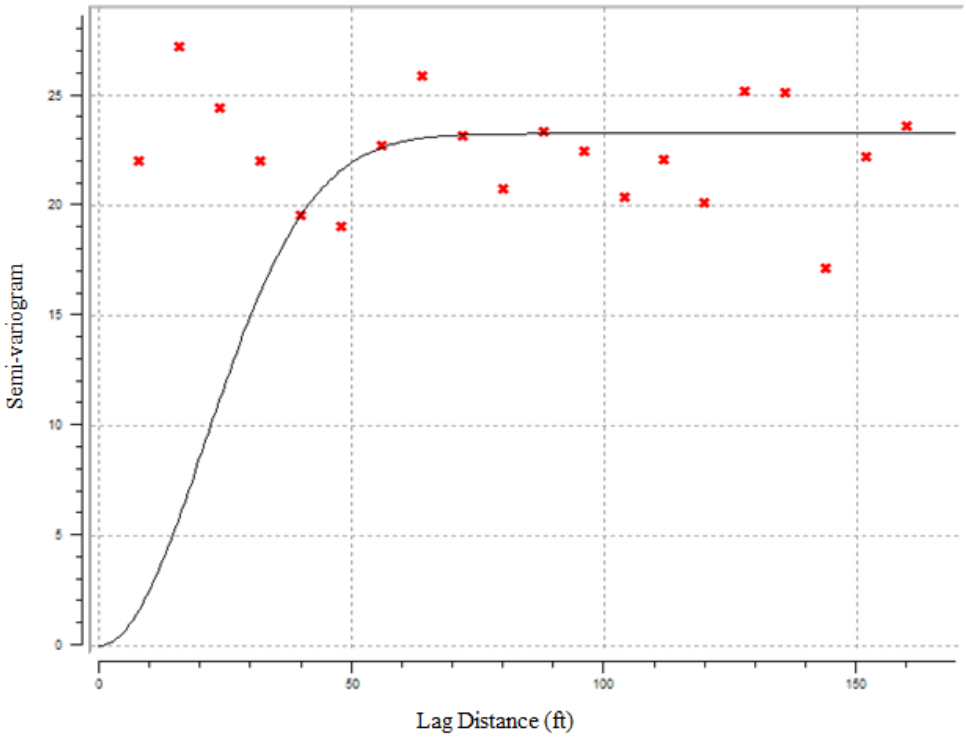

Well 21031 well log variogram

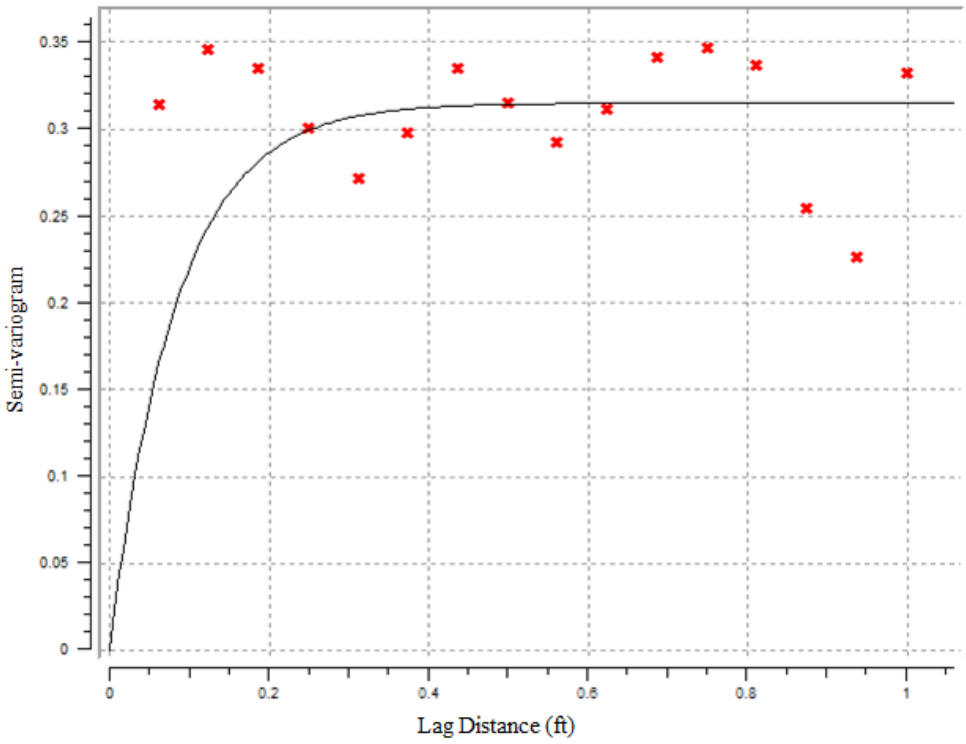

Well 21031 CT variogram

A1.26 Well 21031

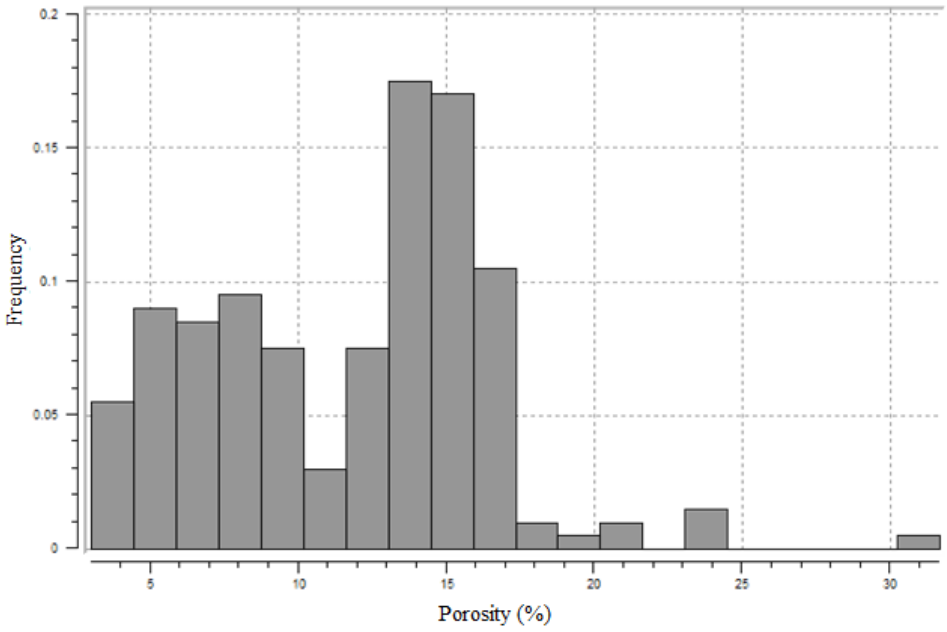

Well 21031 well log histogram

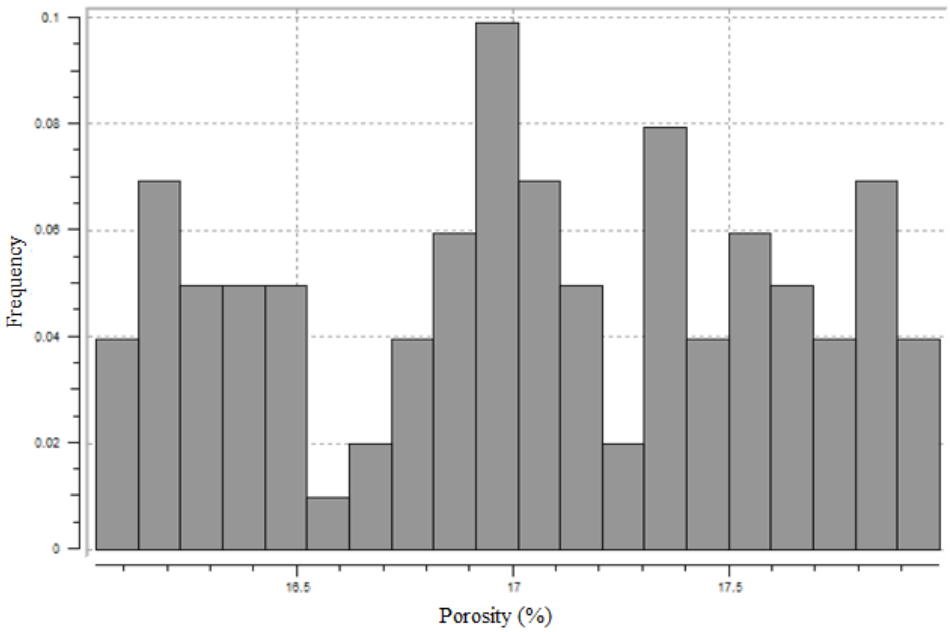

Well 21031 CT histogram

A1.27 Well 21031

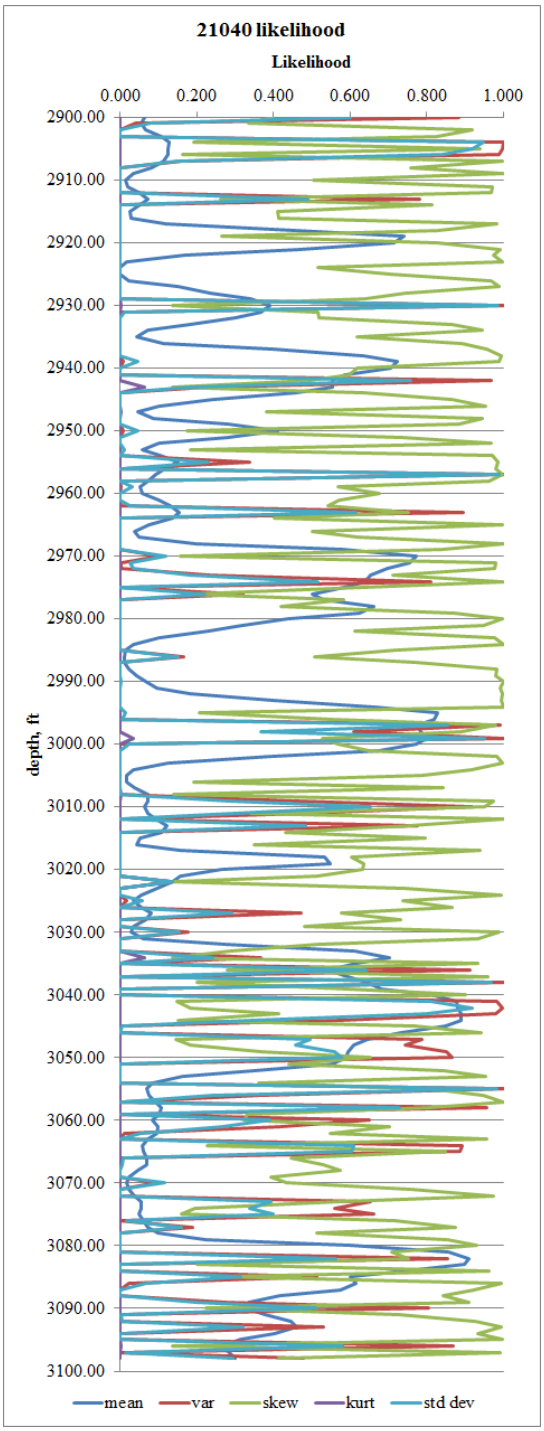

Likelihood for well 21040

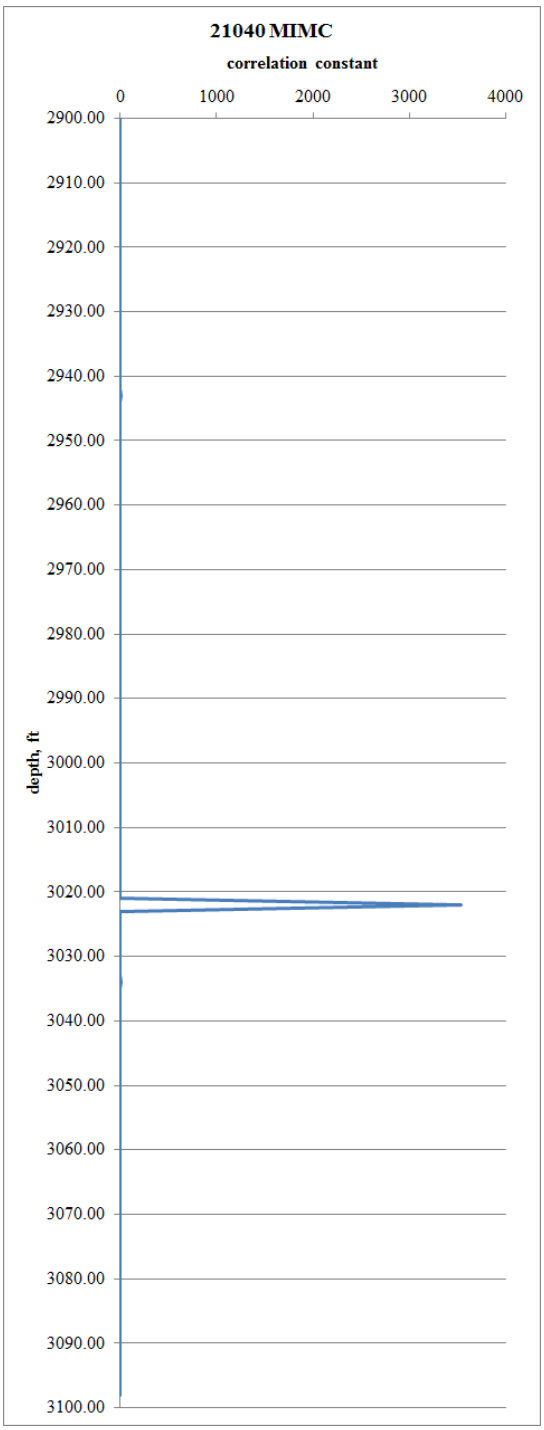

MIMC for well 21040

A1.28 Well 21040

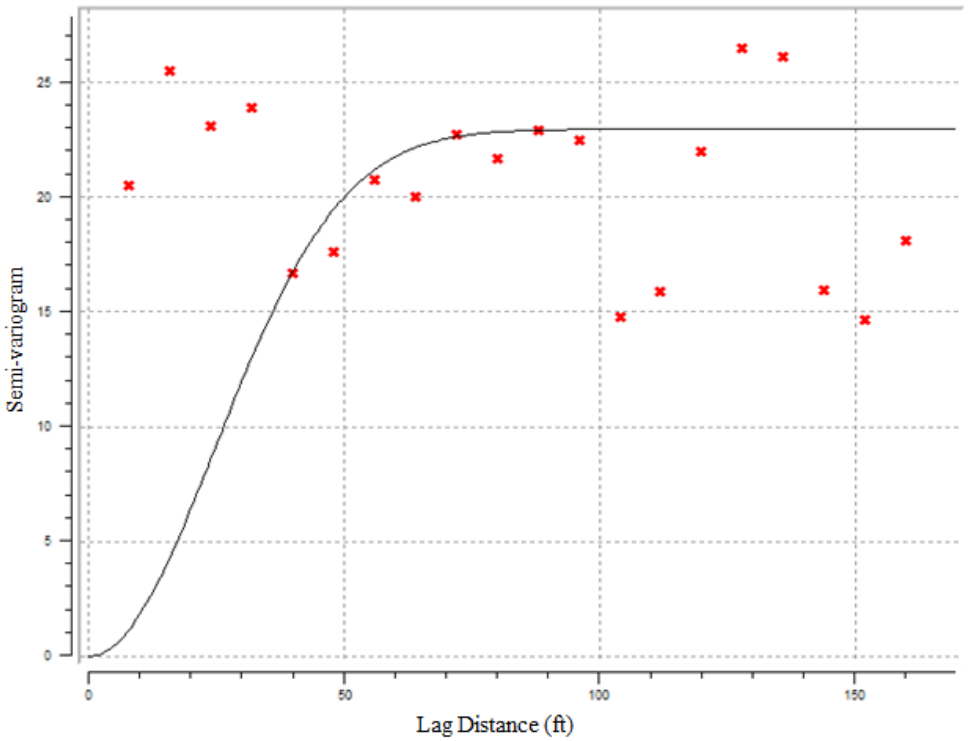

Well 21040 well log variogram

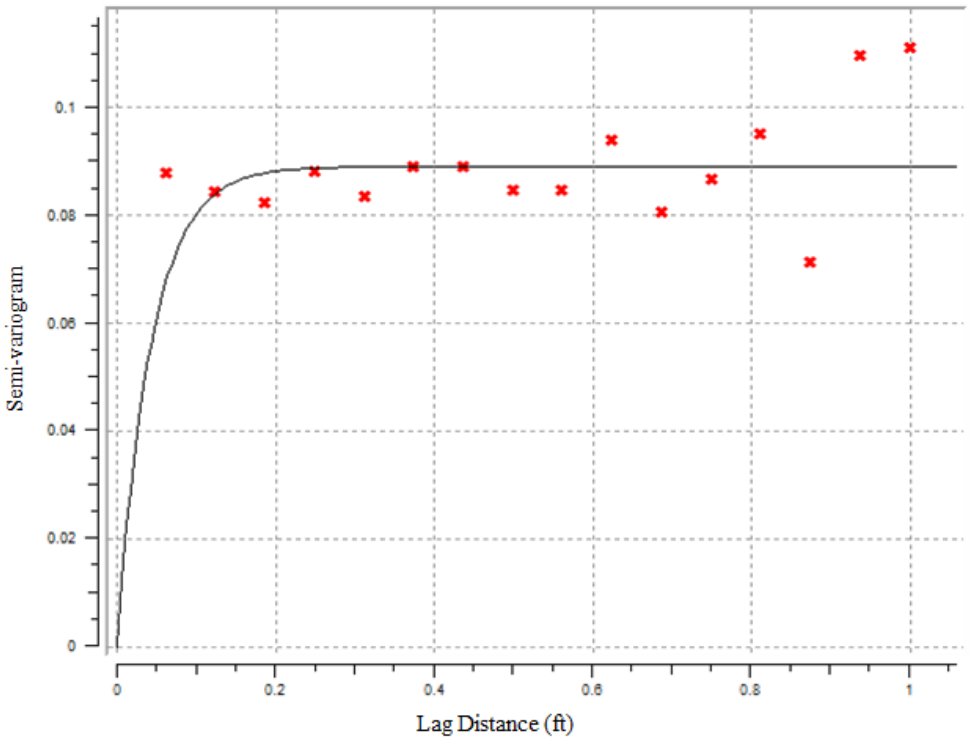

Well 21040 CT variogram

A1.29 Well 21040

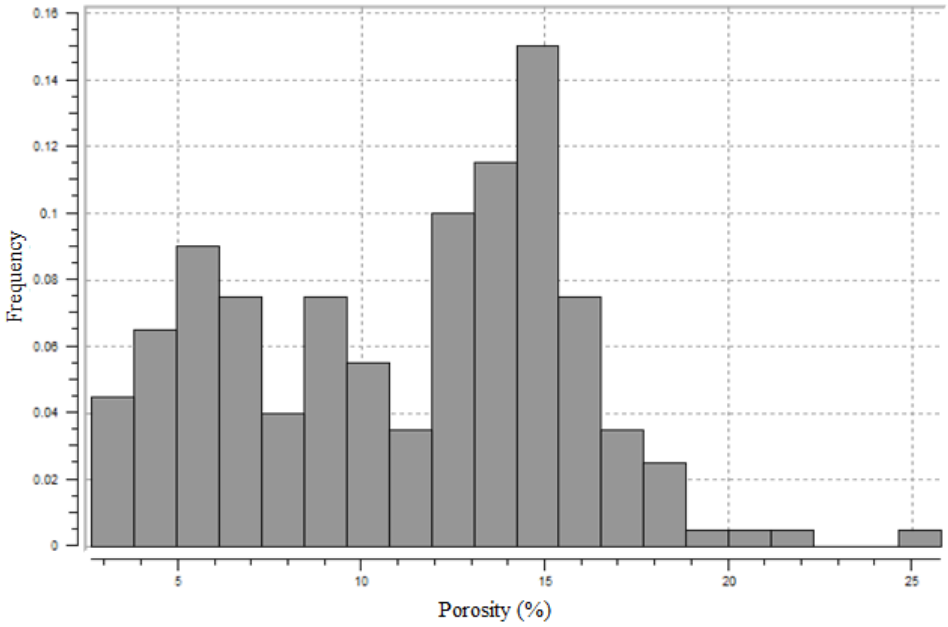

Well 21040 well log histogram

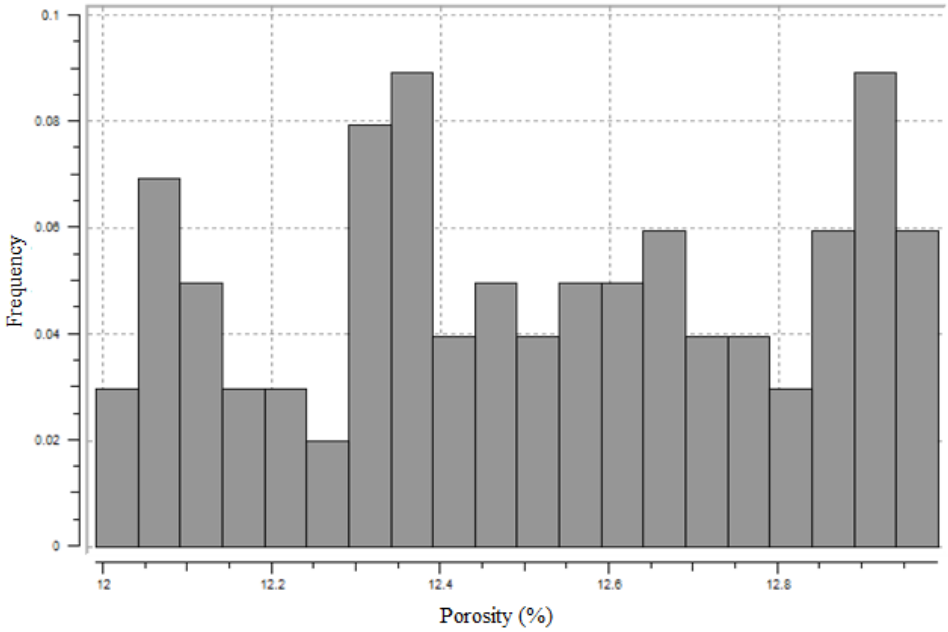

Well 21040 CT histogram

A1.30 Well 21040

REFERENCES

Akin, S., Ross, C.M., & Kovscek, A.R. (2008). Combination of well log and pore-scale data to predict petrophysical properties of diatomite. *Journal of Petroleum Science & Engineering, 60*(3), 133-149.

Alfaaouri, S., Riahi, M.A., Alizadeh, N., & Resaei. (2009). Permeability prediction in an oil reservoir and construction of 3D geological model by stochastic approaches. *Journal of Applied Sciences, 9*(11), 2016-2030.

Asghari, O., Soltni, F., & Amnie, H. B. (2009). The comparison between sequential Gaussian simulation (SGS) of choghart ore. *Australian Journal of Basic and Applied Sciences, 3*(1), 330-41.

Asquith, G., & Gibson, C. (1982) *Basic well log analysis for geologists*. Tulsa: The American Association of Petroleum Geologists.

Babak, O., & Deutsch, C.V. (2009). An intrinsic model of coregionalization that solves variance inflation in collocated cokriging. *Computers & Geosciences, 35*, 603-614.

Bigelow, E. (1992). *Introduction to wireline log analysis*. Houston: Western Atlas.

Carr, T., & Sawin, R.S. (1996). Hugoton natural gas area of Kansas. *Kansas Geological Survey, Public Information Circular (PIC), 5*. Retrieved March 29, 2012, from http://www.kgs.ku.edu/Publications/pic5/pic5_1.html

Choquette, P.W., & Pray, L.C., (1970). Geological nomenclature and classification of porosity in sedimentary carbonates. *AAPG Bulletin*, *54*, 207-250.

Chough, S.K., & Sohn, Y.K. (2010). Tectonic and sedimentary evolution of a Cretaceous continental arc-barkarc system in the Korean peninsula: New view. *Earth-Science Reviews*, *101*, 225-249.

Delbari, M., Afrasiab, P., & Loiskandl, W. (2009). Using Sequential Gaussian Simulation to assess the field-scale spatial uncertainty of soil water content, *Catena, 79*, 163-69.

Deutsch, C.V. (2002). *Geostatistical reservoir modeling*, New York: Oxford University Press.

Fournier, F. (1995). Integration of 3D seismic data in reservoir stochastic simulation: a case study. *Presented at Society of Petroleum Engineers Technical Conference,* Dallas, Texas. SPE30564.

Frykman, P., & Deutsch, C.V. (1999). Geostatistical scaling laws applied to core and log data. *Presented at Society of Petroleum Engineers Technical Conference,* Houston, Texas. SPE56822.

Harris, D., & Foufoula-Georgiou, E. (2001). Subgrid variability and stochastic downscaling of modeled clouds: Effects on radiative transfer computations for rainfall retrieval, *Journal of Geophysicsal Research*, *106*(D10), 10,349–10,362.

Hirsche, K., Boerner, S., Kalkomey, C., & Gastaldi, C. (1998). Avoiding pitfalls in geostatistical reservoir characterization: A survival guide. *The Leading Edge*, 493-504.

Isaaks, E.H., & Srivastava, R.M. (1989). *An introduction to applied geostatistics*. New York: Oxford University Press.

Journel, A.G., & Huijbregts, C.H.J. (1978). *Mining geostatistics*. New York: Academic Press Inc.

Journel, A.G., & Deutsch, C. (1993). Entropy and spatial disorder. *Mathematical Geology*, *25* (3), 329-355.

Al-Khalifah, M., & Makkawi, M. (2002). The impact of data integration on geostatistical porosity modeling: a case study from the Berri Field, Saudi Arabia. *Journal of Petroleum Geology, 25* (4), 485-498.

Kim, Y., Suh, B.S., & Kim, K. (2001). *Natural gamma effect in density determination in the gamma-gamma log and its correction.* Retrieved September 22, 2011, from http://www.kgs.ku.edu/Conferences/IAMG//Sessions/J/Papers/kim.pdf

Leary, P.C., & Al-Kindy, F. (2002). Power-law scaling of spatially correlated porosity and log(permeability) sequences from north-central North Sea Brae oilfield well core. *Geophysical Journal International, 148*, 426-442.

Liu, Y., Harding, A., Abriel, W., & Strebelle, S. (2004). Multiple-point simulation integrating wells, three-dimensional seismic data and geology. *AAPG Bulletin*, *88*(7), 905-921.

Lucia, F.J. (1999). *Carbonate reservoir characterization*. Berlin: Springer.

Luthi, S. (2001) *Geological well log: their use in reservoir modeling*. Berlin: Springer.

Matheron, G. (1970). Random functions and their applications in geology. In D. Merriman (Ed.), *Geostatistics – A Colloquium* (79-88). New York: Plenum Press.

Minasny, B., Vrugt, J.A., & McBratney, A.B. (2011). Confronting uncertainty in model-based geostatistics using Markov Chain Monte Carlo simulation. *Geoderma*, *163*, 150-162.

Newell, K.D., Watney, W.L., Cheng, S.W.L., & Brownrigg, R. (1987). *Stratigraphic and spatial distribution of oil and gas production in Kansas*. Kansas Geological *S*ociety: Subsurface Geology, Series Number 9.

Oz, B., Deutsch, C.V., & Frykman, P. (2002). A visualbasic program for histogram and variogram scaling. *Computers & Geosciences*, *28*, 21-31.

Paik, I.S., & Lee, Y.I. (1995). Short term climatic changes recorded in early Cretaceous floodplain deposits, Korea. *Proceedings of 15th International Symposium of Kyaungpook National University*. Korea. 395-417.

Pawitan, Y. (2001). *In all likelihood: statistical modelling and inference using likelihood*. New York: Oxford University Press Inc.

Prasad, M. (2003). Velocity-permeability relations within hydraulic units. *Geophysics*, *68*(1), 108-117.

Price, D., Curtis, A., & Wood, R. (2008). Statistical correlation between geophysical logs and extracted core. *Geophysics*, *73*(3), E97-E106.

Prothero, D.R., & Schwab, F. (2004). *Sedimentary geology: an introduction to sedimentary rocks and stratigraphy* (2nd ed.). New York: Freeman and Company.

Al Qassab, H.M., Fitzmaurice, J., Al-Ali, Z.A., Al-Khalifa, M.A., Aktas, G.A., & Glover, P.W. (2000). Cross-discipline integration in reservoir modeling: the impact on fluid flow simulation and reservoir management. *Presented at Society of Petroleum Engineers Technical Conference* Dallas, Texas. SPE62902.

Remy, N., Boucher, A., & Wu, J. (2009). *Applied geostatistics with SGeMS: A User's Guide*. New York: Cambridge University Press.

Remy, N., Boucher, A., Wu, J., & Li, T. (2009). Applied geostatistics with SGeMS [Computer software]. New York: Cambridge University Press.

Rider, M. (1986) *The geological interpretation of well logs*. New York: Blackie Halsted Press.

Serra, O. (1984) *Fundamentals of well log interpretation: The acquisition of logging data* (Vol 1). Amsterdam: Elsevier.

Tilke, P.G., Allen, D., & Gyllensten, A. (2006). Quantitative analysis of porosity heterogeneity: application of geostatistics to borehole images. *Mathematical Geology*, *38*(2), 155-174.

Tran, T. T., Wen, X., & Behrens, R.A. (1999). Efficient conditioning of 3d fine-scale reservoir model to multiphase production data using streamline-based coarse-scale inversion and geostatistical downscaling. *Presented at Society of Petroleum Engineers Technical Conference*, Houston, Texas. SPE56518.

Webster, R., & Oliver, M.A. (2007). *Geostatistics for environmental scientists*. Chichester: John Wiley & Sons.

Xu, W., Tarn, T.T., Srivastava, R.M., & Journel, A.G. (1992). Integrating seismic data in reservoir modeling: the collocated cokriging alternative. *Presented at Society of Petroleum Engineers Technical Conference* Washington, D.C. SPE24742.

Yao, T., Mukerji, T., Journel, A., & Mavko, G. (1999). Scale matching with factorial kriging for improved porosity estimation from seismic data. *Mathematical Geology 31*(1), 23-46.

VITA

Katrina Burch was born in Kansas City, Missouri. She graduated with honors from the University of Missouri – Kansas City in 2009 after earning a Bachelor of Science in Geology. In 2012, she graduated with a Master's of Science in Environmental and Urban Geosciences from the University of Missouri – Kansas City.